SUPRAMOLECULAR MODIFICATION OF MESOSCALE MATERIALS

by

SEAN ALDON FONTENOT

A DISSERTATION

Presented to the Department of Chemistry
and the Graduate School of the University of Oregon
in partial fulfillment of the requirements
for the degree of
Doctor of Philosophy

June 2012

DISSERTATION APPROVAL PAGE

Student: Sean Aldon Fontenot

Title: Supramolecular Modification of Mesoscale Materials

This dissertation has been accepted and approved in partial fulfillment of the requirements for the Doctor of Philosophy degree in the Department of Chemistry by:

Dr. Michael M. Haley	Chair
Dr. Darren W. Johnson	Advisor
Dr. David R. Tyler	Member
Dr. Kenneth M. Doxsee	Member
Dr. Paul J. Wallace	Outside Member

and

Kimberly Andrews Espy   Vice President for Research & Innovation/Dean of the Graduate School

Original approval signatures are on file with the University of Oregon Graduate School.

Degree awarded June 2012

DISSERTATION ABSTRACT

Sean A. Fontenot

Doctor of Philosophy

Department of Chemistry

June 2012

Title: Supramolecular Modification of Mesoscale Materials

The process of surface modification allows us to combine the structural advantages of

materials with the chemical functionality of organic compounds. Attachment of functional organic

molecules to surfaces of high surface area substrates yields materials having dense chemical

functionality. Materials with meso- and nanoscale features are often used as support substrates

because their small-scale features provide very high surface area. Mesoporous silica is one of the

most chemically accessible mesoscale materials, and the well-established chemistries of its

production and modification lead to controlled pore structure and rapid kinetics. Such materials

have seen use as sorbents for environmental remediation of contaminated water. For this

application, their high degree of functionality and high-affinity surface chemistries permit a

relatively small amount of material to effectively treat a large volume of water.

The many advantages of these highly engineered materials come at a relatively high

economic cost. The high-affinity chemical functionalities that provide these materials with

unprecedented efficiencies also make them correspondingly more difficult to recycle. One-time

utilization of these materials makes the cost-per-use high which consequently limits their

economically viable applications. The goal of this work has been to explore surface chemistries that

will allow high performance, regenerable or recyclable sorbent materials. Shifting from a single-

use material to a regenerable platform in which the mesoscale supports are recycled may lower the

environmental and economic costs of the material while retaining the advantageous properties of the meso- and nanostructured materials.

We chose to approach this goal by developing non-covalent, supramolecular surface modification techniques as alternatives to current surface modification techniques which, almost without exception, are based on covalent modification motifs. Non-covalent attachment of organic molecules to surfaces allows us to avoid the necessity of optimizing the attachment for each class of organic molecule as well as avoid protection and de-protection procedures necessary to attach delicate or reactive functional groups to surfaces. In this way, supramolecular modification processes reduce the cost of material research and development in addition to the costs of material production and use.

This dissertation contains previously published and unpublished co-authored material.

CURRICULUM VITAE

NAME OF AUTHOR: Sean A. Fontenot

GRADUATE AND UNDERGRADUATE SCHOOLS ATTENDED:

University of Oregon, Eugene
Hendrix College, Conway, Arkansas

DEGREES AWARDED:

Doctor of Philosophy, Chemistry, 2012, University of Oregon
Master of Science, Chemistry, 2010, University of Oregon
Bachelor of Arts, Chemistry; Minor, Religion, 2004, Hendrix College

AREAS OF SPECIAL INTEREST:

Surface Modification and Characterization of Materials
Supramolecular Chemistry
Organic and Physical Organic Chemistry

PROFESSIONAL EXPERIENCE:

Graduate teaching fellow and IGERT fellow, Department of Chemistry, University of Oregon, 2006-2012

Ph.D. intern, Energy and Environment Directorate, Pacific Northwest National Laboratory, 2009

Research technician, Arkansas Cancer Research Center, University of Arkansas for Medical Sciences, 2004-2006

Undergraduate research fellow, Arkansas INBRE (formerly BRIN) program, University of Arkansas and University of Arkansas for Medical Sciences, 2003

GRANTS, AWARDS, AND HONORS:

IGERT fellowship, University of Oregon, 2008-2011

PUBLICATIONS:

S. A. Fontenot, V. M. Cangelosi, M. A. Pitt, A. C. Sather, L. N. Zakharov, O. B. Berryman, D. W. Johnson, *Dalton Transactions,* 2011, **40**, 12125.

S. A. Fontenot, T. G. Carter, D. W. Johnson, R. S. Addleman, M. G. Warner, W. Yantasee, C. L. Warner, G. E. Fryxell, and J. T. Bays, in *Trace Analysis with Nanomaterials*, eds. D. T. Pierce and J. X. Zhao, Wiley-VCH Verlag GmbH & Co. KGaA, Weinheim, 2010, 191.

R. S. Addleman, J. T. Bays, T. G. Carter, S. A. Fontenot, G. E. Fryxell, D. W Johnson, "Renewable Sorbent Material and Method of Use" U.S. Patent # 20100147768, June 17, 2010

V. M. Cangelosi, L. N. Zakharov, S. A. Fontenot, M. A. Pitt, D. W. Johnson, *Dalton Transactions,* 2008, **26**, 3447.

ACKNOWLEDGEMENTS

To Dean and Lonnie Fontenot, my parents, and Adrienne and Billy, my younger siblings. From them I learned hard work, self-respect, compassion, self-sacrifice, forgiveness, and celebration.

To my great friends, David Grundman, Shannon Mockli, Joshua Tremblay, Liz Marg, Joey Williams, Sam Charles, Lyle Lowery, Stuart Price, and Ian Aucoin. In the words of Eddie Vedder: "I'm a lucky man to count on both hands the ones I love."

For the last fifteen years, I have invested most of my time in some sort or another of education or training which were, in many respects, selfish investments. Because of these pursuits, I have been absent for important moments, including deaths and funerals, in the lives of people who believed in me. In a way this work is the culmination of my educational pursuits, so it is with a fragile combination of joy and regret that I include in its dedication Kelvin Daigle and Frank Assunto, my uncles; Grace and Ronald Fontenot, my grandparents; and Gladys and Darmas Daigle, my great-grandparents.

TABLE OF CONTENTS

LIST OF FIGURES

LIST OF TABLES

LIST OF SCHEMES

CHAPTER I

MODIFICATION OF MESOPOROUS MATERIALS

1. Introduction

This dissertation focuses on development of new surface chemistries based on reversible, non-covalent interactions. Most of this work involves modification of mesoporous silica materials intended for application as sorbents. For that reason, this introductory chapter provides a primer on mesoporous silica preparation and current techniques for its modification as well as an introduction to the novel surface modification techniques presented later. This chapter will also introduce reversibly functionalized materials and discuss the special considerations warranted by these materials.

Modification of material surfaces is often conducted in order to combine the structural advantages of support materials with the chemical functionality of organic compounds. Such modifications have been used in the production of functional materials including sensors, biochips, and sorbents. The material application directs the choice of both the surface functionality and the surface structure/geometry. For instance, materials having high surface area per unit mass are useful for applications that benefit from the highest possible density of functionality. Most high-surface area materials are based on mesoporous supports such as mesoporous silica, mesoporous carbon, zeolites, or metal-organic frameworks (MOFs) which are reviewed in Chapter II. For such materials, the pore interiors provide most of the surface area.

The advantages of high surface area materials come as a compromise; materials with internal surfaces present a set of additional complications in terms of preparation and characterization. Characterization in particular is challenging since many advanced surface imaging techniques such as electron microscopy and atomic force microscopy (AFM), as well as depth-profiling techniques such as X-ray photoelectron spectrometry (XPS) and Auger electron

spectroscopy (AES) are less effective in characterizing porous materials. Materials without well-ordered meso- or nano-scale features are particularly difficult in this respect. All is not lost, however. The relative abundance of functional groups (per unit mass) of high-surface-area materials makes these amenable to gravimetric techniques such as thermal gravimetric analysis (TGA) as well as titration and classic colorimetric techniques which are less effective for analysis of low-surface-area materials.

2. Preparation of Mesoporous Silica

Mesoporous silica materials are, almost without exception, prepared by sol-gel processes in which silicate monomers are crosslinked in the presence of surfactants (Figure 1).[1–3] Surfactants self-assemble, forming colloidal structures that act as templates for the features of the final silica material. Crosslinking of silicate monomers yields a silica network which occupies the "negative space" outside of the surfactant template. Depending on the identity of the surfactant and the preparation conditions, materials may be constructed with more or less regular arrays of pore channels and with varying degrees of pore diameter distribution.
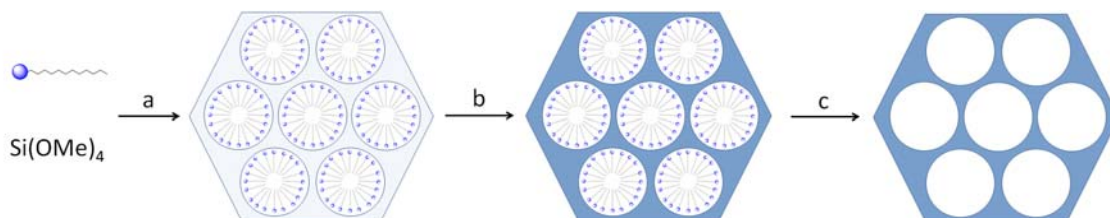
Figure 1. Preparation of mesoporous silica. a) A silane source (tetramethoxyorthosilicate in this example) and a surfactant (top left) are combined yielding a sol-gel in which silanes (represented by the light blue hexagon) are assembled around a surfactant template. b) The sol-gel mixture is heated yielding a highly crosslinked silane (represented by the dark blue hexagon). c) The surfactant is removed by washing and/or thermal degradation leaving the porous silica.

Crosslinking is often followed by calcination or partial calcination. The process of calcination is used to eliminate residual surfactant and complete crosslinking of the silica matrix which densifies the material, typically yielding a more uniform material.[4,5] Before calcination, the silica surface consists of varying numbers (depending on method of preparation) of hydroxylated silica atoms (silanols) and fully-crosslinked silica. Reactivity of the material surface is attributed to the presence of the silanol groups. Calcined surfaces are comparatively depleted of surface

silanols.[6,7] Thus, calcined silica materials generally have fewer reactive surface groups than their non-calcined counterparts.

3. Modification of Mesoporous Silica Surfaces

There are two primary strategies for preparing porous silica materials with functionalized surfaces: Co-condensation, (or synthetic modification) and post-synthetic modification.[6,8] Co-condensation involves attaching functional groups as crosslinking occurs. Post-synthetic modification is performed after the material has been crosslinked and may be performed post-calcination. Thus, post-synthetic modification relies on the presence of reactive functional groups (silanols) on the surface. Attaching organic functionality by either co-condensation or post-synthetic modification almost always involves the reaction of chlorosilanes or of siloxane species such as triethoxy- and trimethoxysilanes.[6]

3.1. Modification of mesoporous silica by co-condensation

Co-condensation is performed by incorporating functional silanes (siloxanes or chlorosilanes) capable of self-assembling along with the surfactant. These silanes are effectively part of the surfactant template in the sol-gel mixture (Figure 2). However, unlike typical surfactant molecules (such as quaternary ammonium species), they are incorporated along with the silicate monomers into the silica matrix. When the surfactant is removed, the functional portion of the silane precursor remains attached to the silica surface. Spatially, these functional portions are located in the empty space (the pores) previously occupied by the surfactant template. In this fashion, most of the functionality is present at the interior surfaces of the pores.[9]
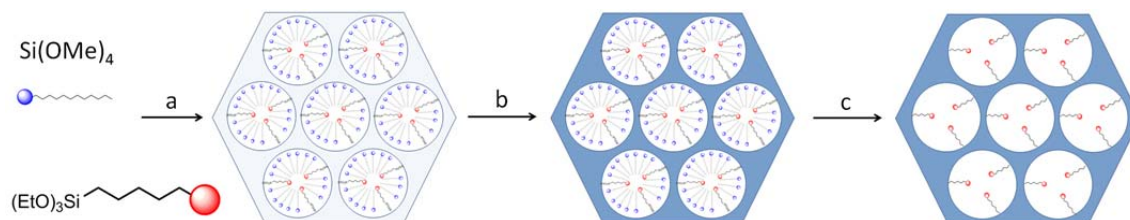
Figure 2. Preparation of functionalized mesoporous silica by co-condensation. a) A silica source, a surfactant, and a functional triethoxysilane (bottom right) are combined yielding a sol-gel mixture in which the surfactant template includes the functional organic molecule. b) Crosslinking leads to covalent attachment of the functional silane to the silica matrix with the functionality (represented by the red circle) directed inward. c) Removal of the surfactant leaves the crosslinked silane which includes the functional species.

Functional silanes used in co-condensation methods must be able to incorporate into the surfactant template in the sol-gel mixture. Incompatible silanes will not self-assemble along with surfactant molecules and may disturb the surfactant template. Functional silanes must also be compatible with the condensation chemistry. Co-condensation with any silane bearing a functional group (in addition to the silica group) capable of interacting the silicate monomers may lead to the destruction of the functionality by its incorporation into the silica matrix. For this reason, functional surfaces prepared by co-condensation generally feature chemically robust functional group such as amines, thiols, alkenes, and arenes. Since calcination requires temperatures near or above 500 °C, beyond the decomposition temperature of most organic functional groups, co-condensation usually precludes calcination.

3.2. Post-synthetic modification of mesoporous silica

Surface silanols react with chloro- and alkoxyslianes, allowing direct attachment of functional silanes to the mesoporous silica surface even after calcination (Figure 3). Direct silanation is performed by suspending the silica in a solvent, adding functional silane, and then removing the solvent and any unreacted silane.
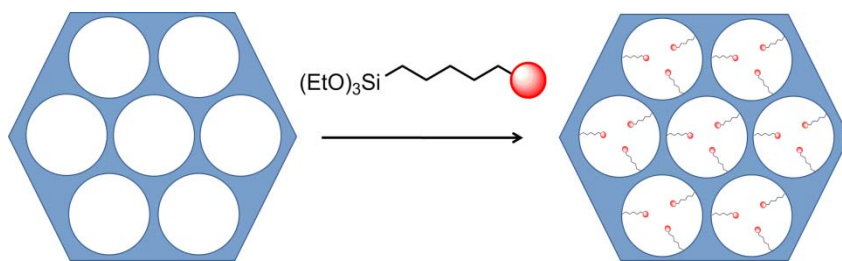
Figure 3. Post-synthetic modification *via* direct silanation of mesoporous silica. Functional triethoxysilanes may be incorporated to a pre-synthesized material. No surfactant template is necessary for this procedure.

For modification using alkoxysilanes, solvents that form azeotropes with the corresponding alcohol byproducts are ideal since the removal of these byproducts drives the reaction *via* Le Chatelier's Principle, allowing more efficient reaction and more complete surface coverage. Direct silanation methods suffer from similar chemical incompatibilities to co-condensation methods. However, a much higher degree of functionalization can be achieved with direct silanation methods

since they require no surfactant which could obscure some of the reactive pore sites during silanation.

To sidestep the chemical incompatibilities of both co-condensation and direct silanation methods, a functional surface may be prepared to set up for secondary modification (modification of deposited functional groups). This allows attachment of fragile functional groups which would not survive the crosslinking of silicates, silanation, or calcination. Secondary surface modifications have been demonstrated using click reactions, dative bonds, Diels-Alder reactions, acid halide additions, and carbodiimide additions.[3,10] In Chapter IV of this work, we describe secondary modifications using amines to support amide formation and urea formation *via* Staudinger-type reactions. The supramolecular modification methods, the focus of this work, could also be examples of secondary (ternary in some cases) surface modifications.

3.3. Supramolecular modification of mesoporous silica surfaces

Supramolecular surface modification can be considered a subset of the post-synthetic modifications discussed in Section 2.3 of this chapter. Supramolecular chemistry has been said to be the chemistry of the intermolecular bond.[11,12] We have applied supramolecular interaction motifs to the problems of surface modification and, in doing so, have developed new methods of surface modification based on these motifs. Beyond basic science investigation, our justification for this project is twofold. 1) Since supramolecular interactions do not involve the destruction or formation of covalent bonds, they are typically tolerated by even the most delicate of functional groups. Therefore, it should be possible to easily attach any organic functional group to a surface *via* supramolecular interactions. 2) Generally speaking, the stability of a supramolecular association is highly dependent on the environment. From a material design perspective this dependence is a double-edged sword. Certain interactions will be limited to suitable environments (see the following example in Figure 4). On the other hand, this dependence allows reversibility of supramolecular associations simply by changing the chemical environment (switching the polarity of a solvent, for example).[13] This dissertation introduces water-persistent two-component association motifs which we apply to silica and iron oxide surfaces.

An example of a stable, reversible, non-covalent surface functionalization technique was demonstrated by Yoshitaki and coworkers who prepared an ethylenediamine-functionalized silica surface (EDA-SAMMS).[14] The EDA functional groups associate with Cu(II) and Fe(III) among

others (Figure 4). The Fe(III) surface yielded a material (Fe-EDA-SAMMS) with excellent sorbent properties; capable of removing arsenate, selenite, and chromate from water. Our investigations involving these materials confirm that Fe- and Cu-EDA SAMMS remain excellent sorbents for arsenate and chromate at neutral or basic pH and even in the presence of competing anions. The association between Fe(III) and the EDA surface is reversible. Yoshitake and coworkers demonstrated that almost all of the Fe(III) could be removed, regenerating the EDA surface, by acid washing. Since the association of Fe(III) to EDA is stable to an acidic environment in which the Fe(III)-EDA association is not stable in an acidic environment, we are able to effectively reverse the modification of the EDA-SAMMS surface.
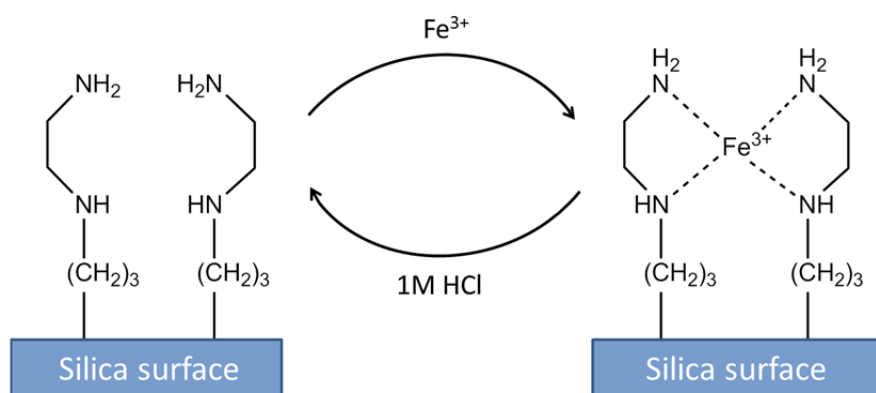
Figure 4. An illustration of the reversible secondary functionalization of the EDA-SAMMS surface.   EDA-SAMMS (left) will associate with Fe(III) in water forming a persistent Fe-EDA surface. This association is unstable in acidic environments. Thus, the Fe-EDA association may be reversed by acidifying the solution.

We have developed two systems which are conceptually similar to the EDA-SAMMS system. Chapter III presents the development of a surface modification system based on interactions between a phenyl-modified silica surface (Ph-SAMMS) and functional aromatic compounds which form the secondary surface. Since both the Ph-SAMMS surface and the aromatic secondary surface species are quite hydrophobic, the associations between surface phenyls and secondary surface species are persistent in aqueous environments but unstable in organic environments. This differential stability allows us to reverse the secondary functionalization of Ph-SAMMS. Chapter IV presents a surface modification motif based on the association of a surface of cyclodextrin molecules with small organic molecules. This motif is also persistent in aqueous environments and can be reversed by lowering the polarity of the environment. For both

of these materials, the functionalizing groups contain thiols. Thiol-based materials have well-established sorbent characteristics and conventionally functionalized (by direct silanation) thiol-bearing analogues of our supramolecular materials were available or easy to prepare for direct comparision.[15–18] In addition, surface thiols may be directly quantified by the Ellman's test for thiols.[19] This provides an extra analytical handle for material characterization which would not have been available for non-thiol materials.

3.4. Geometric considerations of surface modification

The effects surface modifications on pore diameter and surface area are important to material design. In almost all cases, mass transport through the pores, affected to a great extent by pore diameter, limits the speed at which reactions between the environment and pore interiors reach equilibrium.[20,21] Modification of porous material surfaces effectively decreases pore diameter and, by extension, the available surface area of the material (Figure 5). Surface area is primary limiting factor in the number of accessible functional groups per gram of material. For sorbent materials, this effectively dictates the sorbent capacity.
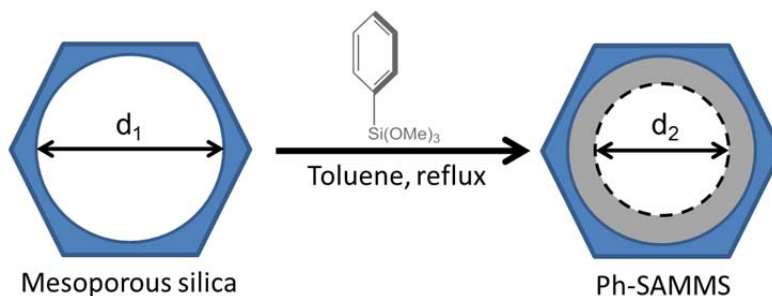
Figure 5. Illustration of pore diameter reduction upon functionalization with a phenylsilane. Reduction in pore diameter is accompanied by a corresponding reduction in surface area.

The sizes (thickness) of the modifying species as well as the extent of modification (i.e. density of functional groups) determine the magnitude of the reduction in pore diameter surface area. This is exemplified by the series of phenyl-functionalized materials presented in Chapter III, Section 2. It is important to note that materials with smaller pores experience a proportionally *larger* reduction in pore size for a given surface thickness and coverage. For this reason, we found it optimal in some cases to start with a larger pore size (lower initial surface area) in order to achieve a respectable final surface area while maintaining a pore size sufficient for favorable mass transport

kinetics. As a final consideration: The curvature of the pores means that the steric clash of nearby functional groups will be more significant depending on the thickness of the modifying group. For instance, when a bulky functional group is tethered to the surface, repulsion between nearby functional groups increases with the length of the tether. An important implication of this geometric feature is that modeling the footprint of a surface molecule as if the surface were flat will always overestimate the maximum surface coverage of a porous material.

4. Summary and Bridge to Chapter II and Sequent Chapters

By attaching functional molecules to surfaces of materials, we impart the functionality of those molecules onto the materials. By modifying the ample surfaces of mesoporous materials, we can produce materials with very dense functionality. As a result of the meso- and/or nanoscale features of these materials, characterization is complicated and new design considerations, including the geometric considerations outlined in the previous section, are necessary for the production of functional and efficient materials. Application of such materials as sorbents is of great interest in terms of both sensing and remediation as well for a host of other applications. Because of this application potential a variety of surface modification techniques, including the ones developed as part of this work, have been invented and were introduced in this chapter. Chapter II is a review of functionalized meso-and nano-structured materials, including mesoporous silicas, for application as sorbents for analysis and remediation. This review discusses mesoporous materials in the context of a variety of other surface chemistries and morphologies and identifies material characteristics which are important to sorbents in particular. Chapter II was co-authored by Timothy G. Carter, Darren W. Johnson, R. Shane Addleman, Marvin G. Warner, Wassana Yantasee, Cynthia L. Warner, Glen E. Fryxell, and John T. Bays, and was previously published.

Chapter III describes a supramolecular surface modification motif based on arene-arene interactions. Chapter III was co-authored by Timothy G. Carter, Darren W. Johnson, and R. Shane Addleman, and will be submitted for publication. Chapter IV describes a supramolecular surface modification motif based on cyclodextrin host-guest associations. Chapter IV was co-authored by Kara M. Sherman, Anna S.Ivanova and Darren W. Johnson, and will be submitted for publication. Chapter V presents an investigation of the solid-state geometreis of As_2L_3 cryptands. Chapter V was co-authored by Virginia M. Cangelosi, Melanie A. Pitt, Aaron C. Sather, Lev N. Zakharov, Orion B. Berryman, and Darren W. Johnson and was previously published.

CHAPTER II

NANOSTRUCTURED MATERIALS FOR SELECTIVE COLLECTION
OF TRACE-LEVEL METALS FROM AQUEOUS SYSTEMS

This chapter was co-authored by Timothy G. Carter, and Darren W. Johnson from the Department of Chemistry and Materials Science Institute, University of Oregon and R. Shane Addleman, Marvin G. Warner, Wassana Yantasee, Cynthia L. Warner, Glen E. Fryxell, and John T. Bays of the Materials Chemistry and Surface Research Group, Pacific Northwest National Laboratory. Timothy Carter, Darren Johnson, Shane Addleman, Marvin Warner, Wassana Yantasee and Glen Fryxell each contributed material to this chapter. John Bays and Cynthia Warner participated in analysis and provided editorial assistance. Sean Fontenot prepared the chapter, contributed to each section, provided the most of the material, performed literature research and analysis, and compiled material from the other authors. This chapter was published as a chapter of the same name in "Trace Analysis with Nanomaterials" by D. T. Pierce, J. X. Zhao, Wiley-VCH, Weinheim, 2010, 191.

1. Introduction

This chapter surveys the use of nanostructured materials for the selective collection of trace-level metals from aqueous systems. Herein, we will discuss application of these materials to various environmental challenges with a focus primarily upon analytical applications. The unique properties of the nanostructured materials and the advantages they provide will be summarized. It will be shown that, when correctly constructed, these materials are superior sorbents and can be used to enhance trace level analysis.

A number of separation and filtration techniques are available for the collection of trace level species and each method must be matched to specific application. For trace level metals in

solution arguably the best and most widely used methods involve solid phase sorbents materials that provide effective capture of desired metal species. Effectiveness of the solid phase sorbent for any given application is determined by availability, cost, and performance. Activated carbon and ion exchangers are widely available and relatively cheap but in most cases do not have the performance necessary for many analytical applications. Activated carbon and ion exchangers generally fail to have the selectivity and affinity needed for trace analyte collection from actual environmental matrices.

A critical capability for understanding and responding to situations involving toxic materials is the ability to quickly identify the toxic material(s) involved and the extent of contamination. This is a key issue for circumstances ranging from responding to terrorist attacks to monitoring environmental remediation efforts. Unfortunately, analytical technology does not presently exist to meet these needs. Instruments powerful enough to meet the required speed, sensitivity, and selectivity requirements do not function well outside of rigorously controlled laboratory conditions and are usually very complex and expensive. Simple screening methods that provide immediate results in the field enable on-site, near-real-time decisions. These field screening methods are typically less costly and more rapid than formal laboratory analysis; this is significant since site testing and monitoring typically involves extensive sampling. To meet this need, a wide range of field screening methods for identifying chemical, biological, and nuclear materials is presently being marketed and used. Unfortunately, existing field assay methods are typically inadequate because they lack the selectivity and sensitivity needed to provide reliable information. The degree and type of improvement needed vary with application but sensitivity improvements of greater than 1000-fold are typically required, and much larger enhancements would usually be preferred. This large leap in analytical performance is unlikely to be achieved with incremental improvements in measurement procedure, instrument design, or improved electronics. A new analytical approach is required.

In many circumstances the deficiencies in selectivity and sensitivity could be addressed with high performance sorbent materials that selectively concentrate the target analyte. In addition to concentrating the target analyte(s) the sorbent can exclude interfering species and provide a uniform, well-defined sample matrix for analysis. Sorbents coupled with instrumentation could be used for either real-time analysis of the signature species or as a rapid screening method to flag those samples that require more detailed analysis. Sorbents coupled with rugged, compact

instrumentation could provide portable, yet highly sensitive, field analyzers that could be quickly reconfigured for new analytes simply by changing the sorbent material. Sorbents used in these systems could be designed to be reusable, renewable or disposable depending upon the instrument configuration desired and material chemistries involved. These same sorbents could be used to improve the performance of traditional laboratory techniques with more effective sample clean up.

This book chapter is a discussion and review of various advanced nanostructured materials applicable to the selective collection of trace-level analytes from aqueous systems for sensing and separation applications. For consistency and comparison, when possible, materials expressing thiol surface chemistry are used as examples. While a plethora of surface chemistries exist and many have relevance to environmental challenges, the thiol surface chemistry is highly effective for the capture of many toxic heavy metals from aqueous systems, and serves as a useful baseline to compare materials performance. Further, the thiol surface chemistry has been demonstrated on a range of nanostructures and therefore provides continuity and a common platform for nanomaterial comparison. This chapter is organized into sections by the material type. Discussions are broken down into the materials science and application of:

- Functionalized nanoporous silica materials

- Functionalized magnetic nanomaterials

- Carbon based nanostructured materials

- Other materials such as zeolites, and imprinted polymers

- Concluding thoughts on economics and the future of nanostructured materials in trace analysis

2. Thiol Functionalized Mesoporous Silica for Heavy Metal Collection

Removal of heavy metals, such as mercury (Hg), lead (Pb), thallium (Tl), cadmium (Cd), and arsenic (As) from natural waters has attracted considerable attention because of environmental contamination and their adverse effects on environmental and human health. Introduction of sorbent functionalities into nanoporous structures has significantly improved the performance of those sorbent materials in metal removal when compared to conventional sorbent beds.[1-3] This section reviews the ability of thiol functionalized ordered mesoporous silica, termed thiol self-assembled monolayer on mesoporous support (SH-SAMMS™) for the capture of heavy metals, which is superior to commercial sorbents such as Duolite® GT-73 resins and Darco® KB-B

activated carbon. SH-SAMMS[TM] also presents new applications beyond environmental applications, including chelation therapies and biomonitoring of heavy metals.

The metal binding affinity of a sorbent can be expressed in terms of the distribution coefficient (K_d). The K_d, in mL/g, is simply a mass-weighted partition coefficient between the solid phase and liquid supernatant phase as follows:

$$K_d = \frac{(C_o - C_f)}{C_f} \times \frac{V}{M}$$

C_o and C_f are the initial and final concentrations in the solution of the target species, V is the solution volume in mL, and M is the mass of the sorbent. The higher the K_d value, the more effective the sorbent material is at capturing and holding the target species. In general, K_d values of ~10^3 are considered good and those above 10^4 are outstanding.[4]

The ability of a sorbent material to capture a metal ion depends on the pK_a of its ligand, the stability constant of the metal-ligand complex, the presence of competitive ligands in solution, the pH of the solution[5], and the metals ions capacity to undergo hydrolysis[6]. Figure 1 shows the binding affinity (K_d) of SH-SAMMS[TM] to various metal ions in HNO_3 spiked filtered river water. As anticipated from Pearson's hard-soft acid-base theory (HSAB)[7], soft ligands like thiol groups prefer to bind soft metals like Hg and Ag, rather than a relatively harder metal such as Co. Based on the K_d values, the SH-SAMMS[TM] is an outstanding sorbent for Hg, Ag, Pb, Cu, and Cd ($K_d > 50,000$ mL/g), and a good sorbent for As in river water at neutral pH. SH-SAMMS could effectively bind Hg, Ag, and As for the entire pH range (pH 0 to 8.5), Cu from pH 2 to 8.5, and Cd and Pb from 6 to 8.5. Work in our laboratory reveals that Hg is strongly bound to SH-SAMMS[TM] even in acid concentrations as high as 5 M of acid (HCl and HNO_3). Above pH 7, a noticeable drop in K_d of Ag, Hg, Cd, and Pb (all still above 10^5) may be a result of strong association between the metal ions and native anions in the water (e.g., between Ag(I) and reduced sulfur groups[8] or Ag(I) and Hg(II) and chloride anions).[9,10]

In most pH-adjusted samples (e.g., pH 0 - 8.5), ionic strength is also varied, and may affect the metal binding affinity of a sorbent. Table 1 shows that ionic strength does not significantly affect the SH-SAMMS[TM] material until the concentration reaches 1 M sodium (as acetate) concentration. In the three natural waters, the affinity of SH-SAMMS[TM] for all metals tested remained virtually unaffected.
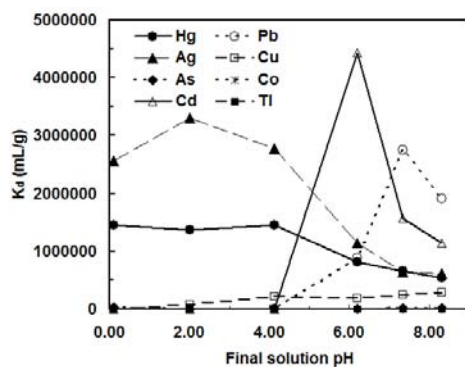
Figure 1. Effect of pH on the K_d values of SH-SAMMS™, measured in HNO_3 spiked filtered river water with a liquid to solid (L/S) ratio of 5000:1.

Matrix	pH	Cu	As	Ag	Cd	Hg	Pb
Columbia River water, WA[b]	7.66	9.5×10^5	7.2×10^4	7.1×10^6	1.0×10^7	3.6×10^5	5.3×10^6
Hanford ground water, WA[b]	8.00	1.3×10^6	5.7×10^4	1.1×10^7	1.1×10^7	5.9×10^5	5.6×10^6
Sequim Bay sea water, WA[b]	7.74	1.3×10^6	9.2×10^4	7.5×10^6	1.5×10^7	2.5×10^6	3.4×10^6
0.001 M CH_3COONa	7.14	-	4900	-	1.5×10^6	3.8×10^5	3.1×10^5
0.01 M CH_3COONa	7.19	-	2900	-	3.3×10^6	3.0×10^5	8.5×10^5
0.1 M CH_3COONa	7.21	-	4100	-	3.9×10^6	6.6×10^5	6.6×10^5
1.0 M CH_3COONa	7.28	-	2000	-	7.5×10^5	5.7×10^5	9.2×10^4

Table 1. Matrix effect on K_d of various metals on SH-SAMMS™[a] Reprinted with permission from reference 11. (a) Reported as average value of three replicates, L/S of 5000 mL/g; (b) 0.45 micron filtered.

Table 2 summarizes K_d of metal ions in filtered ground water (pH 6.8-6.9), measured for different sorbents. Note that thallium was added into the solutions as Tl(I) and arsenic as As(III). In terms of K_d, SH-SAMMS™ is significantly superior to the commercial GT-73 and activated carbon (Darco KB-B) for capturing Hg, Cd, Ag, Pb, and Tl. The superior affinity is owing to the multidentate chelation ability and the suitable substrate of SH-SAMMS™ that are not found in the commercial resins.

13

Figure 2 shows the adsorption isotherms of Hg on SH-SAMMS™, DMSA-Fe$_3$O$_4$, and GT-73 in filtered groundwater (pH 8.1).[12] The isotherm curves present the Hg uptake as a function of the equilibrium Hg solution concentration at room temperature. The saturation adsorption capacity of Hg on SH-SAMMS™ was found to be 167 mg/g but in filtered ground water (pH 8.1) while that of GT-73 was only 8 mg/g in the same water. In acidified river water (pH 1.99), a Hg adsorption capacity of 400 mg/g of SH-SAMMS™ has been achieved. The large surface area of the DMSA-Fe$_3$O$_4$ (114 m^2/g, see Section 3 for more details) and SH-SAMMS™ (114 m^2/g) afforded a high number of ligands on the materials, leading to a large ion loading capacity. Although the capacity of GT-73 for Hg in DI water (pH 4-6) was reported to be 600 mg/g [13], the measured Hg capacity in groundwater reported here is only 8 mg/g, which suggests very poor selectivity of the GT-73's binding sites in groundwater.

Sorbent	Final pH	Co	Cu	As	Ag	Cd	Hg	Tl	Pb
DMSA-Fe$_3$O$_4$	6.91	3000	2.7×10^5	5400	3.6×10^6	1.0×10^4	9.2×10^4	1.4×10^4	2.3×10^6
Fe$_3$O$_4$	6.93	1600	7400	5800	1.3×10^4	2400	1.6×10^4	4000	7.8×10^4
SH-SAMMS™	6.80	430	1.7×10^6	950	6.7×10^7	6.6×10^4	1.1×10^6	1.5×10^4	3.5×10^5
Thiol resin[a]	6.76	890	6300	1200	1.6×10^4	1500	1.0×10^4	2200	4.1×10^4
Activated carbon[b]	6.90	790	2.6×10^4	750	2.7×10^4	1300	3.1×10^4	21	1.9×10^5

Table 2. K_d of metal ions on selected sorbents in Hanford ground water. Reported as average value of three replicates, L/S = 10000 mL/g, in 0.45 micron filtered ground water. a) GT-173 by Rohm & Hoss b) Darco KB-B.
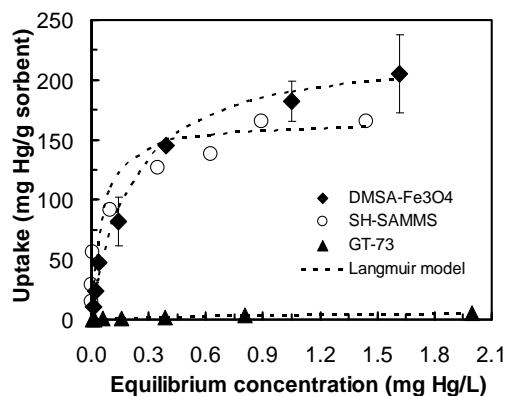
Figure 2. Adsorption isotherm of Hg in groundwater (pH 8.1) on DMSA-Fe$_3$O$_4$ (L/S, 5x10^5), SH-SAMMS (L/S, 5x10^5) and GT-73 (L/S, 7000). Dash-lines represent Langmuir modeling of the data. Reprinted with permission from reference 12.

In addition to covalently linking functional head groups to mesoporous silica, an alternative connective approach utilizes weak interactions through π-π stacking between an 'anchored' aromatic monolayer and chemisorbed functionalized ligands. One example studied various mono and bisfunctionalized mercaptomethyl benzenes adsorbed onto mesoporous silica containing a phenyl monolayer (Phenyl-SAMMS).[14] Comparisons between these materials and Thiol-SAMMS shows similar uptake capacities and kinetics. For instance, K_d values for Phenyl-SAMMS chemisorbed with 1,4-bis(mercaptomethyl)benzene show similar capture levels with the covalently attached Thiol-SAMMS in Hanford well water matrix spiked with 500 ppb Hg(II), Pb(II), Cd(II), and Ag(I) ions. Therefore, the metal affinity levels of the chemisorbed Phenyl-SAMMS are near equal to that of the covalently bound Thiol-SAMMS. Because of the weak yet stable interaction imparted by the π-π stacking, these materials have shown the ability to be stripped of their metal-loaded ligands by simple organic washes, thus leading to the possibility of regeneration of the base Phenyl-SAMMS material. The ability to regenerate is an attractive feature for both water purification and preconcentration-based technologies. Regeneration of the base material with a simple infield wash can greatly reduce the overall usage cost; an essential criteria for sorbent materials.

In addition to sorption affinity, capacity, and selectivity to the target metal ions, it is important that a sorbent material offer rapid sorption in order to minimize the time required to remove metal ions. Figure 3 shows the uptake rate of Pb on various sorbent materials measured in filtered groundwater (pH 7.7). Pb could be captured by SH-SAMMS™ at a much faster rate than

the two commercial sorbents, Chelex-100 (an EDTA-based resin) and GT-73 (a thiol functionalized resin). Specifically, after one minute of contact time, over 99 wt% of 1 mg/L of Pb was removed by SH-SAMMS, while only 48 wt% and 9 wt% of Pb were removed using Chelex-100 and GT-73, respectively. It took over 10 minutes for Chelex-100 and 2 hours for GT-73 to remove over 96% of Pb. GT-73 and Chelex-100 are synthesized by attaching chelating ligands to porous polymer resins, which dominate their physical properties. Thus GT-73 and Chelex-100 are subject to solvent swelling and have dendritic porosities. The SH-SAMMS^{TM} has a rigid silica support and open pore structure that allow for rapid diffusion of analytes into the binding sites, resulting in extremely fast sorption kinetics.

Sorbents that can capture heavy metals in biological media such as blood, gastrointestinal fluids, and urine are highly desirable for several reasons. The decorporation of toxic metals from blood and gastric intestinal fluids is anticipated to provide a breakthrough in chelation therapy.
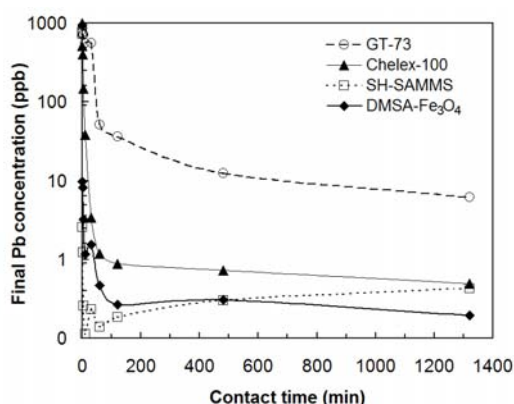
Figure 3. Kinetics of adsorption of 1000 ppb of Pb in filtered groundwater. pH 7.8, all with L/S of 1000, except DMSA-Fe$_3$O$_4$ with L/S of 2000, from reference 12. Nanostructured silica and DMSA-Fe$_3$O$_4$ show superior kinetics and better uptake efficiency.

Since the 1940s, *in vivo* toxic metal immobilization has involved the use of intravenous ethylenediaminetetraacetate (EDTA) treatment or oral/intravenous dimercaptosuccinic acid (DMSA) treatment following metal exposures. Solid sorbents are potentially better than their liquid counterparts because (1) when used as oral drugs, they can minimize the gut absorption of ingested harmful chemicals to human body, and (2) when used in extracorporeal decorporation (or hemoperfusion) devices, they can remove the chemicals in blood that have been absorbed

systemically from all routes of exposure (oral, dermal and inhalation), which decreases the burden on the kidneys for clearing the toxic metal-bound liquid chelating agents.

SH-SAMMS[TM] captures a large percentage (~90%) of As, Cd, Hg, and a moderate percentage of Pb, presented in human urine and blood at relevant exposure levels (50 μg/L). Not only can SH-SAMMS[TM] remove inorganic Hg(II) as shown in Table 3, but it can also remove methyl Hg(II) (CH_3Hg^+, which is a much more problematic form of Hg); for example, at L/S of 200, 87% of methyl Hg(II) was removed from human plasma containing 100 μg/L of the analyte. Figure 4 also shows the K_d of the four metals on SH-SAMMS[TM] measured in synthetic gastrointestinal fluids, with a pH similar to what might be encountered within the various regions of the gastrointestinal tract (pH 1-3 in stomach, pH 5.5-7 in large intestine, pH 6-6.5 in duodenum, and pH 7-8 in jejunum and ileum),[15,16]
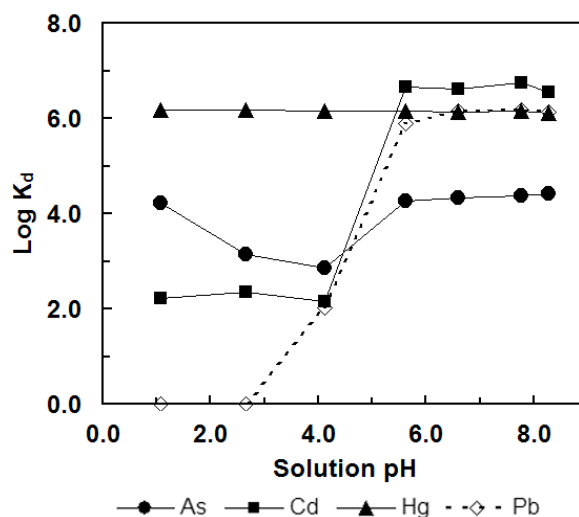
Figure 4. K_d of As, Cd, Hg, and Pb, measured on SH-SAMMS**[TM]** in synthetic gastrointestinal fluids prepared by adjusting synthetic gastric fluid (contained 0.03 M NaCl, 0.085 M HCl, pH 1.11) with 0.2 M $NaHCO_3$ to the desired pH; initial metal ion concentrations of 50 μg/L and L/S of 5000.

Matrix	L/S	Initial metal concentration	As	Cd	Hg	Pb
Human blood	1000	50 μg/L	90	93	92	15
Human urine	1000	50 μg /L	93	87	89	33

Table 3. Percent removal of heavy metals from biological matrices using SH-SAMMS[TM] reported as average values of three replicates, S.D. < 5%.

In addition to their use in chelation therapies, the sorbent materials that can effectively concentrate heavy metals from complex matrices like blood and urine will substantially improve biomonitoring of exposure to these species. Direct preconcentration of toxic metals from biological samples without acid digesting them first has been a challenging task for two main reasons. The proteins and macro molecules in complex biological samples can compete with the sorbent materials for binding with the metal ions resulting in low capture extent (e.g., an example is Pb in Table 3). Additionally, these biomolecules foul the sensors resulting in rapid degradation (especially in electrochemical sensors where proteins adsorb on the sensor surface and form an insulating layer). By employing Nafion as an antifouling layer and SH-SAMMS™ as the metal concentrator, we have successfully used the SH-SAMMS™-Nafion composite in electrochemical sensors for low ppb (µg/L) detection of heavy metals (e.g., Cd and Pb) in urine without sample pretreatment or protein fouling. [17] The resulting sensor offered the detection limits similar to the state-of-the-art inductively coupled plasma mass spectrometry (ICP-MS). Unlike the ICP-MS, the sensor is portable and will facilitate rapid biomonitoring of exposure to toxic metals. SH-SAMMS™ nanomaterials have recently emerged as highly effective sensors for trace metal detection. Their high efficacy for metal concentration is presently being explored to enhance a range of analytical methods including ICP-MS, radiological measurements, and X-ray fluorescence among other techniques.

3. Functionalized Magnetic Nanoparticles for Metal Capture and Detection

In this section, we will focus on the application of engineered magnetic nanoparticles (diameter < 100 nm in most cases) that contain a thiol surface functionality for the purpose of separating and detecting a wide variety of analytes from complex environmental matrices. Recently, the use of functionalized superparamagnetic nanoparticles in environmentally relevant applications such as selective capture and pre-concentration of specific analytes from complex samples for sensitive detection has been reported in an increasingly large number of publications and reviews.[12,18-34]

As stated above a fundamental approach for improving any analytical method is to selectively separate the analytes from the sample matrix and concentrate them into a smaller volume prior to measurement. Preconcentration of the analytes prior to assay allows one to improve the sensitivity, selectivity, and speed of analytical process. Preconcentration is an ideal

application for functionalized magnetic nanoparticles. Once dispersed in solution they can rapidly contact high volumes, selectively capture target analytes, and then can be magnetically recovered and manipulated by the application of a relatively strong (often > 1 T) but easily generated magnetic field. The functionalized magnetic nanoparticles provide a magnetically controllable sorbent material for solid phase extraction (SPE). It has been demonstrated that the intrinsic high surface area arising from the nanoscale dimensions of these nanomaterials and the ability to impart specific surface functionalization make magnetic nanoparticles very effective for SPE.[35] In addition, the magnetic nanoparticles have the advantage that very small quantities of materials are required to accomplish effective preconcentration and detection. Once preconcentration is complete the analyte can be stripped off the SPE material for assay as appropriate (e.g. *via* acid, organic solvent, thermalization, etc.). Alternatively, for some applications the SPE material can be assayed directly.[35]

The amount of analyte extracted by the SPE material is limited by the magnitude of the partition or distribution coefficient (K_d) of the analyte between the sorbent material and the sample matrix, as described in the previous section, since at trace levels saturation does not become an issue. By employing high surface area (typically > 100 $m^2 g^{-1}$), dispersible, and specifically functionalized magnetic nanoparticles one is able to drive the interaction of the nanoparticle sorbents with the analytes in the sample effectively facilitating both separation and preconcentration. As stated above, the higher the K_d value the better the SPE material will work for trace level assay. Large surface areas (usually > 100 $m^2 g^{-1}$) and high affinity surface chemistries enable the large K_d values needed for effective SPE. The surface chemistry of the SPE material dictates the selectivity of the material for a given analyte, and adjusting the surface chemistry of the SPE material allows it to be applied to different classes of analytes or function in different matrices. A comparison of the K_d values for a variety of different SPE materials, including functionalized superparamagnetic nanoparticles, in filtered ground water is shown previously in Table 2.

From a broader perspective, magnetic nanoparticles have the potential to be extremely effective SPE materials for the preconcentration, removal, and detection of environmental contaminants. The surface can be tailored to target a wide range of analytes in much the same manner as the SAMMS materials discussed above. This is accomplished by incorporating small organic molecules onto the surface of the nanoparticles that contain two sets of functional groups; one with an affinity toward the iron oxide surface (i.e. carboxylic acid and/or silane) and another

with an affinity toward the target metal analyte of interest.

Complementing the ability to modify the surface chemistry with analyte-selective ligands, these materials have a unique property, namely superparamagnetism that arises from their nanoscale single magnetic domain structures[25]. Superparamagnetic behavior manifests itself in nanoparticles that are smaller than the critical diameter which is material and temperature dependent. Throughout the bulk of this section, we will predominantly be discussing iron oxide nanoparticles with diameters ranging from 5-20 nm which falls within the established critical diameter for this material (~15-20 nm). From a practical standpoint, a superparamagnetic nanoparticle has little to no remnant magnetization after exposure to a magnetic field and low to no coercivity (the field required to bring the magnetization to zero) meaning that they will not magnetically agglomerate at room temperature.[25] This is significant for applications where it is desirable to have the nanoparticles well dispersed in the sample matrix and easily manipulable by an applied external magnetic field. By exploiting the ability to remove the magnetic nanoparticles from solution with an external field and the ability to tailor the surface functionality of the nanoparticles through synthetic means, it is possible to both separate and detect with great sensitivity a wide range of heavy metal analytes. We will focus our discussion on the attachment of small molecules for the purposes of both separating the target analyte from complex samples containing interferents as well as detecting them once separation is complete. In doing so we hope to demonstrate the efficacy and future potential of magnetic nanomaterials for the effective preconcentration and sensing of environmentally relevant heavy metal analytes from complex sample matrices (e.g. river, ground, and ocean water).

Iron oxide nanoparticles are the most commonly used superparamagnetic nanoparticle for these applications since the materials can be made cheaply, in large quantities, and methods for the surface functionalization of the materials are well established.[20,23-25-36-39] The iron oxide core can be made using a variety of methods depending on the desired size, dispersity, and magnetic characteristics. The surface can be further modified to contain the thiol functionality necessary for the intended application. In some cases applications may require exposure of the nanoparticles to harsh chemical environments necessitating encasement of the nanoparticles in an inert shell, typically silica. Silica encasement of iron oxide nanoparticles is a common treatment to render the material more robust in low pH or biological environments and has the advantage of the silanol surface chemistry for silane ligand modification.[40-44] Noble metals are also used for encasement of

the iron oxide core depending on the application. For example, gold or silver encasement allows one to take advantage of both the magnetic and optical characteristics (e.g. plasmon resonance due to the metallic shell) of the core-shell materials when concentration and detection of the materials is desired.[45-57]

In our work we have demonstrated that functionalized superparamagnetic nanoparticles can effectively disperse in aqueous environmental samples and sequester a wide variety of analytes including heavy metals.[33-34] Specifically, we have employed thiol-modified Fe_3O_4 nanoparticles that are approximately 6 nm in diameter to remove Hg, Ag, Pb, Cd and Tl from natural waters (i.e. river, ground, and ocean water). These materials are described below in Figure 5. The magnetic nanoparticles used in this study have the distinct advantage that they are highly dispersible in aqueous media, but they can be removed with relative ease by exposing the sample to a magnetic field. In this case the field strength that was used was ~1.2 T generated by a NdFeB rare earth magnet.[34] Using this setup it was shown that the nanoparticles could remove over 99 wt% of 1 mg/L Pb within 1 minute of contact time and that they have a Hg capacity of over 227 mg/g, a 30-fold larger capacity than conventional resin-based sorbents.[34] In order to determine the efficacy of extraction of heavy metals by the magnetic nanoparticles a variety of measurements to determine the distribution coefficient (K_d) were made as summarized in Table 2 above. Figure 6 illustrates that at near neutral pH in river water, the thiol-modified magnetic nanoparticles are outstanding sorbent materials for soft metals such as Hg, Ag, Pb, Cu, and As (K_d > 50,000). In addition, the
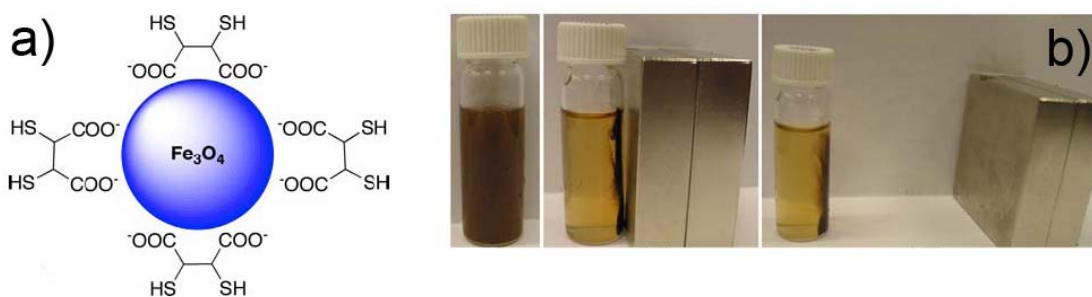
Figure 5. Schematic of (a) DMSA-modified Fe_3O_4 nanoparticles, and (b) removal of the nanoparticles from the liquid phase using NdFeB magnets; initial solution (left panel), after 10s with the magnet (middle panel), and when the magnet was moved to a distant position (right panel). Reprinted from reference 58 with permission from The American Chemical Society.

materials were demonstrated to be a good sorbent for harder metals such as Cd, Co, and Tl.[34] Once the metals were extracted, the trace detection of the heavy metal analyte was carried out using ICP-MS after contact with the magnetic nanoparticles.[34]
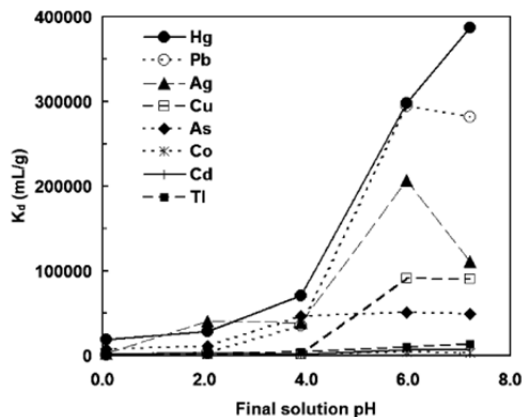
Figure 6. Effect of pH on the K_d values of Fe_3O_4 nanoparticles, measured in HNO_3 spiked unfiltered river water (L/S, 10^5). Reprinted from reference 34 with permission from The American Chemical Society.

Studies from other groups have shown similar characteristics of functionalized magnetic nanoparticles and microparticles modified with a wide variety of affinity ligands for the extraction of heavy metals from environmental samples.[59-62] However, due to the need to fully understand the behavior of the materials when dispersed in the environment (e.g. tendency toward aggregation and/or decomposition as well as mobility), this field still remains relatively undeveloped when one is discussing the use of superparamagnetic nanoparticles between 5-20 nm in diameter. There are more references to the use of microparticles (mostly constructed from nanoparticle/polymer composites), but these materials fall well outside of the size range of what is traditionally considered a nanomaterial (i.e. they have sizes > 100 nm).[60] In addition to the magnetic nanoparticles, there has been a great deal of attention given to nanoporous materials such as silica ceramics (pore size on the order of ~ 3-6 nm but particle size on the order of microns) for the removal and remediation of contaminants from natural waters due to their high surface area and relative ease of functionalization.[34, 63-66] However, even though these materials are outstanding contaminant sorbents, they suffer from the intrinsic mass transport limitations of moving the large volumes of water to the sorbent material. Alternatively, other high surface area sorbents that can be surface functionalized and that are more readily dispersible in aqueous systems, but that can be easily recovered once bound to the target analyte offer significant advantages for many applications.

Materials such as magnetic nanoparticles and polymer/nanoparticle composites offer the unique capability for magnetically directed separation and sensing processes.[67-70]

Our group has demonstrated the use of both magnetic and nonmagnetic high surface area sorbent materials to enhance the electrochemical detection of toxic heavy metals from natural waters.[33,58] The sorbent materials, either functionalized magnetic nanoparticles or mesoporous silica, were modified with a wide range of thiol containing organic molecules that possess a high affinity toward heavy metals (e.g. Hg, Pb, and Cd) and placed or collected at an electrode surface (Figure 7). Using these high surface area sorbent materials, we have been able to demonstrate sensitive electrochemical detection of environmentally relevant heavy metals in complex environmental (e.g. river water) and clinical samples (e.g. urine). Superparamagnetic Fe_3O_4 nanoparticles functionalized with dimercaptosuccinic acid (DMSA) like those discussed above were used to first bind the heavy metal contaminants from complex samples and then subsequently carry them to the surface of a magnetic electrode as shown in Figure 7.
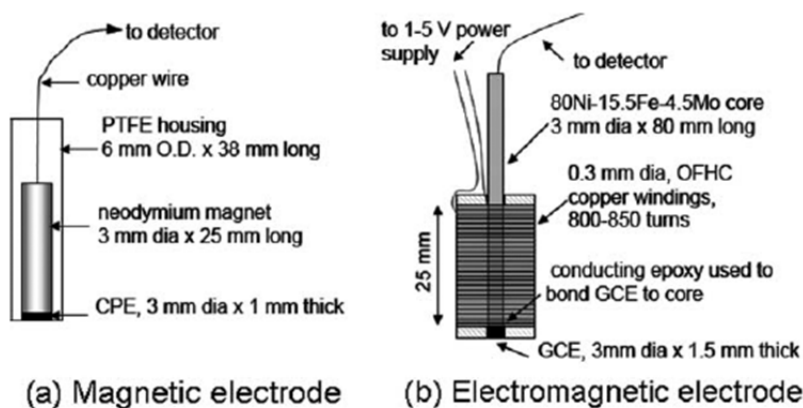
Figure 7. Schematics of (a) magnetic electrode and (b) electromagnetic electrode which concentrate metal ions using superparamagnetic nanoparticles. Reprinted from reference 58 with permission from The Royal Society of Chemistry (RSC).

By using an applied magnetic field to remove the target analytes from solution prior to electrochemical analysis, they are effectively isolated from the huge number of potential interferents present in complex sample matrixes. Using this system we have successfully overcome, at least to some extent, two of the biggest problems that prevent widespread adoption of electrochemical sensors for the analysis of metal ions in biological samples, which are (1) the binding of the target metals to proteins present in the sample matrix leading to a lowered signal

response and (2) electrode fouling caused by proteins. As can be seen from Figure 8, we have successfully measured concentrations of Pb in rat urine as low as 10 ppb with as little as 20 seconds of preconcentration (after 90 seconds of preconcentration, which is optimal, the detection limit was 2.5 ppb Pb). Further, Figure 9 shows that the magnetic nanoparticles are also capable of enabling the detection of multiple heavy metals (i.e. Cd, Pb, Cu, and Ag) from a variety of natural waters with only ~2.5 minutes of preconcentration time.

In addition to this work a number of other groups have reported the use of magnetic nanoparticles in the electrochemical analysis of other environmentally relevant targets (e.g. proteins and nucleic acids) besides heavy metals.[21,22,71] It is important to point out that even though the bulk of the work that has been performed in this area was aimed at clinical applications, the detection of biological species is of paramount importance to environmental sensing due to the fact that many common environmental contaminants are of biological origin.[73] A recent example that employs magnetic nanomaterials for the detection of a protein biomarker to pesticide exposure utilizes a similar magnetic electrode as described above and shown in Figure 7.[74] In this work, the magnetic particles have been bound with gold nanoparticles to provide an extremely responsive material for electrochemical analysis.[74-75] These composite nanomaterials have been used to bind and separate protein biomarker targets from solution followed by the detection without the need for any type of amplification typical to protein detection.

The use of magnetic nanoparticles in trace analyte optical detection scenarios has also received a great deal of attention in the recent literature with reviews by Corr, et al. and Katz, et al. going into great depths on the formation of nanomaterial composites for biological detection and biomedical applications.[81,21] However, it is important to note that the bulk of reported detection schemes center on the use of magnetic nanoparticles in electrochemical assays. This is because even when one considers all of the potential benefits associated with using a fluorescent nanomaterial that also is magnetic (e.g. ability to separate bound analyte from a sample and monitor the process optically), there are many complications that can arise. Primarily, the use of materials such as magnetic nanoparticles in an optical detection platform can scatter, absorb, or even quench the optical signal from the fluorescent reporter leading to a decrease in signal output. Despite these limitations, magnetic/fluorescent materials have great promise in environmental sensing because they will enable one to separate/concentrate a target analyte from a complex sample prior to analysis preventing unwanted optical noise from background interferents. Concurrently, these

materials will optically label the target analyte upon binding allowing for rapid sample analysis using traditional optical methods that have exquisite sensitivity after the separation is complete. We believe that as the materials production methods continue to mature and more magnetic/fluorescent composite nanomaterials become available there will be an explosion in the use of these types of materials in environmental sensing applications.
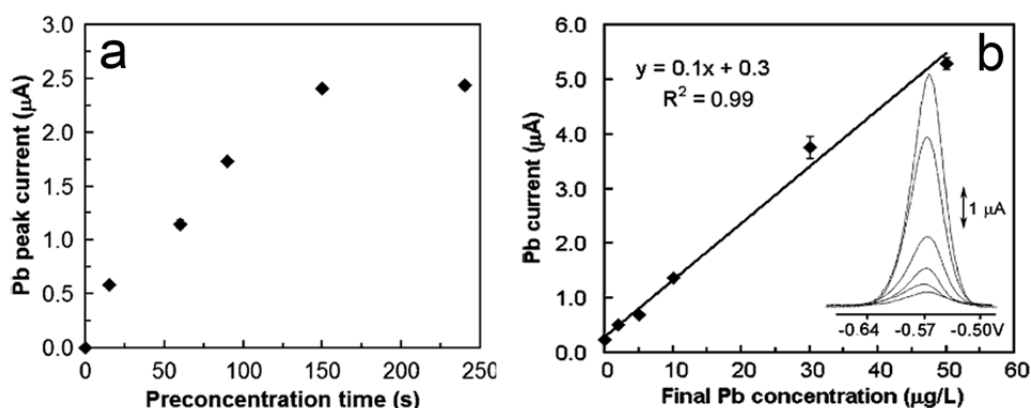
Figure 8. a) Signals of 10 ppb Pb measured at DMSA–Fe$_3$O$_4$-magnetic sensors in samples containing 25 vol.% of rat urine with varied preconcentration time and b) Linear Pb calibration curve measured at DMSA–Fe$_3$O$_4$ magnetic sensors in Pb-spiked samples containing 25 vol.% of rat urine. Reprinted from reference 58 with permission from The Royal Society of Chemistry (RSC).
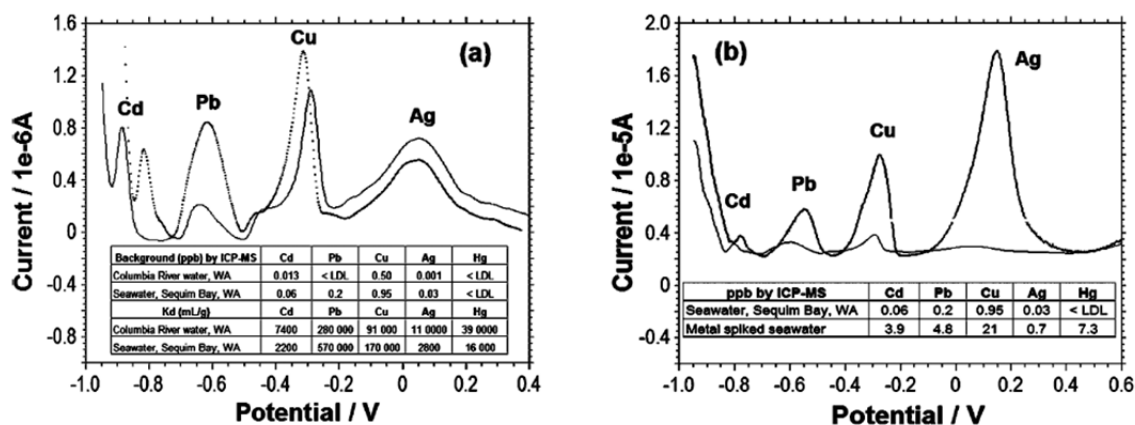
Figure 9. Sensor measurements of (a) background metal ions in seawater (dashed line) and river water (solid line) and (b) background metal ions (thin line) and metals spiked (thick line) in seawater, after 150 s of preconcentration time. Inset shows the metal concentrations, measured with ICP-MS, and the distribution coefficients of multiple metal ions (S/L of 0.01 g L−1 of DMSA–Fe3O4, initial metal conc. of 500 ppb each, pH of 7.20 for river water and 7.64 for seawater). Reprinted from reference 58 with permission from The Royal Society of Chemistry (RSC).

4. Nanoporous Carbon Based Sorbent Materials

Activated carbon is arguably the oldest, and most widely utilized sorbent in human history.[76] Activated carbon has been around since antiquity and has grown into a major industry today, enjoying sales of many hundreds of millions of dollars each year. Activated carbon has a number of features that are attractive for pre-concentration of analytes from aqueous systems – it is affordable, widely available, has high surface area, open pore structure, is stable towards hydrolysis, has good chemical stability, and excellent thermal stability. Activated carbon is widely used in the removal of a variety of contaminants from water in municipal drinking water purification (e.g. chlorocarbons arising as a by-product of the chlorination process).[77] The utility of activated carbon as a sorbent material is centered around its ability to capture a wide variety of chemical species. Such non-specific adsorption is not necessarily desirable for analytical pre-concentration as it entrains many other species that are not of interest and wastes valuable capture capacity doing so. Chemical selectivity can be very valuable for analytical pre-concentration.

There have been numerous efforts over the years to chemically modify activated carbon in an effort to enhance its capture efficiency for specific analytes. Many of these efforts have involved some sort of controlled oxidation, or acid treatment as a way to increase the degree of oxygenation of the carbon backbone. For example, activated carbon treated with sulfuric acid has been used to adsorb pollutants from wastewater.[78] Activated carbon has also been treated with various oxidants to enhance its adsorption capacity. Treatment of granular activated carbon with potassium bromate was found to enhance the sorption of Ni ions.[79]

Numerous studies have used chemically modified activated carbons to capture a wide variety of metal ions from aqueous environments. Various activated carbons have been used to capture chromate from wastewater.[80] Similarly, various activated carbons' capture efficiency for Ni(II) has been systematically compared.[81] Selective sorption of Pt(II) from a mixture of metals in solution was also studied using chemically modified activated carbon.[82] Likewise, toxic metals like Pb(II), Cd(II) and Cu have all been concentrated from aqueous media using carbon-based sorbents.[83,84,85] Activated carbons have even had polymer chains intercalated into their porous architectures in an effort to enhance their ability to bind toxic heavy metals.[86]

Chemically modified activated carbons have been used for the pre-concentration of specific analytes for water quality analysis. For example, various trace level toxic elements have been

concentrated from water samples for analysis by neutron activation.[87,88] This area was recently reviewed.[89]

Clearly, activated carbon is a broad-scale sorbent, capable of sorbing a wide variety of analytes, and when sampling natural waters this can lead to undesirable fouling and competition issues. Therefore, it would be desirable to install specific ligands (as opposed to generic "activation") inside the carbon scaffold so that some element of chemical selectivity might be enjoyed in these efforts.

Simple ligands have been installed on the carbon backbone to enhance metal binding affinity. For example, activated carbon has been sulfonated to produce a sulfonic acid that has been shown to be effective for ion exchange.[90] Activated carbon has also been nitrated, and the nitro groups subsequently reduced to amines, which were then used as anchors to capture a variety of transition metals and lanthanide ions from aqueous media.[91]
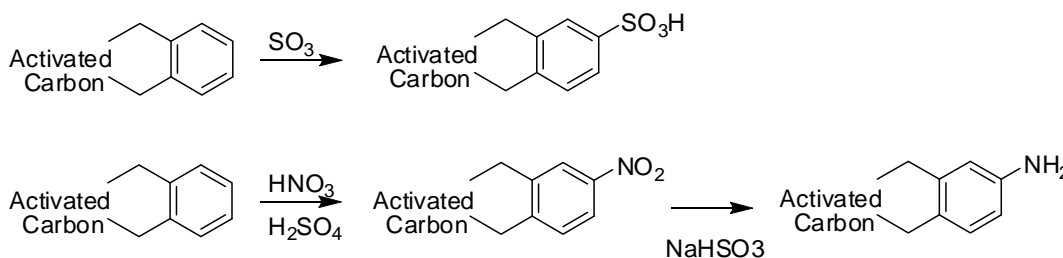
Scheme 1. Sulfonation of activated carbon (above) and nitration and subsequent reduction of activated carbon.

More recently, activated carbon has been chloromethylated, analogous to the synthesis of the polymeric system known as Merrifield's resin.[92] Chloromethylation allows for the easy introduction of a wide variety of chemical functionality through simple substitution reactions. In this case, the chloride was displaced by a sulfur-containing nucleophile, and the resulting thiolated activated carbon was shown to be an effective, and selective, heavy metal sorbent.[93] The performance of thiolated nanoporous carbon ac compared to conventional activated carbon is shown in Table 4. The thiol functionality improves the affinity of the material for softer heavy metals. It should be pointed out that a portion of the functionality appears to be located inside micropores (an inherent limitation of activated carbon) and therefore has limited chemical accessibility.

Activated carbon → Activated carbon (CH₂Cl) → Activated carbon (CH₂SH)
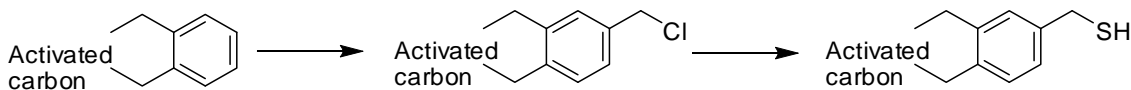
Scheme 2. Preparation of thiol-functionalized activated carbon by chloromethylation followed by substitution.

More sophisticated chelating N,N'-bis(salicylidene)-1,2-phenylenediamine ligands have also been installed in activated carbon and used to capture trace levels of copper from aquatic media and subsequent analysis.[94] Moving to more and more sophisticated ligand design allows for greater and greater discrimination in the binding chemistry.

Sorbent	Final pH	Average Kd (mL/g sorbent)							
		Co(II)	Cu(II)	As(III)	Ag(I)	Cd(II)	Hg(II)	Tl(I)	Pb(II)
Ac-CH₂SH	0.17	280	260	180	1700	0	1.6×10^6	96	91
	2.02	160	260	78	1400	83	1.1×10^6	19	120
	4.31	120	2100	0	5800	270	1.8×10^6	110	1500
	6.37	1100	5.5×10^4	160	6.2×10^4	1400	2.2×10^6	560	8.6×10^4
	7.33	1900	1.0×10^5	0	3.4×10^5	5000	6.1×10^6	1500	1.2×10^5
	8.49	2100	8.8×10^4	0	4.1×10^5	4300	2.0×10^7	1700	1.1×10^5
Activated Carbon	2.12	0	55	0	220	0	2600	73	170
	4.22	110	5400	0	820	170	4800	250	6600
	7.61	1300	5.3×10^4	23	3400	2900	9700	1800	6.7×10^4

Table 4. K_d values of metal sorption by thiolated activated carbon (AC-CH₂-SH). All experiments were performed in triplicate and averaged. Reprinted with permission from reference 89.

The approach of chemically modifying activated carbon has the advantages of being simple and direct, and uses a substrate that has high surface area and is readily available in bulk, but this approach is limited due to the microporosity inherent to activated carbon, as well as the latent functionality of the activated carbon backbone (e.g. carboxylic acids, phenols, ketones, etc.), both of which will provide non-selective metal ion (and organic) sorption, and therefore a significant amount of undesirable competing adsorption. Clearly, it would be advantageous to work with a carbon scaffold with large pores that were constructed around specifically tailored functionality.

In recent years a great deal of effort has gone into the study of templated mesoporous carbons.[95-106] This approach generally uses a templated mesoporous silica as scaffold upon which some suitable organic precursor is arrayed, and subsequently polymerized, then carbonized (typically at 800-1000°C). After the carbonization stage, the silica template is generally removed

via digestion with either HF or NaOH, leaving a free-standing nanoporous carbon scaffold that is structurally related to the original silica template.

Because of the high temperatures involved in the carbonization stage, this synthetic strategy tends to have very little flexibility in terms of functional "handles" that can be used to bind metal ions, or other analytes. A clever solution to this has been reported by Mokaya and co-workers in their syntheses of N-doped mesoporous carbons.[28-30] In this work a stream of acetonitrile (CH_3CN) vapor is entrained in an inert atmosphere and passed through a tube furnace (generally at 900-1100°C) containing a sample of the silica template. The acetonitrile is carbonized on the silica surface, and the resulting mesoporous carbon was found to contain ~8% N, with a surface area of ~1000 m^2/g, and a pore volume of 0.83 mL/g. XPS analysis of this material suggests that the N functionality is a mixture of "pyridine-like N" and quaternary ammonium salts. Use of these materials as a sorbent to capture metal ions and other analytes has not yet been demonstrated, but pyridine ligands are well-known to bind metal ions and quaternary ammonium salts can be used for anion exchange.

High surface area N-containing mesoporous carbons have been made using other strategies as well. It is possible to start off with the N-containing arene intact, and polymerize the heteroaromatic precursor. For example, 1,10-phenanthroline is a diamine that is well-known to chelate a variety of transition metal cations.[107] Utilization of this material in the synthesis of templated mesoporous carbon yields a product that had a surface area of approximately 870 m^2/g and 30-35 Å pores.[108] Due to the reluctance of the 1,10-phenanthroline nucleus to undergo electrophilic aromatic substitution, this strategy was found to require temperatures of 700-800 °C for carbonization. As a result, N loss (which takes place above about 600 °C) was able to compete and these materials were found to contain ~5% N.[109] This material was found to have excellent chemical and thermal stability, and was shown to be an effective sorbent for transition metal cations.
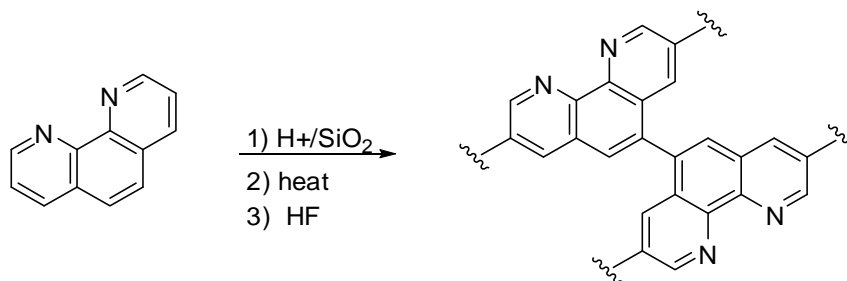
Scheme 3. Formation of N-functionalized activated carbon from 1,10-phenanthroline.

High surface area pyridine-based mesoporous carbons have also been made using the cyclotrimerization of diethynylpyridines by taking advantage of the high reactivity of the acetylene group.[110] The structure of the products obtained from this approach were found to be dependent on the regiochemistry of the acetylene groups on the pyridine precursor. The best results were obtained with the 2,5-diethynylpyridine precursor, which gave a product with a surface area of 1930 m^2/g, a pore volume of 2.14 mL/g, and ~4% N. These high surface area pyridine-based materials have not been evaluated as pre-concentration sorbents, but should be useful for capturing transition metal cations, organic acids, and trigonal (or tetrahedral) anions.
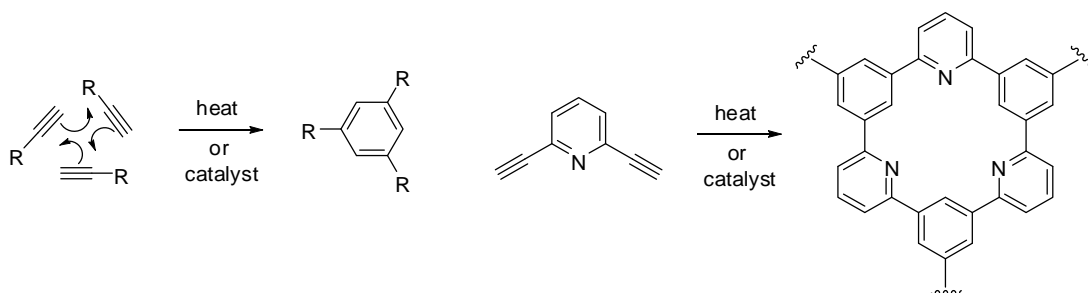
Scheme 4. Synthesis of high surface area N-functionalized mesoporous carbon *via* cyclotrimerization of diethynylpyridines.

The primary limitation on this synthetic strategy is the high temperature required for the polymerization/carbonization process. At temperatures above 600 °C, pyridine rings undergo ring-ring fusion reactions and N is lost.[109] Therefore, it would be desirable to use more reactive polymerization chemistry in an effort to get these temperatures down as low as possible in order to preserve as much of the N functionality as possible. $SiCl_4$ catalyzed cyclotrimerization of the commercially available 2,6-diacetylpyridine inside an SBA-15 template has been shown to result in a mesoporous carbon at temperatures as low as 600 °C.[110,111] The product was found to have a surface area of 1275 m^2/g, 35 Å pores, and contain 6.8% N. Again, this pyridine-based nanoporous sorbent should be useful for capturing transition metal cations, organic acids, and (in protonated form) trigonal or tetrahedral anions.

Other heteroaromatic precursors can also be used in this chemistry. For example, acid catalyzed polymerization of 2-thiophenemethanol inside an SBA-15 template, and subsequent carbonization of the intermediate product at 700-800 °C was found to create a S-functionalized mesoporous carbon.[112] The sulfur content, surface area, and pore volume were found to be dependent on the

carbonization temperature, but between 700-800 °C, the sulfur content was 4.9-7.2%, the surface was 1620-1930 m^2/g, and the pore volume was 1.68-2.14 mL/g. Like all mesoporous carbons, these S-FMCs were found to have excellent thermal and chemical stability; boiling them in buffers from pH 1 to pH 13 for 24 hours induced no discernible change in these nanoporous sorbents. Indeed, these S-FMCs were found to be effective heavy metal sorbents. K_d values for Hg^{+2} were greater than 250,000 over the same broad range of pH (1 to 13). Very few heavy metal sorbents are capable of effective metal capture over such a wide range of pH.
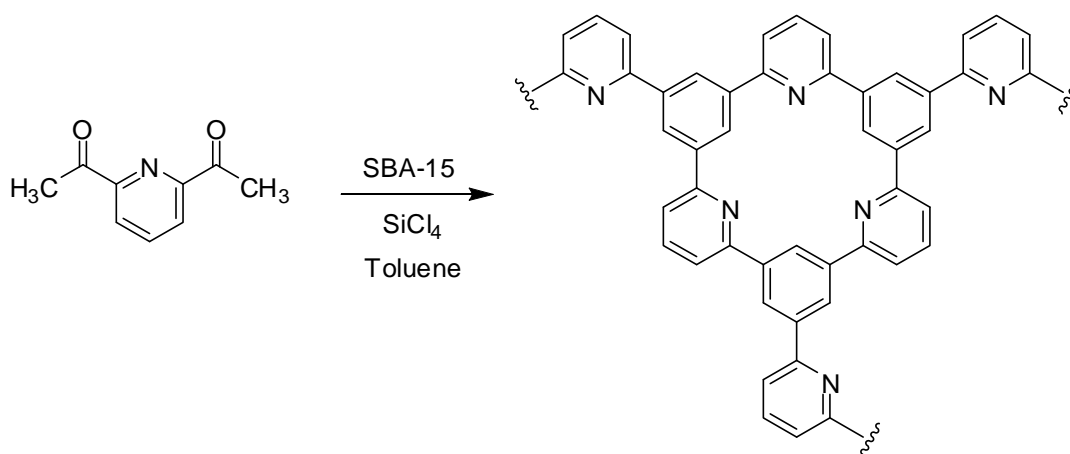
Scheme 5. Preparation of N-functionalized mesoporous carbon using an SBA-15 template.
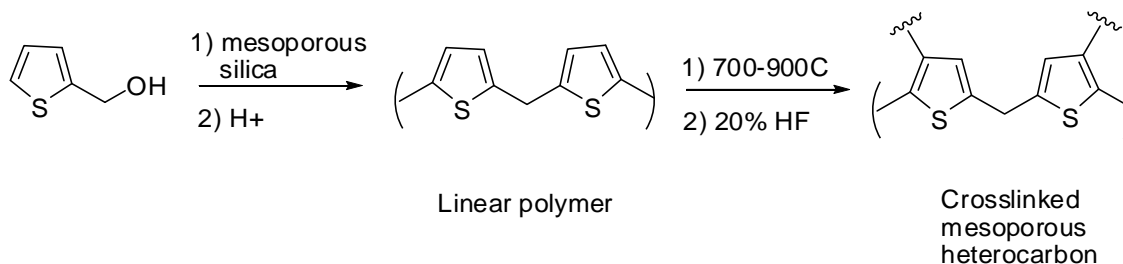
Scheme 6. Synthesis of S-functionalized mesoporous by polymerization of thiophenemethanol followed by crosslinking.

One of the advantages of carbon based sorbents is their chemical stability and resistance to chemical degradation. Unfortunately, the chemical stability of these materials also translates into resistance to several commonly used forms of chemical functionalization. Such chemical functionalization is needed to augment their poor selectivity. Chemical selectivity is desirable for

analytical preconcentration applications (and also in remediation applications) so as not to consume the sorbent's capacity to bind non-target species. Installation of specific ligand chemistries (e.g. thiols, thiophenes, chelating diamines, etc.) helps to overcome this. These solutions preserve the chemical stability of the carbon backbone while adding chemically selective ligands with improved affinity for metal species, and extend the usefulness of carbon-based sorbents beyond that of a general sorbent.

5. Other Nanostructured Sorbent Materials

5.1. Zeolites

Zeolites are aluminosilicate materials which exhibit well defined, highly porous structures. They occur naturally and may be prepared by several methods. The general zeolite structure is a three-dimensional network of repeating isomorphous SiO_4 and AlO_4^- tetrahedra linked by oxygen atoms. This yields an anionic lattice with acidic (bridging OH groups on Al-O-Si linkages) and basic (Al tetrahedra) sites. Charge balance is maintained by extra-lattice Na(I), K(I), Ca(II), or Mg(II) atoms. To date, there are over 40 known naturally occurring zeolites which differ in structure and in Al:Si ratio (Figure 10).[113] Small amounts of Fe are also found in natural zeolites.[114] Zeolites are widely used in both separation and catalysis applications.[115]   Like activated carbon materials, zeolites are commonly employed as general sorbents.[116] Their high surface area allows removal of organic species from solution although their effectiveness as sorbents for organic species is limited compared to that of activated carbon materials. Their anionic framework makes zeolites natural cation exchangers while their well-defined pores lend some degree of preference to the ions absorbed. The most widely-used and studied natural zeolite, clinoptilolite, exhibits a general selectivity: Pb(II) > Cd(II) > Cs(I) > Co(II) > Cr(III) > Zn(II) > Ni(II) > Hg(II).[117] Clinoptilolite is also effective in sorption of Sr(II) and Sb(II).[118,119] Other natural zeolite materials may differ in selectivity. For instance: scolecite follows the series Cr(III) > Mn(II) > Cd(II) > Ni(II).[120] This selectivity is desirable for adsorption of these analytes at trace levels in matrices which contain competing species.
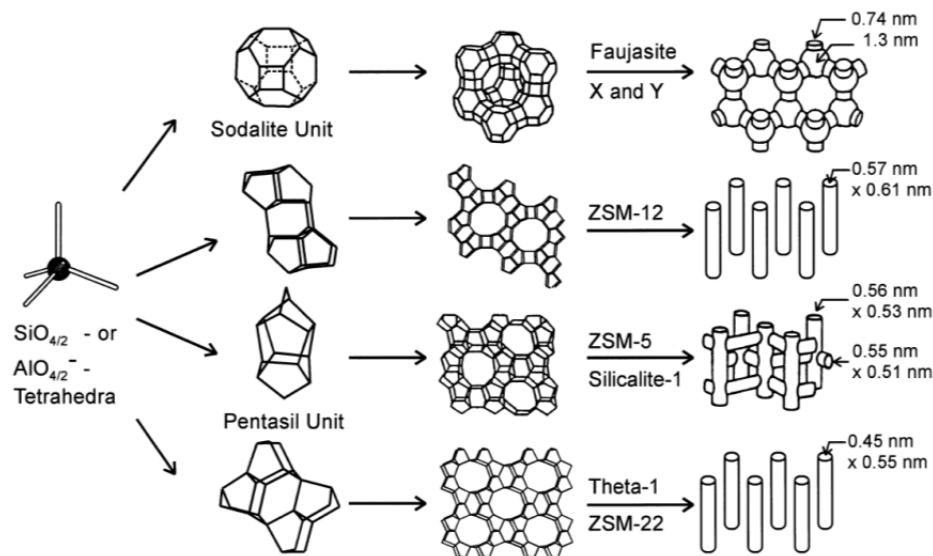
Figure 10. Structures, pore shapes, and dimensions of several zeolites. Figure reprinted with permission from reference.[121]

Adsorption of metals by zeolites is governed by pH, temperature, and is made further complex by the different surface sites found within the lattices. pH affects not only the state of lattice hydroxyl groups and metal speciation but at very low pH protonation of surface sites reduces the lattice affinity for positively charged species.[122]

Analysis of adsorption isotherms indicates that adsorption of metal cations occurs via both ion exchange and chemisorption processes. Both processes are involved in adsorption of many metals. For Pb(II) and Zn(II) ion exchange occurs quickly and is followed by slower chemisorption.[119,123,124] In most cases, sorption favors cations with higher charges and smaller radii.[125]

Adsorption occurs most effectively for metals that exist as cations. Because they have little affinity for the anionic lattice, metals which form oxoanions or other anionic species are not as effectively adsorbed. Organic contaminants such as phenol that form complexes with metal ions interfere to various degrees with metal sorption.[126] It is likely that these metal-ligand complexes hinder penetration into pores or form neutral or anionic complexes which have no affinity for anionic lattice. In some cases, the sorbent may be regenerated in solutions with high concentrations of competing cations such as $NaNO_3$ solutions. Acid may be used to remove adsorbed metals, although this has been shown to damage some zeolites.[122]

Natural zeolites may be modified in order to enhance their ability to absorb anionic species. When treated with Fe(II) and Fe(III) nanoparticles, these functionalized materials show impressive affinity for arsenate and arsenite anions compared to the native zeolite.[127,128] Fe(II) is also used to treat activated carbon to the same effect.[127] An Al-functionalized zeolite has also been shown to remove arsenate.[129] Small sizes of natural zeolite pores (typically between 0.4 and 1.2 nm) lends them their selectivity and high surface area but limits their use in adsorption of larger molecules, restricts mass transport through the material, and can result in high back pressure in flow systems.[130]

Synthetic zeolites have been designed in an effort to prepare zeolites and zeolite-like materials without the limitations of natural zeolites. Two strategies have been explored: 1) making zeolites with larger pores and 2) inserting larger pores into zeolite materials. These modified zeolites have been reviewed recently.[131,132] Synthetic mesoporous zeolites may possess different metal selectivity profiles than their natural counterparts. However, little work has been done involving synthetic zeolites as sorbents.

Like activated carbon materials, zeolites are low-cost, high surface area, semi-selective sorbents. Their selectivity can be tailored by modifying lattice constituents, by functionalizing the lattice, or by changing the porous network topology. Like the functionalized nanoporous materials discussed in this section, the high cost of functionalization renders the more sophisticated materials less practical as sorbents for remediation but makes them ideal for detection applications.[133]

5.2. Ion imprinted polymers

Molecular imprinting is a technique for preparing polymeric matrices which are capable of highly selective phase extraction. Imprinted polymers are prepared by polymerizing functional and often crosslinkable monomers in the presence of an imprint molecule (Figure 11). This preparation of imprinted polymers is typically divided into three steps. During an imprint step, functional monomers form a complex with the imprint molecule which either closely resembles or is identical to a target analyte. The monomers are then crosslinked during a polymerization step. This fixes their position and orientation in the network. The imprint molecule is then removed during a leaching step. The polymer network is left with functional monomers pre-organized in a geometry optimum for binding the template molecule.

Ion imprinted polymers recognize metal ions after imprinting. The first ion imprinted polymer was developed by Nishide et al in 1976.[135,136] These early poly(4-vinlypyridine) resins could be imprinted to preferentially adsorb Cu(II), Ni(II), Hg(II), Zn(II), and Cd(II). Since then, efforts have been made to selectively bind different metals, improve the efficiency of absorption, and develop robust, regenerable imprinted polymers. Many of these efforts have involved incorporating metal-ligand complexes based on different chelating systems into polymer matrices. For example, carboxylic acid derivatized monomers have been shown to produce a resin specific to UO_2^{2+}.[137] 5,7-dichloroquinoline derivatives have been used as the chelating monomers for Dy and Sm – specific polymers.[138,139] A polymerizable 3-oxapentanediamide derivative was used in a polymer which could be used to separate Ca(II) from Mg(II) ions and vice versa.[140] Lemaire, et al used methacrylate monomers to selectively bind Gd and, in a similar polymer matrix, diethylene triamine pentaacetic acid (DPTA) derivative chelating monomers for La(III).[141] Prasada Rao, et al. have reviewed this topic recently.[134,142]
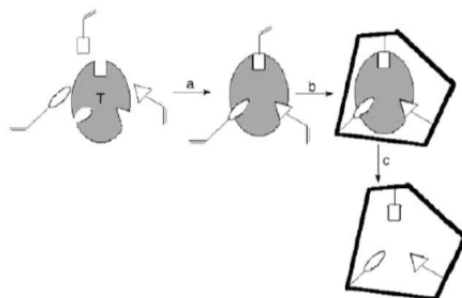
Figure 11. Representation of molecular ion imprinting process. a) complexation b) polymerization, c) leaching. T represents the imprint molecule. Reprinted with permission from reference 134.

Using more sophisticated ligands yields higher specificity and more efficient adsorption of target analytes. The synthetic challenges have been to incorporate these sophisticated chelate functionalities into polymerizable molecules. It is sometimes possible to circumvent this challenge by using both polymerizable and non-polymerizable ligands to form the template-ligand complex. The non-polymerizable ligands becomes trapped in the polymer matrix even after the template species is removed.[142]

Advantages of imprinted polymers are simple preparation, durability, predetermined and predictable selectivity. They may be used as bulk polymer, but are more effective when incorporated into nanostructured materials. Ion-imprinted polymers may be cast as thin films,

incorporated into membranes, or applied as coatings to solid supports.[128-132] Applying the polymer to a high surface area material eliminates the mass transport limitation involved in using the material in bulk. Drawbacks to ion imprinted polymers include poor solubility of the template (metal ion) in the imprinting mixture.

This section has outlined just two particular classes of material which are being explored for trace metal adsorption from aqueous matrices. There is tremendous room for development of zeolites, ion-imprinted polymer-based materials, and other nanoporous materials like aluminophosphate materials and metal organic frameworks as sorbents for trace-level metal contaminants. Practical utilization of these nanomaterials in trace level assay will depend upon the capability to tailor the materials into form factors that allow integration with devices and functionalize the surfaces to have high selectivity and affinity.

6. Summary and Bridge to Chapter III

This chapter has reviewed selected nanostructured materials, many with thiol functionalization, for the capture of softer heavy metals from aqueous systems for environmental sensing and separation applications. It has been shown that correctly constructed nano- and mesoscale sorbents can be superior to conventional sorbent materials. It should be reiterated that we chose to review only work employing thiol surface chemistry since this provides a highly effective means for the capture of many toxic heavy metals from aqueous systems and offers a useful baseline for comparing the performance of the various nanomaterials. Many other elegant surface chemistries exist and enable the application of nanomaterials to other analyte sets. Beyond simple performance, one remaining factor that merits discussion is the economics of using nanomaterials for collection and detection.

Nanostructured materials can be expensive. While industrial scale up can bring costs down, it does not address two fundamental problems: first, scaling the production volumes up from laboratory beakers to industrial tonnage is a nontrivial effort, particularly for advanced materials with complex structures. Second, the materials and methods needed to assemble sorbents with the useful nanostructure and surface chemistry will almost inevitably make them more expensive than bulk or traditional sorbent materials. For large scale applications of nanomaterials, the performance of the materials must be sufficient to merit the additional cost. Viability will have to be assessed on a case by case basis, but will likely be more successful on high

value applications such as those associated with radioactive materials or localized applications such as batch treatment. The much larger K_d and capacity values for functionalized nanoporous silica and nanoparticulate iron oxide shown in Tables 1, 2, and 4 suggest that, despite higher costs than tradition bulk sorbents, they may provide better value for select applications. Furthermore, the possibility of supramolecular modification of SAMMS and related nanomaterials (such as the chemisorbed Phenyl-SAMMS materials presented in Chapter III) provides a route to mitigate the cost of the nanomaterial by providing a greater product lifetime.

In contrast to large scale separations, analytical applications require much smaller volumes of sorbent materials. In most cases analytical applications will require only milligrams (or even micrograms) of sorbent material. Information obtained from analytical assays forms the basis for many high value decisions such as those made as a result of medical diagnostics, legal forensics, determination of clean water and food, or operation of an industrial process. Consequently, with high value results and small quantities of material needed, the cost of the sorbent material for analytical applications is less relevant than for large-scale applications. For analytical applications, getting a stable supply of materials with dependable performance and effectively integrating them into the analytical method/device is more important than the nanomaterial cost. For some nanomaterials, such as the quantum dot emitters and PANAM dendrimers, reliable industrial production and their widespread analytical utilization has already been demonstrated. As commercial sources of nanomaterials become increasingly available it is inevitable that they will be integrated in the products as appropriate, with high-value applications such as improved analytical devices/methods leading the way.

In conclusion, this chapter has discussed the material science and applications of functionalized nanoporous silica, functionalized superparamagnetic particles, nanostructured carbon based materials, and other structured materials such as zeolites. These materials only scratch the surface of meso- and nanoscale materials that can be employed in sensing and remediation applications. Additional materials that are presently under development, as well as others not yet imagined, will provide new and relevant capabilities enabling a range of analytical applications for trace level measurements. Chapters III and IV describe the development of new surface chemistries which will facilitate the production of new functional surfaces on a host of different material formats. In Chapter III we apply a novel supramolecular surface modification motif to mesoporous silica as well as the Fe_3O_4 nanoparticles which were introduced in this

37

chapter. Both materials are evaluated as sorbents and are capable of performance on par with the covalently functionalized materials discussed in the previous sections.

CHAPTER III

SUPRAMOLECULAR MODIFICATION OF SURFACES

VIA ARENE-ARENE INTERACTIONS

This chapter was co-authored by Timothy G. Carter, and Darren W. Johnson from the Department of Chemistry and Materials Science Institute, University of Oregon and R. Shane Addleman, of the Materials Chemistry and Surface Research Group, Pacific Northwest National Laboratory. Sean Fontenot prepared the chapter, designed and performed all experiments, and performed literature research and analysis. Darren Johnson, Timothy Carter, and Shane Addleman are responsible for development of this project and provided editorial assistance. Portions of this chapter excluding Section 2.3 will be submitted for publication.

1. Introduction

Access to clean drinking water and remediation of contaminated aqueous systems are of growing importance as global population and industrialization increase.[1,2] Removal of heavy metals, such as mercury (Hg), lead (Pb), and cadmium (Cd) from water is important because the presence of these contaminants, even at relatively low concentrations, has well documented adverse effects on the environment in general and human health in particular. Sorbent materials capable of selective separation of metal contaminants from aqueous systems have applications in improved industrial processing, monitoring and measurement, medical treatment, and environmental remediation.[3-11]

Construction of a sorbent material involves a series of trade-offs. Polymer and resin based materials are economical and have diverse chemistries but comparatively limited surface area and site density which result in lower capacities.[12-14] Porous materials with higher surface areas yield sorbent materials with greater capacity. Activated carbons, common and cost-effective sorbents,

have high surface areas but limited selectivity.[15,16] Porous silica materials have the advantages of high surface area, controlled pore structure, and rapid kinetics resulting from non-dendritic morphology. The porous silica surfaces are easily chemically modified using established silane chemistries.[17] Functionalized porous silica sorbents are chemically very flexible and can be created with a wide range of surface chemistries and material form factors.[18,19]

Functionalized mesoporous materials are generally excellent sorbents and have been prepared with various surface chemistries for toxic metal, metalloid, and oxyanion uptake.[20-22] Thiol- and sulfur-functionalized materials have excellent affinities for softer metals such as Hg, Ag, Cu, Cd, and Pb, and have been shown to enhance electrochemical detection of trace metal contaminants.[23-31]

The high affinity binding sites that provide these materials with unprecedented affinities also make them correspondingly more difficult to recycle since acidic or salt stripping of the bound contaminants and subsequent regeneration of surface sites generate significant amounts of chemical waste. On the other hand, one-time utilization of highly-engineered materials makes the relative cost high and consequently severely limits the economically viable applications of such materials for environmental remediation, industrial processes, and critical resource recovery. Our goal has been to explore non-covalent surface chemistries that will provide high performance, regenerable or recyclable sorbent material. Shifting from a single use material to a regenerable platform in which the silica support is recycled lowers the environmental and economic costs of the material while retaining the advantageous properties of engineered nanostructured materials. Supramolecular functionalization methods are important in their own right. Non-covalent attachment of organic molecules to surfaces allows one to avoid the necessity of optimizing the attachment for each class of organic molecules as well as avoid protection and de-protection procedures necessary to attach delicate or reactive functional groups to surfaces.

Our approach to creating a high affinity but non-covalently functionalized sorbent material has been to reversibly attach metal-chelating molecules to a functionalized, mesostructured support material. For applications in water remediation, this reversible attachment must yield a material which is stable to aqueous matrices but still be easily disassembled when desired. In previous work we have demonstrated such a material (general assembly is shown in Figure 1).[32] This first-generation material, although very effective in toxic metal ion uptake suffered from leaching of the active thiol layer into the aqueous matrices in which the material is designed to work.

This report follows an original communication providing a more comprehensive study and describing improvements to our initial successes. For this application, a surface of a phenyl-functionalized mesoporous silica (Ph-SAMMS) serves as an anchor layer that supports a secondary surface layer of thiol-bearing aromatic ligands which, in turn, present a high density of thiol sites to the interior of the material (Figure 1). We have modified Ph-SAMMS surfaces with several different thiol-bearing aromatic molecules resulting in three new sorbent materials. The resulting materials were evaluated for stability and effectiveness in removing Cd, Hg, Pb, and Ag from actual river water. We have also explored the effects of both the phenyl anchor density and the thiol surface density on the stability of the final material to aqueous matrices. We also demonstrate the use of Ellman's test for thiols to determine the free thiols available on functionalized nanomaterials. The Ellman's test was applied as an alternative to TGA for direct quantification of the density of the aromatic thiol layer. Our results show a set of materials which are as effective as the original benzyl mercaptan-functionalized Ph-SAMMS material but are much more robust toward leaching in aqueous environments. In order to demonstrate the arene-arene functionalization motif on a non-
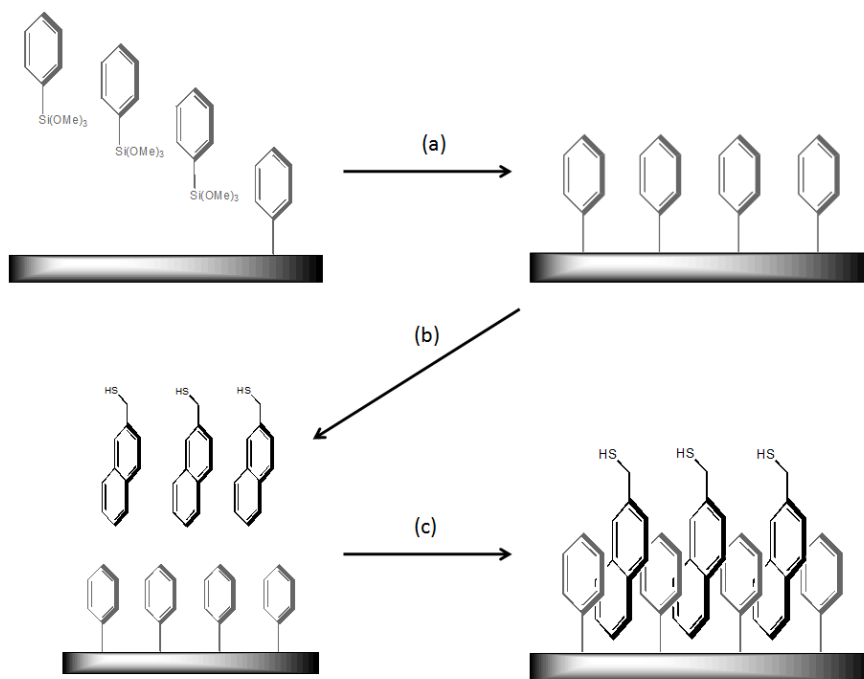
Figure 1. Preparation of Ph-SAMMS and supramolecular modification thereof. a) A phenyl layer is covalently attached to the MCM-41 surface yielding Ph-SAMMS. b) Ph-SAMMS is incubated with aromatic thiols. c) Slow evaporation yields a non-covalently functionalized thiol-bearing material which is effective for capture of Cd, Hg, and Pb. The orientations of molecules in this illustration are highly idealized.

porous material, we have prepared phenyl-functionalized Fe_3O_4 nanoparticles which exhibit surface properties nearly identical to those of non-covalently functionalized Ph-SAMMS materials. This work demonstrates a method of installation and characterization of a secondary surface upon a functionalized mesostuctured support. This method has application beyond thiol functional groups and could be applied to any water-stable functionality.

2. Arene-Arene Interaction Motif on Mesoporous Silica

General preparation of the materials presented in this report is illustrated in Figure 1. Phenyl silane molecules are covalently bound to the surface of the support structure, forming a uniform layer of phenyl rings (a). As a support structure, nano- or mesoporous silica (e.g. MCM-41) is advantageous due to its high area of kinetically accessible surface.[33,34] Ph-SAMMS is then incubated with aromatic thiols in an organic solution (b) and slow evaporation of the solvent yields a non-covalently attached thiol-bearing surface. The product material is then washed with methanol. The methanol wash separates solid material from any thiol component which simply precipitated during evaporation (as opposed to incorporating into the Ph-SAMMS material). The final sorbent material has been shown to be effective for capture of a range of heavy metal cations including Cd(II), Hg(II), and Pb(II) and the non-covalent linkage in the surface layer enables the active surface to be removed, recycled and replaced.[32]

Thermal gravimetric analysis (TGA) was used to determine the density of the phenylsilane layer. Pore size, determined by the Barrett-Joyner-Halenda (BJH) method, decreases as the extent of silanation increases (Table 1).[35] These reductions in pore diameter are accompanied by proportional reductions in surface area. This confirms that the pores have not been obstructed by oligomerization of the organosilanes and that the primary reason for the reduction in pore size is the addition of the phenylsilane units (Table 1).[36]

Phenyl silane coverage [Phenyl molecules nm^{-2}]	Surface Area [m^2 g^{-1}]	Mean Pore Diameter [Å]
2.43	390	17
2.22	400	17
1.60	550	19
0.72	730	27
0.34	770	31
0.06	875	34
0	1050	35

Table 1. Surface area and mean pore diamater for selected Ph-SAMMS. Surface area was measured using the Brunauer-Emmett-Teller (BET) method. As expected, surface area and pore are lower for more completely functionalized materials. The pore diameter measurements indicated the the reduced surface area is not due to obstruction of the pores by phenyl silane oligomers.

Porous materials present a challenge to characterization. While TGA provides useful information, XPS, XRD, or microscopy methods are often used for quantitative characterization of material surface components. However, most X-ray and microscopy methods are not effective in analyzing surfaces of highly porous materials. The Ellman's test for thiols is a quick and effective method for characterization of thiol-bearing materials. This colorimetric test was initially used to quantify cysteine residues on proteins.[37] By incubating thiol-functionalized silica materials with Ellman's reagent, we are able to quantify the number of thiol groups on the material surface. The Ellman's test was also used to measure the extent of secondary surface desorption into the aqueous matrix. This is done by simply incubating the material in a liquid matrix, removing the material by filtration, and then measuring the concentration of thiols in the filtrates.

2.1. Impact of scaffold (phenyl) layer density

In order to prevent leaching of the thiol secondary surface in aqueous matrices, the interactions between the scaffold and active layers must be much stronger than the thiol groups' propensity to enable solubilization of the semipolar molecule. We chose to explore these interactions by examining the effects of the density of the scaffold layer molecules on the MCM-41 surface as well as the density and identity of the thiol layer molecules.

The phenyl layer provides anchor points for the assembly of a secondary layer of aromatic molecules. In this fashion, the phenyl layer provides a scaffolding upon which to assemble the aromatic molecules that actually complex the target chemicals (i.e. heavy metals) of interest. The density of the phenyl rings affects the capacity of the Ph-SAMMS scaffold for SH-layer components

as well as the stability of the resultant material (Figure 2). Figure 2 shows the capacity for mercaptomethyl naphthalene of a series of Ph-SAMMS materials varying in phenyl density as well as the corresponding leaching of the thiol component of each sample. Regarding capacity for SH-layer components, increased phenyl density may be expected to provide increased capacity as the number of sites for interaction between surface aromatics and SH-layer aromatics increases with density. However, as seen in Table 1, materials with higher phenyl density have correspondingly smaller surface areas. This leads to significant reduction in capacity (both for the secondary surface layer and, by extension, for sorbates) for materials with very high phenyl density (2.4 phenyls per nm^2) compared to materials with moderate phenyl density (1.6 phenyls per nm^2). High phenyl layer density is associated with lower leaching. Presumably, this is because, at a high phenyl-density, the interior of the Ph-SAMMS pores provides a more hydrophobic environment than in low phenyl-density samples, and thus, is a more favorable environment for the hydrophobic aromatic thiols.
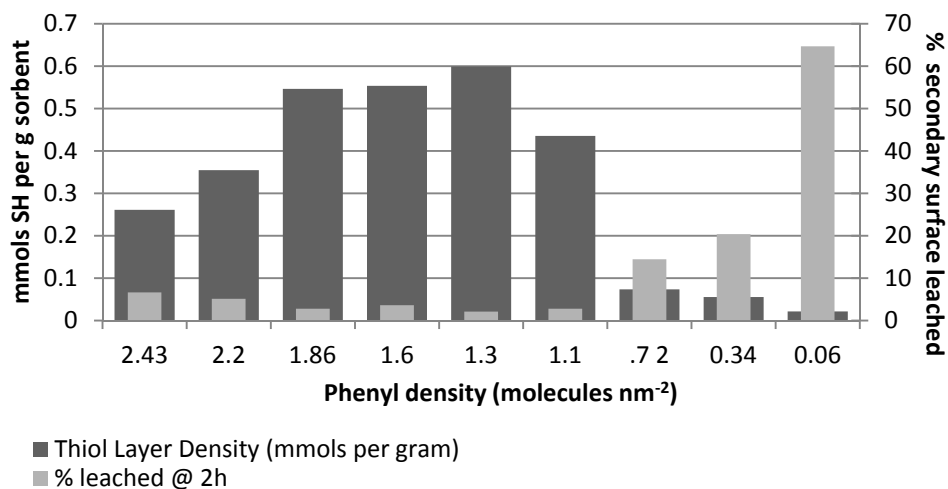
Figure 2. Comparative stability of materials prepared from Ph-SAMMS scaffolds of different densities.

2.2. Impact of density and identity of secondary surface components

The identity of the aromatic thiols used to make up the secondary surface layer has a significant effect on material stability (Figure 3). Benzyl mercaptan (BM) forms the least stable surface (34% leached after 2 hours in filtered Columbia River water) which is not surprising given its relatively high water solubility. 1,4 bis(mercaptomethyl)benzene (BMMB) shows reduced leaching compared to BM but still, loses up to 10% of the thiol surface under identical conditions.

Mercaptomethylnaphthalene (MN) which has very limited water solubility, forms the most robust secondary surface tested, leaching as little as 5%. All three non-covalently functionalized materials can be prepared with thiol densities similar or better than SH-SAMMS which indicates similar capacity and affinity for target cations (Figure 3).

The density of the secondary surface also affects the stability of the final material to aqueous matrices (Figure 4). Varying the amount of thiol component can increase the robustness of the secondary surface. Materials were prepared with less than 0.01 mmols thiol up to 0.11 mmols thiol per g on Ph-SAMMS with 1.3 phenyls per nm^2. These two examples leached 34% and about 5%, respectively. Presumably, more dense and complete secondary surfaces are more robust because hydrophobic aromatic thiols contribute to the overall hydrophobicity of the surface environment, making the more densely covered surfaces more favorable for hydrophobic species.
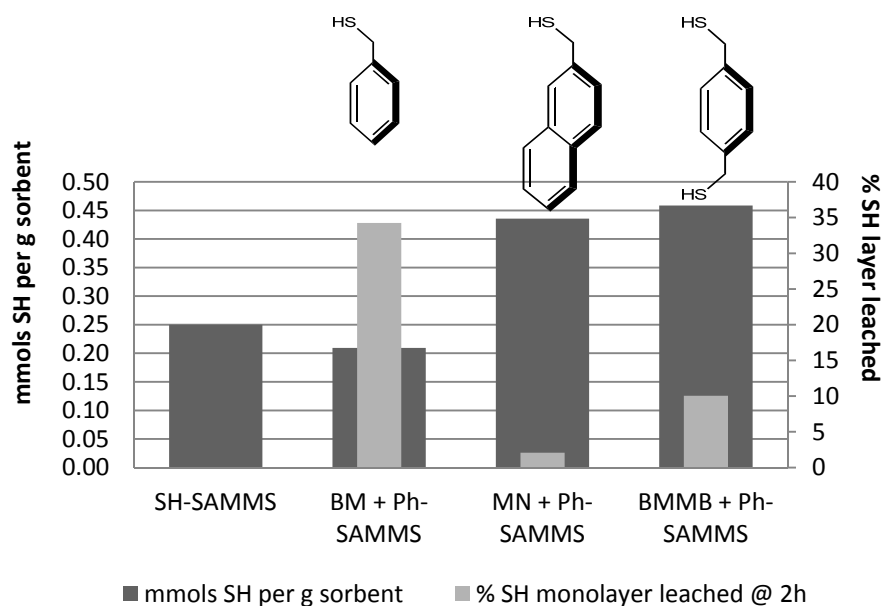
Figure 3. Comparative stability of materials based on secondary surface identity. Materials were produced with either benzyl mercaptan (BM), 2-(mercaptomethyl)naphthalene (MN), or 1,3 bis(mercaptomethyl)benzene (BMMB). As expected, the covalently functionalized SH-SAMMS showed no detectable leaching.
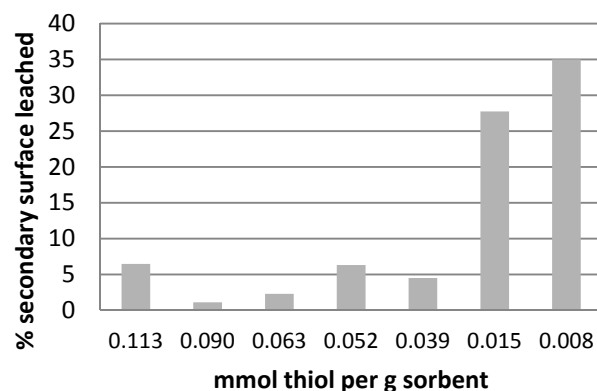
Figure 4. Comparative stability of materials based on secondary surface density. Materials were produced with varying amounts of SH layer component (MN).

2.3. Geometries of the scaffold and secondary surface layers

Identifying the geometry of the Ph-SAMMS – surface layer interface will be important in predicting the properties of new material designs. It is unknown at this point how functional groups are distributed on functionalized silica surfaces that are prepared via direct silanation (Chapter I, Section 3). Recent work indicates that the uniformity of distribution of post-synthetically functionalized mesoporos silica is dependent the solvent as well as the organosilane being deposited.[41] This work suggests that for incompletely functionalzied materials (i.e. Ph-SAMMS with less than about 1.8 phenyls per nm^2) prepared in non-polar solvents (e.g. hexane and toluene) the functional groups are deposited somewhat densely on the surfaces nearest the pore windows and less densely further toward the interior of the pores. However, the Ph-SAMMS system has not been investigated in this repsect.

Given the challenges of directly imaging our porous materials, we designed an experiment in order to obtain indirect evidence of surface geometry. Knowing that exposure to aqueous matrices would remove some, but not all, of the secondary surface, we used sublimation techniques to attempt to similarly distingusih between weakly and strongly bound secondary surface molecules. By carefully controlling pressure and temperature, we were able to remove all but the most stable configurations. We then analyzed these materials by TGA and the Ellman's test in order to determine the relative amount of secondary surface molecules remaining in hopes that the secondary surface:phenyl scaffold ratio would shed some light on the geometries of the two surfaces.

We investigated Ph-SAMMS scaffold materials with 0.36, 0.72, 1.30, 1.60 and 1.86 phenyls per nm^2 and prepared each of these scaffolds with four different amounts of secondary surface molecules. In all of these experiments mercaptometylnapthalene (MN) was used to make the secondary surface. Figure 5 shows the results of these experiments. The sublimation experiments showed that very low ratios (less than 1:10) were preferred and that these ratios varied with the Ph-SAMMS phenyl density. Very low phenyl density materials (0.34 and 0.72 phenyls per nm^2) had *higher* final secondary surface:scaffold ratios of about 1:10 while the more completely functionalized phenyl materials had final ratios of about 1:20.

Initially, we hypothesized that the secondary surface molecules would arrange in an interlocked configuration (Figure 6, image a) in which the seoncdary surface components would be present in a large ratio (1:2) relative to the scaffold molecules. It was clear from our first TGA measurements that we were not achieving this level of secondary surface coverage. We then reasoned that, if the phenyl density made this orientation impossible (i.e. the phenyl groups were too close together to allow interlocking of the secondary surface molecules) then other orientations (Figure 6) should be favored such as the "border configuration" (Figure 6, b) in which the phenyl and naphthyl groups interact in an offset face-face manner only near the outside of "islands" of
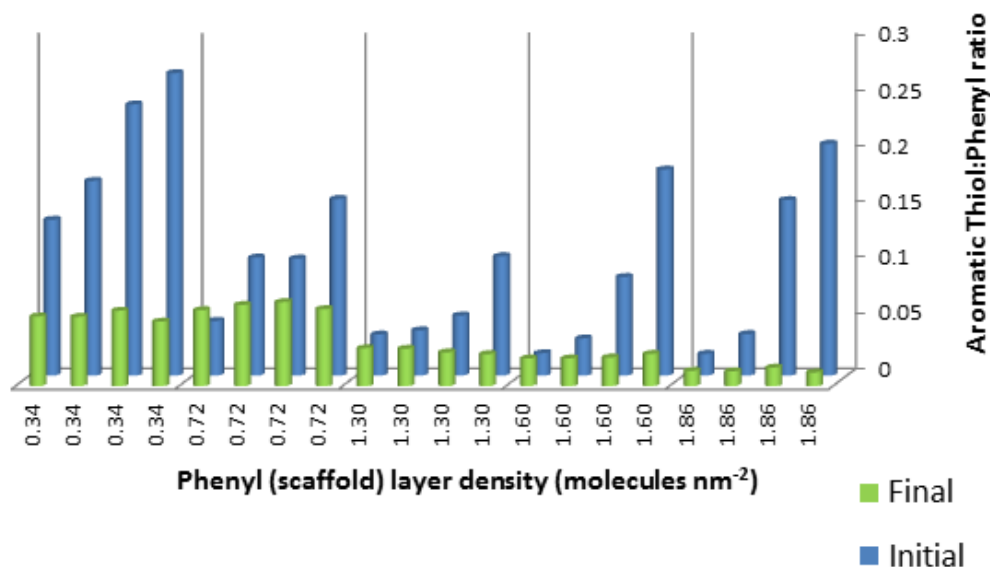
Figure 5. Secondary surface:scaffold ratio as a function of phenyl density. Blue bars indicate the initial secondary surface ratio and green bars indicate the secondary surface ratio measured after sublimation. Fixed ratios of less than 1:10 are obtained regardless of starting phenyl density.
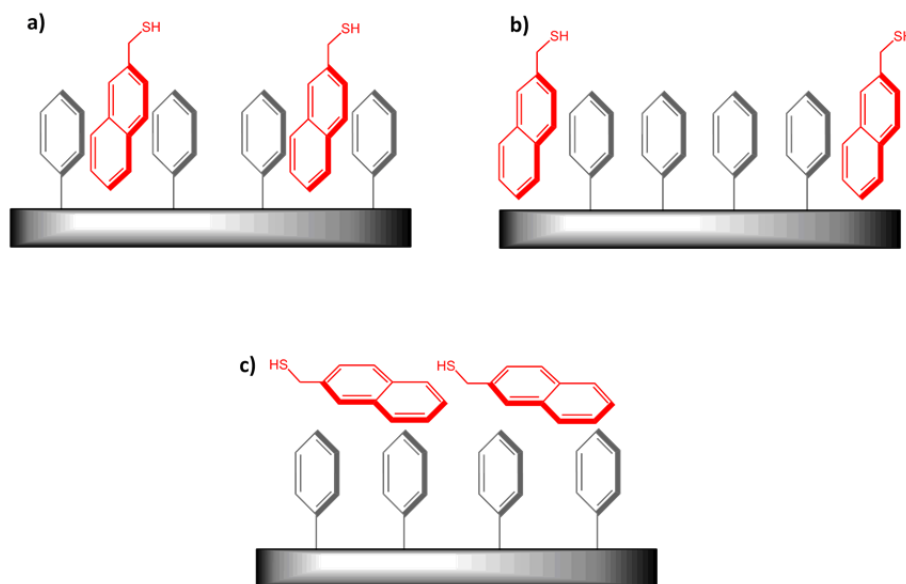
Figure 6. Proposed geometric arrangements of secondary surface molecules vs. phenyl scaffold molecules. a) interlocked "toaster" configuration, b) "border" configuration, and c) edge-face layered configuration.

closely-packed phenyl groups or an "edge-face layered" configuration in which the naphthyl rings interact with the phenyl groups in an edge-face manner primarily on the top of the islands of phenyl groups (Figure 6, c and a espectively).

The area of interaction between secondary surface and scaffold in the proposed "border configuration" is at a minimum in the highly functionalized and minimally functionalized Ph-SAMMS materials and should be at its maximum in the moderately functionalized Ph-SAMMS materials. In the "toaster" and "edge-face layered" configurations, the area of interaction should simply increase with phenyl density. Based on these observations about the interaction areas, our data suggests a configuration similar to the "border configuration" (Figure 6, b) since this is the only configuration in which the secondary surface – scaffold interaction would be at a maximim in Ph-SAMMS materials with moderate phenyl density. These observations only apply to material geometry preferred by these sublimation experiments in which the hydrophobic interactions which are likely very important in aqueous matrices have little contribution to material stability. The preferred geometry suggested by these experiments are not necessarily indicative of the preferred geometry of the surfaces which are present when the materials are exposed to aqueous matrices.

2.4. Comparative sorption performance of mesoporous materials

Sorbent performance can be characterized by the collection efficacy and the fundamental affinity of target materials. Generally a sorbent material's affinity for a target species described by the distribution coefficient (Kd) measurement:

$$K_d = \frac{C_o - C_f}{C_f} \times \frac{V}{M}$$

C_o is the initial concentration of the target analyte, C_f is the final equilibrium concentration, V is the volume (mL) of the testing solution, and M is the mass (g) of sorbent used. The distribution coefficient is the solid phase equivalent to liquid phase equilibrium constants and is a direct empirical measurement of a sorbents affinity (for the specified chemical in the specified matrix). Higher affinities are needed for trace level capture and K_d values of 10,000 are considered quite good, and K_d values exceeding 100,000 are considered excellent. When evaluating sorbent effectiveness in experiments in which C_f is very small, the values of C_f and percent target removal (Table 2) should be considered along with K_d since very small differences in C_f can create very large differences in the numerical value of K_d (Table 3) – making two comparable sorbents seem very different. The % removal provides a practical measurement of sorbents ability to remove material from solution, in this case trace level heavy metals from river water. Thiol-functionalized SAMMS materials presented in the report show near complete removal of the heavy metal ions (Table 2).

	Cd		Hg		Pb		Ag	
	Final Conc [ppb]	% Removal	Final Conc [ppb]	% Removal	Final Conc [ppb]	% Removal	Final Conc [ppb]	% Recovery
MCM-41	41	15	38	3	0.6	95	44	2
Ph-SAMMS 1.3	46	5	38	3	1.8	62	41	4
GT-74	17	62	19	57	30	66	11	84
SH-SAMMS	0.03	100	0.4	99	0.04	100	<0.01*	100
A-0.05 SH per g	1.2	97	1.3	97	0.9	92	<0.01*	100
B-0.26 SH per g	0.6	99	1.2	97	<0.04*	100	<0.01*	100
C-0.55 SH per g	0.9	98	1.4	97	0.2	99	<0.01*	100

Table 2. C_f and % target removal for selected materials. A, B, and C represent non-covalently functionalized SH-bearing materials having 0.05, 0.26, and 0.55 mmol thiols per g material, respectively. [*] C_f values were below the limit of quantification (LOQ) – the values reported are LOQ times the dilution factor. In all experiments L/S was 5000.

The affinity of thiol-functionalized materials for Hg(II), Cd(II), Ag(I) and Pb(II) is greater than that of MCM-41, Ph-SAMMS, and typical sorbent materials (Table 3). Further, the non-

covalently functionalized thiol-bearing materials for Hg(II), Cd(II), Ag(I) and Pb(II) in water is on par with that of their covalently functionalized counterpart, SH-SAMMS (Table 3).

At liquid:soild (L/S) ratios of about 5000, all MCM-41 based materials show higher K_d for Hg, Cd, Ag, and Pb than GT-74. Control experiments using unfunctionalized MCM-41 and Ph-SAMMS show that both have some innate affinity for Pb(II) species in water. All thiol-functionalized sorbents show increased affinity for Pb Hg, Cd, and Ag over MCM-41 and Ph-SAMMS and demonstrate quantitative removal of Pb and Ag and nearly quantitative removal Hg and Cd (Table 2). For all non-covalently functionalized sorbents reported as well as SH-SAMMS, concentrations of Pb, Hg, and Cd were reduced from 50 ppb to well below EPA's maximum contaminant levels for safe drinking water [40].

	Cd	Hg	Pb	Ag
MCM-41	830	130	93 000	130
Ph-SAMMS	270	900	22 000	470
GT-74	8 200	6 600	9 800	27 000
SH-SAMMS	8 300 000	480 000	220 000	>35 000 000
A - 0.05 SH per g	200 000	145 000	62 000	>31 000 000
B - 0.26 SH per g	490 000	180 000	>1 300 000	>31 000 000
C - 0.55 SH per g	270 000	141 000	370 000	>31 000 000

Table 3. K_d values for selected materials. > indicate that the following K_d values were calculated based on a C_f which was below the LOQ. In these cases, the values substituted for C_f were the LOQ times dilution factor. A, B, and C represent non-covalently functionalized SH-bearing materials having 0.05, 0.26, and 0.55 mmol thiol per g material, respectively.

3. Arene-Arene Interaction Motif on Iron Oxide Nanoparticles

We have also modified magnetic iron oxide (Fe_3O_4) nanoparticles (introduced in Chapter II, Section 3) to yield nanoparticles with a phenyl-coated surface. This phenyl-bearing surface is analogous to that of Ph-SAMMS and, similarly to Ph-SAMMS, the surface of these phenyl-bearing nanoparticles acts as a scaffold for a layer of aromatic molecules (Figure 7). As a support structure, Fe_3O_4 nanoparticles (NPs) are advantageous due to their high surface area, dispersibility, and susceptibility to magnetic fields. For application as a sorbent material, the NPs may be dispersed and incubated in a contaminated medium and then retrieved using a strong magnet - as opposed to requiring mechanical retrieval like SAMMS materials.

General preparation procedures for the materials presented in this chapter is given in Section 5. Briefly, Fe_3O_4 NPs are prepared with lauric acid ligand shells – lauric acid molecules are

attached through their carboxylate functionality. The lauric acid ligands are then exchanged for benzoic acid. As a result, the phenyl rings form the accessible surface of the benzoic acid Fe_3O_4 nanoparticles. This orientation of phenyl rings is analogous to that of the Ph-SAMMS surface. The benzoic acid Fe_3O_4 NPs are then incubated with aromatic thiols in an organic solution and slow evaporation of the solvent yields a non-covalently attached thiol-bearing surface. Like all SH-bearing materials discussed in this dissertation, SH-bearing Fe_3O_4 NPs are effective for capture of Cd(II), Hg(II), and Pb(II) from aqueous matrices and the non-covalent linkage in the surface layer enables the active surface to be removed, recycled and replaced.
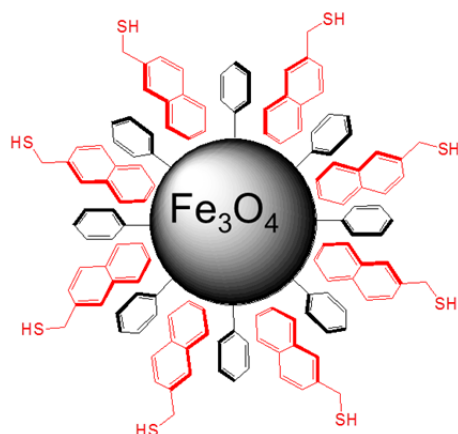
Figure 7. Illustration of a non-covalently functionalized Fe_3O_4 nanoparticle. The phenyl (black) ligand shell enables non-covalent attachment of the thiol-bearing layer (red). Illustration is shown with phenyl ligand shell and thiol-bearing layer in idealized orientation and is not to scale.

3.1. Characterization of Fe_3O_4 nanoparticles

Fe_3O_4 NPs were characterized using BET, TGA, as well by Scanning Transmission Elecron Microscopy (STEM) coupled with Energy-dispersive X-ray spectroscopy (EDX). The BET surface area was found to be ~110 m^2 per g while TGA indicated 0.8 mmol benzoic acid per g of material. These values are typical for the type and diameter (about 8 nm) of these NPs.[28] Unfortuntately, Fe_3O_4 materials are not compatabile with the Ellman's test for thiols. The presence of Fe_3O_4 yields a false positive so, although less precise, TGA was used to quantify the thiol-bearing secondary surface layer (Figure 7). TGA analysis indicated approximately 0.04 mmols of BMMB per g material, 0.05 mmols/g MN and 0.01 or less mmol per g BM. These values represent approximately the same secondary surface:phenyl scaffold ratio (roughly 1:15) as most of the Ph-SAMMS materials. This suggests that the interactions between the phenyl scaffold and secondary

surface involved in both materials are similar - the interactions responsible for the formation of the attachment of the secondary surface to Ph-SAMMs are similar to the interactions resonsible for the attachment of the secondary surface to benzoic acid Fe_3O_4 NPs.

The number of phenyls per gram material and the number of thiols per gram material are significantly higher for Ph-SAMMS materials than for Fe_3O_4 NPs. This discrepancy is expected given the higher relative suface area per unit mass of the SAMMS materials (between 800 and 400 m^2/g for Ph-SAMMS compared to about 100 m^2/g for ~60 Å Fe_3O_4 NPs.)
In an effort to confirm the presense of the secondary surface, we performed STEM-EDX eperiments which provide elemental analysis of the imaged sample (Figure 8). Energy-dispersive X-ray spectroscopy (EDX) does not indicate conclusively the presence of sulfur. Organic sulfur produces an EDX signal at about 2.2 keV. Such a signal is present (Figure 8, bottom left), however, the counts are too low (less than 4 for S compared to 60 for Fe) to allow a confident evaluation of the presence of sulfur. This is probably due to relatively low concentration of S compared that of Fe and O. Based on analysis of the TGA data, one would expect the sulfur content of the functionalized Fe_3O_4 NPs to account for less than 1% of the weight of the material. The amount of S relative to Fe, O, and even C, is so small in these materials that detecting it by EDX is not practical. In Section 3.2 we discuss the sorption performance of the functionalized Fe_3O_4 NPs. We observe that the addition of the thiol-bearing secondary surface produces a material with the sorption characteristics of typical thiol-bearing materials. So, despite our failure to directly measure the sulfur content of our functionalized Fe_3O_4 NPs, observations of their sorption characteristics along with TGA analysis seem sufficient to confirm that the Fe_3O_4 NPs are indeed thiol-bearing materials.
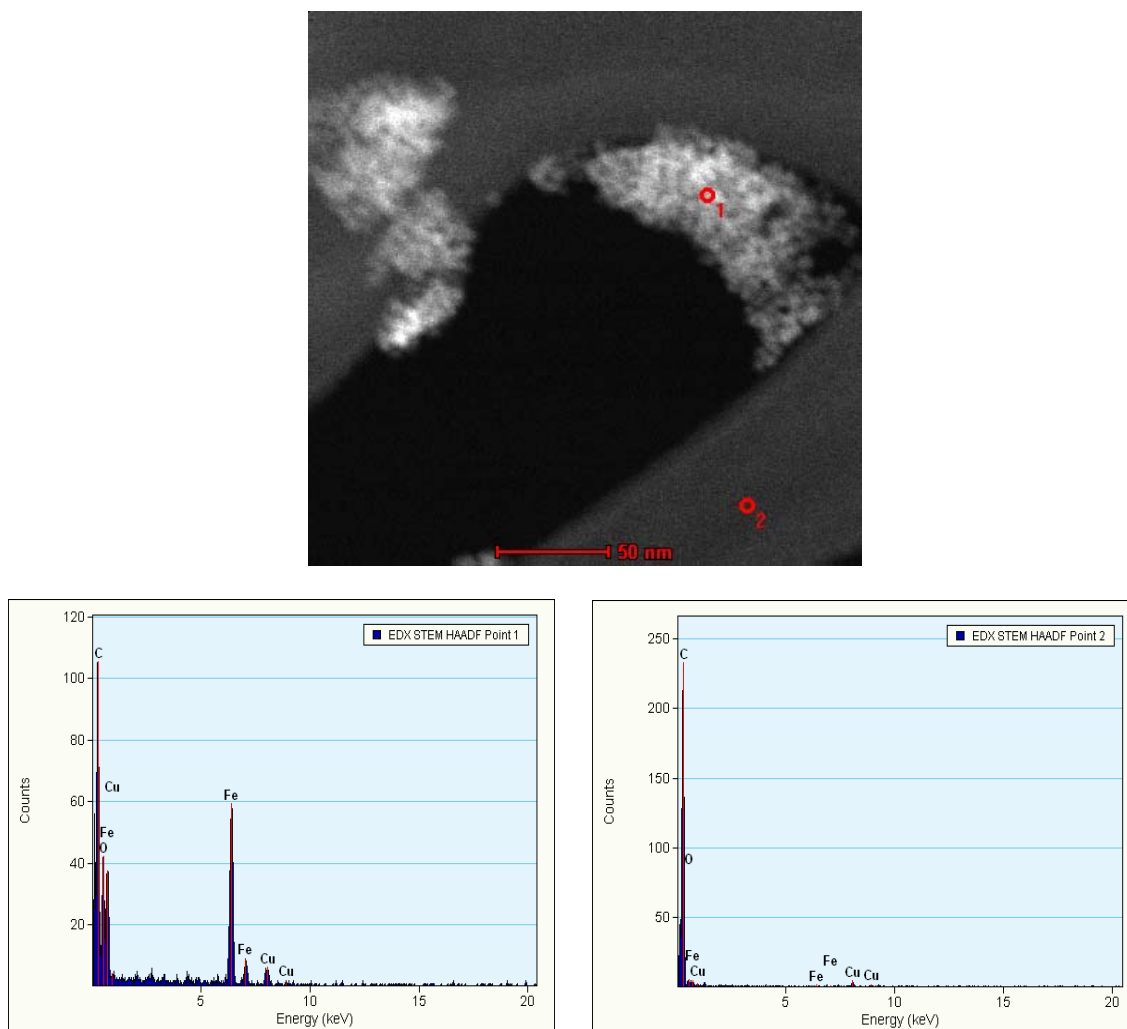
Figure 8. TEM image (top) and EDX analysis of functionalized Fe_3O_4 nanoparticles. EDX analysis does not indicate the presence of sulfur. The left chart indicates EDX counts in region one. As a control, the right chart indicates EDX counts of the TEM grid (lacey carbon).

3.2. Comparative sorption performance of Fe_3O_4 nanoparticles

As expected, addition of the thiol-bearing secondary surface yields a material with excellent sorption ability for Cd(II), Hg(II), and Pb(II). Table 4 shows the % removal and final concentration Cd(II), Hg(II), and Pb(II) by benzoic acid Fe_3O_4 NPs (as a control), as well as mercaptopropionaic acid (MPA) Fe_3O_4 (presented in reference 28) NPs which are covalently functionalized, thiol-bearing NPs. Table 5 shows the corresponding K_d values for the same materials and contaminants. Benzoic acid Fe_3O_4 NPs are capable of moderate adsorption of Cd(II) and Hg(II) and excellent adsorption of Pb(II). Presumably, the Pb affinity is due to the combination of exposed Fe_3O_4 surface and/or exposed carboxylate functionalities interacting with the famously oxophilic Pb(II)

53

ions.[42] Since the Fe_3O_4 NPs are capable of nearly complete removal of Pb(II), thiol

functionalization does not have any practical benefit for this substrate with respect to Pb(II)

removal. Regarding Cd(II) and Hg(II) removal, MPA Fe_3O_4 NPs appear to be marginally more

efficient than our non-covalently functionalized benzoic acid Fe_3O_4 NPs and much more efficient

than benzoic acid Fe_3O_4 NPs.

	Cd		Hg		Pb	
	Final Conc [ppb]	% Removal	Final Conc [ppb]	% Removal	Final Conc [ppb]	% Removal
Benzoic acid NP	12	76	22	28	0.04	99
MPA NP	3	95	0.4	99	<0.04*	99
BMMB+NP	6	88	2	94	<0.04*	99
MN+NP	5	90	2	92	0.06	98
BM+NP	7	86	0.7	97	0.07	98

Table 4. Percent removal and final concentration of Cd(II), Hg(II), and Pb(II) from Columbia River water by Fe_3O_4 NP materials.

	Cd	Hg	Pb
Benzoic acid NP	3 500	360	116 000
MPA NP	25 000	110 000	177 000
BMMB NP	12 000	13 000	211 000
MN NP	14 000	12 000	122 000
BM NP	10 000	58 000	191 000

Table 5. K_d values for removal of Cd(II), Hg(II), and Pb(II) by functionalized Fe_3O_4 NPs. MPA-functionalized NPs perform slightly better than their non-covalently functionalized counterparts, BMMB NP, MN NP, and BM NP.

4. Conclusions and Bridge to Chapter IV

In summary, a series of flexibly and reversibly functionalized sorbents have been prepared

and some have shown excellent stability and performance in water matrices. Three factors

affecting this stability were identified, the identity of the secondary surface components, density of

these components, and the density of the phenyl groups of Ph-SAMMS. The secondary surface

layer was found to be most stable when composed of molecules with limited water solubility and

when these molecules were supplied in sufficient density. A scaffold density of about 1.3 phenyl

molecules per nm^2 was found to be optimal for the overall water stability of the final material. The

same surface functionalization motif was applied to phenyl-bearing Fe_3O_4 NPs which yielded thiol-

bearing Fe_3O_4 NPs having a surface configuration analogous to that of the non-covalently

functionalized Ph-SAMMS materials. Both the functionalized SAMMS materials and the functionalized Fe_3O_4 NPs show excellent Cd(II), Hg(II), and Pb(II) sorption performance in a natural water matrix.

One drawback of a surface modification motif driving almost exclusively by the hydrophobicity of the Ph-SAMMS surface and secondary surface components is that the final overall material is so hydrophobic that it effectively repels water. This a critical disadvantage for a material designed to work in an aqueous matrix and, so far, has only been overcome by adding methanol or ethanol to the material in order to encourage wetting. Chapter IV describes the invention and investigation of yet another supramolecular surface modification motif which is based on associations between small organic secondary surface components and cyclodextrin groups. This motif was designed, among other reasons, in order of overcome the limited wettability of the Ph-SAMMS materials.

CHAPTER IV

SUPRAMOLECULAR MODIFICATION OF SURFACES VIA CYCLODEXTRIN-

ADAMANTANE AND CYCLODEXTRIN-ARENE HOST-GUEST ASSOCIATION

This chapter was coauthored by Darren W. Johnson and Kara M. Sherman from the Department of Chemistry and Materials Science Institute, University of Oregon and Anna S. Ivanova from the California Institute of Technology SURF program. Sean Fontenot prepared the chapter, designed experiments for all materials presented in this chapter, prepared and analyzed cyclodextrin and adamantane materials, and performed literature research and analysis. Kara Sherman designed and performed the preparation of adamantane-based materials, performed analysis of adamantane and cyclodextrin materials, and provided editorial assistance. Anna Ivanova prepared and performed analysis of cyclodextrin materials. Darren Johnson and Sean Fontenot were responsible for development of this project. This unfinished work will be completed by Kara Sherman.

1. Introduction

The Ph-SAMMS materials presented in Chapter III exploit the differential hydrophobicity/hydrophilicity between the Ph-SAMMS surface and an aqueous environment in order to create a metastable secondary surface layer. A major drawback of these new materials for application in aqueous matrices is that the highly hydrophobic materials have kinetically limited accessibility to water. As stated in Chapter III, to achieve favorable sorption kinetics in aqueous matrices, Ph-SAMMS materials must be pre-treated with methanol or ethanol prior to application as sorbents. Realizing that this severely limits the potential application of Ph-SAMMS materials, we sought to develop a supramolecular modification motif which would still yield an easily wettable surface. We accomplished this by modifying a silica surface with β-cyclodextrin and utilizing 2-

mercaptomethyl naphthalene (MN) and 1-adamantanethiol to form the secondary surface (Figure 1). We have also produced an "upside down" analogue of this material in which adamantane-functionalized mesoporous silica (Ad-SAMMS) supports a secondary surface layer of β-cyclodextrin. This preliminary work is encouraging and in future investigations, modified cyclodextrins may be used in order to create a functional secondary surface similar to those discussed in Chapter III.
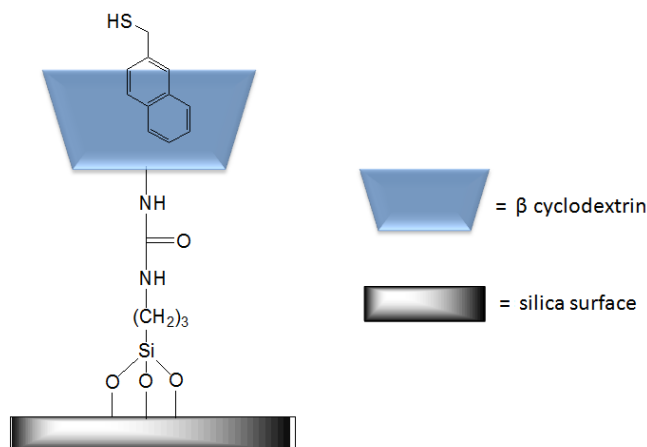
Figure 1. Illustration of β-CD-SAMMS surface with 2-mercaptomethylnaphthalene (MN) shown as a guest.

2. β-Cyclodextrin-Functionalized Mesoporous Silica

We developed β-cyclodextrin-functionalized mesoporous silica (β-CD-SAMMS) to act as a scaffold material similar to Ph-SAMMS. β-cyclodextrin is a cyclical molecule composed of seven glucose monomers attached *via* alpha-1,4 glycosidic bonds. β-cyclodextrin molecules are toroidal in shape with hydroxyl groups bordering the openings of a central cavity (Figure 2). One face of the toroid, dubbed the "primary face," bears seven primary hydroxyl groups, one for each glucose monomer. The "secondary face" bears fourteen secondary hydroxyl groups, two for each glucose monomer. The exterior hydroxyl groups make β-cyclodextrin fairly hydrophilic (it is moderately water soluble). However, the interior of β-cyclodextrin is comparatively hydrophobic. This dichotomy between exterior and interior environments drives the formation of host-guest complexes when hydrophobic species are present along with β-cyclodextrin in an aqueous environment; β-cyclodextrin molecules "host" hydrophobic species which can fit inside the β-cyclodextrin cavity.   In this fashion, β-cyclodextrin molecules are capable of binding many small

organic molecules such as adamantane and naphthalene.[1-4] We took advantage of these host-guest relationships in order to prepare materials in which surface cyclodextrin groups host functional molecules and (Figure 1). By doing so we are able to produce a material without any covalent bonds between functional surface and the material support. In addition, the hydroxyl groups of the β-cyclodextrin molecules provide the material surface with sufficient overall hydrophilicity to preserve the wettability of the material.
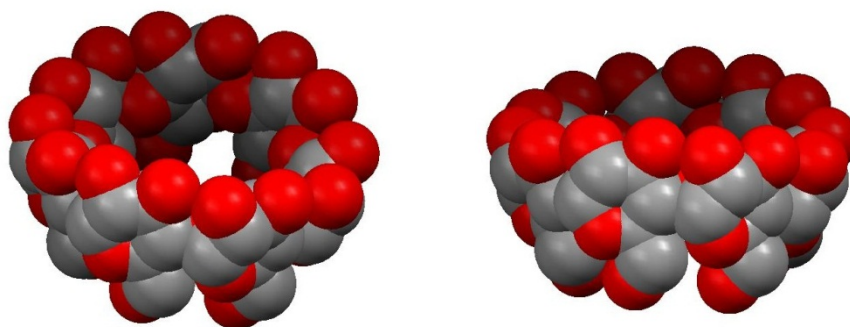
Figure 2. β-cyclodextrin illustrations. The left illustration shows the fourteen hydroxyl oxygens (red) of the secondary face and the comparatively hydrophobic cavity. The right illustration is a better representation of the asymmetrical toroid shape of the molecule. Hydrogens have been omitted for clarity. The diameter of β-cyclodextrin (measured as the distance between the carbon atoms farthest apart plus the one carbon van der Waals radius) is approximately 1.4 nm. This corresponds to a circular footprint of about 1.5 nm^2 and a square footprint of about 2 nm^2.

β-CD-SAMMS was prepared by sequential modification of propylamine-functionalized mesoporous silica (Amino-SAMMS).[5] This surface preparation strategy was introduced in Chapter I, Section 3. Amino-SAMMS itself was prepared using Davisil®, a commercially available mesoporous silica with pore sizes of approximately 160 Å. While MCM-41, having pore sizes of 35 Å was suitable for preparing Ph-SAMMS, Davisil® was used in lieu of MCM-41 because the larger pore size of Davisil is able to accommodate the comparatively "thicker" cyclodextrin surface without suffering a critical reduction in pore size which would lead to severe restriction in mass transport through the pores of β-CD-SAMMS. The effects of geometric restraints on surface functionalization are discussed in Chapter I, Section 3.

β-CD-SAMMS preparation is outlined in Figure 3. A reactive β-cyclodextrin species, mono-6-deoxy-6-azido-β-cyclodextrin (β-CD-N$_3$), was prepared by tosylation of one of the six secondary hydroxyl groups.[6] Tosylation of β-cyclodextrin was followed by conversion of the tosyl

group to an azide (*via* azidolysis) to yield β-CD-N$_3$. A Staudinger-type reaction was then used to attach β-CD-N$_3$ to Amino-SAMMS.[7]
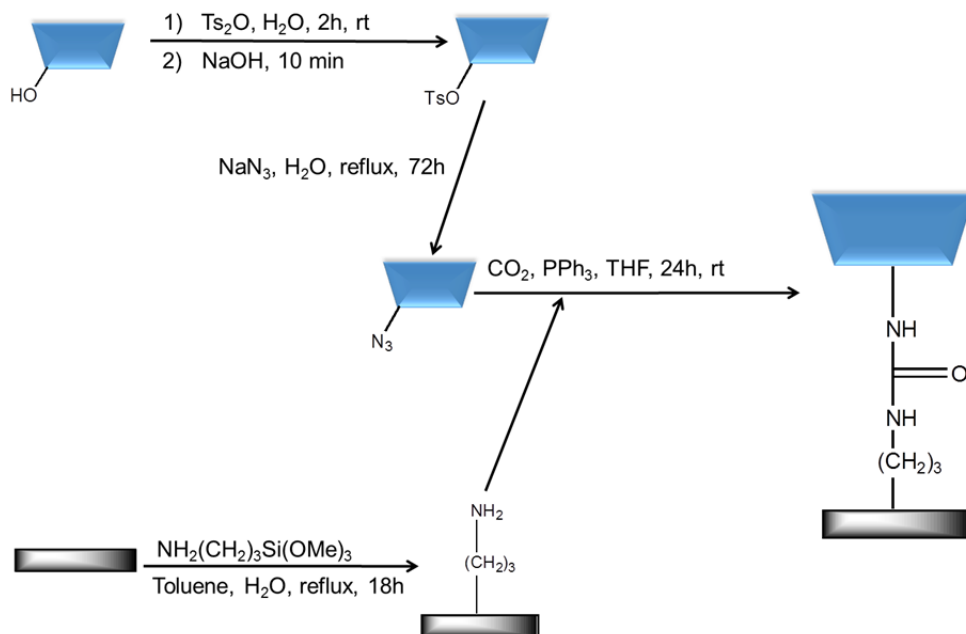
Figure 3. Preparation of β-CD-SAMMS

β-CD-SAMMS and Amino-SAMMS were characterized by thermal gravimetric analysis (TGA). Table 1 shows the results of preparing β-CD-SAMMS using Amino-SAMMS substrates of 0.25, 0.5, and 1.1 amines/nm^2. To ensure that there was sufficient β-CD available for reaction with surface mines, attachment of β-CD was attempted with β-CD-N$_3$ supplied in approximately stoichiometric amounts (i.e. 1:1 with surface amines) as well as in four-fold excess. Because the footprint of β-CD significantly larger than that that of silylpropylamine, we expected that the extent of amine functionalization would be limited such that some surface amines would be "wasted" simply because β-CD groups would obscure nearby amines. Nevertheless we attempted to produce the most uniform material possible. In materials in which there are a multitude of functionalities present, it becomes more difficult to identify the effects of subsequent functionalization. Material uniformity simplifies analysis of these materials.

In all β-CD-SAMMS materials produced, less than 20% of the amines were functionalized (β-CD-N$_3$ was only successfully reacted with 20% or less of the available surface amines). The presence excess of β-CD-N$_3$ does not affect the extent of functionalization; in all cases the small

differences between β-CD-SAMMS produced with 1 and 4 equivalents are within the error of our measurements. We also observed that extending the reaction time beyond 24 h had no effect on the final material composition. Since neither reaction duration nor addition of excess β-CD-N$_3$ had a noticeable impact on the extent of functionalization, we can reasonably conclude that, as we expected, geometric restraints are responsible for the limited functionalization of the surface amines.   The minimum footprint of a β-cyclodextrin molecule can be estimated to be about 1.5 nm^2 (Figure 1). This corresponds to a maximum β-CD density of 0.67 CD/nm^2, assuming a flat surface completely covered with functionally available amines. Surface curvature as well as amine distribution will significantly reduce the actual maximum β-CD density. It is also likely that the amines on Amino-SAMMS are distributed such that they are more dense near the pore windows.[8] However, such surface modeling is beyond the scope of this investigation. It is sufficient that we observe that the most uniform material was produced using Amino-SAMMS with 0.5 amines/nm^2.

Amines per nm^2	CD/Amine Equivalents	% Amines functionalized	CD per nm^2
0.25	1	6	0.01
0.25	4	8	0.02
0.5	1	18	0.09
0.5	4	19	0.1
1.1	1	5	0.06
1.1	4	7	0.08

Table 1. Amino-SAMMS and β-CD-SAMMS coverage. The most uniform materials were produced using an Amino-SAMMS support with 0.5 amines/nm^2. Since adding excess β-CD-N$_3$ does not result in more β-CD groups attached to the surface, we conclude that the extent of β-CD functionalization is limited by the size of the β-CD groups and the interior pore geometry.

2.1. β-CD-SAMMS with MN as a secondary surface component

We successfully attached 1-mercaptomethylnaphthalene (MN) to β-CD-SAMMS by dissolving MN in CHCl$_3$, suspending β-CD-SAMMS in the solution, evaporating to dryness, and washing to remove unbound or precipitated MN. MN was chosen as a secondary surface component to allow direct comparison between Ph-SAMMS (introduced in Chapter III) and β-CD-SAMMS and because β-CD and naphthalene derivatives are capable of forming in a 1:1 host-guest complex.[9,10] As we did with the Ph-SAMMS materials, we prepared MN-functionalized β-CD-SAMMS materials with different amounts of MN, ranging from 1.4 equivalents of MN (1.4 MN per

β-CD) to 0.2. We examined the robustness of the MN-β-CD-SAMMS secondary surface, formed

by adsorption of MN onto β-CD-SAMMS using the Ellman's test for thiols.[11]   The results of these

tests, summarized in Table 2, show that MN-β-CD-SAMMS surfaces are significantly less robust

than those of the best MN-Ph-SAMMS materials (which lost less than 2% of the secondary surface

under the same conditions).

CD per nm^2	MN/CD ratio	MN per nm^2	% SH desorbed (leached into aqua)
0.0	-	0.05	84
0.1	1.4	0.14	74
0.1	0.9	0.01	13
0.1	0.4	0.04	14
0.1	0.2	0.02	8

Table 2. MN-β-CD-SAMMS surface analysis. 0.0 CD per mn^2 represents Amino-SAMMS which
was used as a control to account for the innate affinity of Amino-SAMMS for MN. The conclusions
reached by these experiments are severely limited since approximately 16% of the MN secondary
surface was retained by Amino-SAMMS.

It should be noted that, while secondary surfaces of MN-β-CD-SAMMS materials are more

robust than the MN secondary surfaces prepared as a control on Amino-SAMMS, Amino-SAMMS

does retain a small amount of MN (shown in Table 2 as first entry and confirmed by TGA). Thus,

we are unable to conclude that the secondary surfaces of β-CD-SAMMS materials are forming

exclusively (or at all!) *via* MN-β-CD interactions. Since there are a comparatively large number of

amines present even in our most uniform β-CD-SAMMS materials, we should expect some MN to

adsorb directly onto the amine portions of the material. This would explain why the material

produced with 1.4 MN molecules per β-CD is significantly less robust than those prepared with a

MN/CD of 1 or less – the MN/amine interaction should be much less favorable (in water) than the

MN/CD interaction. Yet, this remains an assumption since we cannot distinguish between

interactions between MN and amine surfaces vs. interactions with β-CD surface. This limitation

prevents us from determining whether or not the host-guest association of β-CD and MN is

sufficiently robust in water to produce an acceptably persistent secondary surface. This same

limitation applies to the adamantane/CD surfaces discussed in the following sections of this

chapter.

In terms of wettability, the advantages of β-CD-SAMMS over Ph-SAMMS were

immediately apparent (Figure 4). Ph-SAMMS materials require pre-treatment with methanol or

ethanol in order to facilitate wetting and suspension in water. β-CD-SAMMS, like Amino-SAMMS and Davisil® wet immediately.
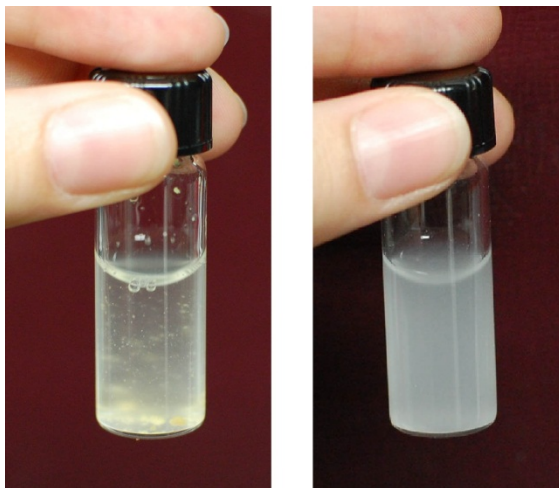
Figure 4. Wettability of Ph-SAMMS (left) compared to β-SAMMS (right). Both materials were prepared using 160 Å Davisil® as the substrate and both materials have been functionalized with MN as a secondary surface component.

2.2. β-CD-SAMMS with adamantanethiol as a secondary surface component

Encouraged by the moderate robustness of the MN-β-CD-SAMMS surface and its favorable wettability, we searched for another secondary surface molecule. Adamantane is an ideal β-cyclodextrin guest and the β-cyclodextrin/adamantane association has been exploited to prepare several classes of polymeric materials.[12,13] The β-cyclodextrin/adamantane association constant has been measured to be 5.2×10^4 M^{-1} in water.[1] While the association constant for MN and β-cyclodextrin and is not known, association constants for 2-hydroxynaphthalene (2-naphthol) was measured to be about 600 M^{-1}, nearly two orders of magnitude smaller than that of the β-cyclodextrin and adamantane.[9] Based on the similarities between MN and 2-naphthol, the β-cyclodextrin/MN association constant may be reasonably assumed to be comparable to that of β-cyclodextrin/2-naphthol (in water). Our evaluation of adamantanethiol-β-CD-SAMMS indicates reduced leaching compared to MN-β-CD-SAMMS (Table 3). So, the greater association constant of the β-cyclodextrin/adamantane system seems to translate into a comparatively more robust secondary surface.

Table 3 summarizes the results of stability testing of Adamantanethiol-β-CD-SAMMS in water. Surfaces prepared with smaller adamantanethiol/CD ratios appear to be more robust. This trend is consistent with our observations of MN-β-CD-SAMMS although the overall robustness of adamantanethiol-β-CD-SAMMS is superior. As we expected, adamantanethiol-β-CD-SAMMS possesses wetting characteristics similar to MN-β-CD-SAMMS.   Since Amino-SAMMS has some affinity for adamantanethiol (as it does for MN), we are unable to determine how much of the adamantanethiol desorption (leaching) is may be attributed to desorption from amine surfaces vs. from the CD groups. We cannot definitively determine whether or not the adamantanethiol/CD interaction in these materials is persistent in water.

CD per nm^2	Adamantanethiol/ CD ratio	Adamantanethiol per nm^2	% SH desorbed (leached into aqua)
0.0	-	0.04	86
0.1	0.95	0.09	18
0.1	0.4	0.04	7
0.1	0.18	0.02	3
0.1	0.19	0.02	2

Table 3. 1-adamantanethiol-β-CD-SAMMS surface analysis. 0.0 CD per mn^2 represents Amino-SAMMS which was used as a control to account for the innate affinity of Amino-SAMMS for 1-adamantanethiol.

3. Ad-SAMMS Materials

Observing that this Adamantane/β-cyclodextrin system was useful for forming wettable-yet-moderately-water-stable surfaces, we prepared Adamantane-functionalized Mesoporous Silica (Ad-SAMMS) which preliminary investigations have shown is capable of supporting a secondary surface of β-cyclodextrin molecules. Used in conjunction with functionalized β-cyclodextrin molecules it will be possible to attach specific functionality to an adamantane surface in exactly the same manner as the adamantanethiol-β-CD-SAMMS example.

Ad-SAMMS was prepared by attaching adamantanecarbonyl groups to Amino-SAMMS (Figure 5). TGA indicates an adamantane density of 0.16 per nm^2 for the resultant Ad-SAMMS material. This corresponds to functionalization of 66% of surface amine groups. This degree of
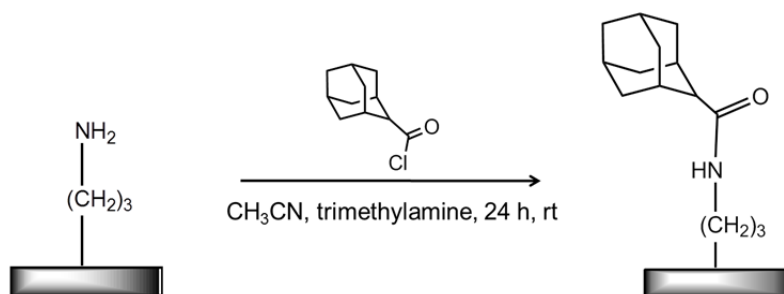
Figure 5. Preparation of Ad-SAMMS. Amino-SAMMS is stirred with trimethylamine and 1-adamantanecarbonyl chloride in acetonitrile.

functionalization is unsurprising given the geometric restrictions of the pores. Preliminary experiments indicate that Ad-SAMMS will absorb β-cyclodextrin from water, yielding a surface with β-CD to potentially occupying 60% of adamantyl groups. This corresponds to approximately 0.1 β-CD per nm^2. Interestingly, this β-CD density is equivalent to the most densely-functionalized β-CD-SAMMS we were able to produce (also 0.1 β-CD per nm^2) which supports out earlier assertion that geometric restrictions are the primary factor in determining the maximum β-CD density of β-CD-SAMMS as well as in determining the maximum capacity of Ad-SAMMS for β-cyclodextrin. It should be noted that these calculations are based on mass difference alone (measured by TGA). Thus, we are unable to determine to what extent the β-CD secondary surface is interacting with the surface adamantyl groups of As-SAMMS or the unfunctionalized surface amines.

4. Summary and Bridge to Chapter V

We designed and prepared new supramolecular materials based on host-guest interactions between adamantane, naphthalene, and β-cyclodextrin. In doing so we accomplished our objective of creating wettable supramolecular materials. Materials presented in this chapter were characterized by TGA and the Ellman's test for thiols and were found to be moderately persistent in water. Our observations that 1-adamantanethiol surfaces are more stable on β-CD-SAMMS than MN surfaces is consistent with the known association constants for adamantane-β-CD and naphthyl-β-CD, respectively. This suggests that the reactions between secondary surface molecules (adamantanethiol and MN) and β-CD are indeed responsible for the formation of the assembly of β-CD-SAMMS materials. Unfortunately, we are prevented from claiming this definitively since we

were unable to prepare completely uniform materials (our β-CD-SAMMS were "mixed surface" materials having substantial amounts of amine surface present as well as silane surface).

We observed that for both β-CD-SAMMS and Ad-SAMMS materials, the maximum achievable β-CD density was approximately 0.1 β-CD/nm^2. This confirms our assertions regarding geometric restrictions as the primary factors in determining the maximum β-CD density of β-CD-SAMMS as well as in determining the maximum capacity of Ad-SAMMS for β-cyclodextrin.

One of the unifying themes of this dissertation has been identification of interactions that drive supramolecular association between molecules. In Chapters III and IV, these interactions have been identified and their effects on surface structure and stability of supramolecular materials have been measured. Chapter V describes related work in which supramolecular interactions give rise to the solid state geometry (helicity, in this case) of supramolecular assemblies. While Chapter V departs from the theme of surface modification, the small assemblies presented therein were accessible by a host of techniques, X-ray crystallography most importantly, which were not applicable to the materials discussed in the previous chapters. This was an advantage of sorts and the investigations in Chapter V were very successful in terms of identifying specific interactions having the largest impact on the conformations of the supramolecular assemblies presented.

CHAPTER V

DESIGN, SYNTHESIS AND CHARACTERIZATION OF SELF-ASSEMBLED

As$_2$L$_3$ AND Sb$_2$L$_3$ CRYPTANDS

This chapter was co-authored by Virginia M. Cangelosi, Melanie A. Pitt, Aaron C. Sather, Lev N. Zakharov, Orion B. Berryman, and Darren W. Johnson. Virginia Cangelosi prepared and developed the methods of preparation of most of the compounds in this study and was responsible for analysis of the formation of all compounds presented. Melanie Pitt and Aaron Sather each prepared one of the structures presented herein. All crystal structures were solved by Lev Zakharov except for the structure of As$_2$5$_3$ which was solved by Orion Berryman. Lev Zakharov also assisted in compilation of geometric data and assisted in analysis thereof. Darren Johnson is responsible for development of this project and provided editorial assistance. Sean Fontenot prepared the chapter, performed literature searches, prepared the As$_2$7$_3$ compound, conducted geometric calculations, and performed the analysis of mechanical coupling phenomena. The contents of this chapter were published as a report of the same name in *Dalton Transactions*, 2011, **40**, 12125.

1. Introduction

Fabrication of complex structures from simple components has been a research topic of great interest in recent years.[1] Supramolecular self-assembly processes and dynamic covalent chemistry offer a powerful set of tools for the bottom-up synthesis of complex structures with new properties and emergent functionality.[2,3] A defining feature of these synthetic strategies is that information contained within relatively simple components determines the formation of much more complex structures. Chemists have compiled an enormous library of self-assembled supramolecular complexes utilizing the directing properties of the transition metals. In

comparison, there are relatively few examples of assemblies that were designed to use the main group elements as directing components, showing that main group supramolecular chemistry is still developing the tools for the predictable formation of well-defined structures.[4] The main group elements generally prefer unusual "coordination" geometries compared to the transition metals, making them attractive targets when seeking novel properties, new topologies and alternative functionalities in self-assembled molecules and materials. However, there exists perhaps a misconception that bonds to main group elements are not labile enough for self-assembly.[5] Contradictory to this belief, our lab has shown that thiolate bonds to the Group 15 elements phosphorus, arsenic, antimony and bismuth are sufficiently reversible and can be used to drive the formation of supramolecular assemblies.[6-8]

This report provides full synthetic details and characterization of new As_2L_3 and Sb_2L_3 cryptands (Table 1). This structural report will discuss in detail how small changes to the ligand can greatly affect the helicity of the assemblies and the stereochemistry of the pnictogen ions. Additionally, a new route that facilitates the supramolecular syntheses is described, in which brief exposure of the reaction mixture to vacuum is sufficient to complete the self-assembly of the cryptands from an equilibrating mixture of lower order structures.

2. Cryptands Overview

Our lab has previously shown that E_2L_3 (E = As, Sb) cryptands form in self-assembly reactions between ECl_3, base, and rigid dithiol ligands H_21, H_22, or H_23 (Scheme 1, Scheme 2).[9-10] Characterization of these dynamic assemblies in solution and in the solid state revealed several structural similarities despite the differences in the rigid spacers between the mercaptomethyl groups of the ligands (ligand backbones). Consistently, each complex features short $E{\cdots}\pi$ distances, a consequence of the favorable pnictogen-π interactions, typically described as donation of electron density from the π-system of the ligands into the σ^* orbitals of the E atoms.[11] The different backbones of ligands H_21, H_22, or H_23 cause subtle variations in the angles and distances between the pnictogen atoms and phenyl rings (Table 2). In order to further explore this interaction, a series of E_2L_3 cryptands were assembled using dithiol ligands with newly designed backbones (H_24 – H_28, Scheme 2). Within each ligand, the mercaptomethyl arms were preserved but the size and rigidity of the backbone spacer was varied.
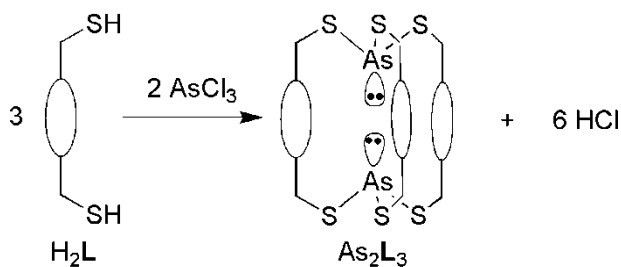
Scheme 1. Self-assembly of As$_2$L$_3$ cryptands.
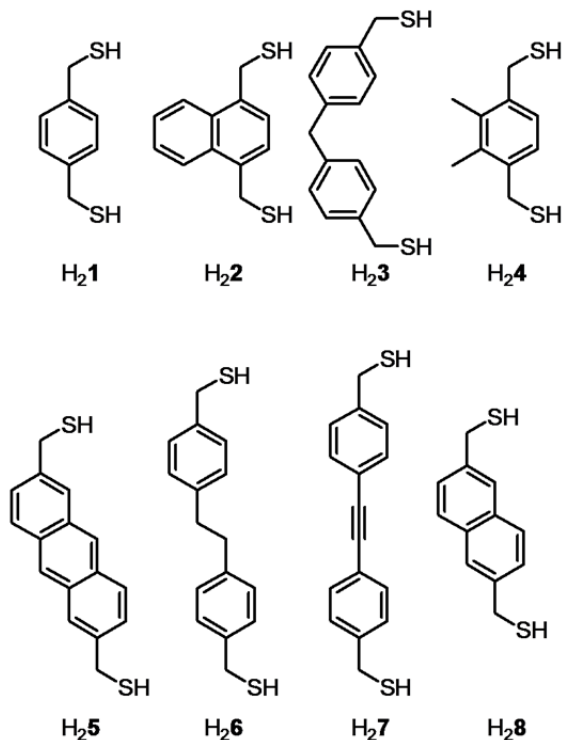
Scheme 2. Ligands used in synthesis of cryptands.

3. Synthesis of Cryptands

As$_2$L$_3$ (L = **1–8**) and Sb$_2$L$_3$ (L = **1, 2, 8**) cryptands were prepared in self-assembly reactions from ECl$_3$ and dithiolate ligands. The conditions previously reported for the synthesis of cryptands As$_2$**1**$_3$ (Figure 1a), Sb$_2$**1**$_3$ (Figure 1b), Sb$_2$**2**$_3$ (Figure 1c), and As$_2$**3**$_3$ (Figure 1e), involving deprotonation of H$_2$**L** with base followed by the addition of ECl$_3$ (E = As, Sb), also allowed for the preparation of cryptands As$_2$**4**$_3$ (Figure 2), As$_2$**2**$_3$ (Figure 1d), As$_2$**5**$_3$ (Figure 3), and As$_2$**6**$_3$ (Figure 4).[6,9,10,12] Crystals were grown of each assembly, allowing the direct comparison of these structures by single crystal X-ray diffraction.

Interestingly, base was not necessary for the synthesis of $As_2\mathbf{7}_3$ (Figure 5) which assembled under conditions which normally result in $As_2\mathbf{L}_2Cl_2$ macrocycle. Furthermore, $As_2\mathbf{8}_3$ would not assemble even with base present. These two surprising results prompted us to consider the role of base in this reaction. Was deprotonation of the ligand with base prior to reaction with arsenic necessary or was the role of the base simply to remove the HCl byproduct of As-S bond formation from the reaction? We previously established that when a 1:1 ratio of dithiol ligand and $AsCl_3$ are combined in the absence of base, two thiol functional groups substitute onto each $AsCl_3$ molecule, resulting in the formation of $As_2\mathbf{L}_2Cl_2$ macrocycles.[13] These results show that base is not necessary for the addition of these first two ligands. However, even if this reaction is carried out in the presence of excess ligand, substitution of a third thiol ligand onto As does not occur before $As_2\mathbf{L}_2Cl_2$ precipitates from solution after several days (except in the case of $As_2\mathbf{7}_3$). Each substitution of thiolate onto $AsCl_3$ results in the formation of an equivalent of HCl and one theory to explain our observations is that equilibrium with HCl causes the reaction to stop after two substitutions have been made at each arsenic center. In order to test this hypothesis, a chloroform solution of $H_2\mathbf{1}$ and $2/3$ $AsCl_3$ was heated and exposed to high vacuum at intervals over the course of the reaction (under continuous vacuum all solvent would have evaporated). Under these conditions $As_2\mathbf{1}_3$ formed, suggesting that the presence of the HCl byproduct is what limits the addition of ligands onto arsenic. Further support for this theory lies in our previous report that heating a mixture of dissolved $As_2\mathbf{L}_2Cl_2$ crystals with excess $H_2\mathbf{L}$ allows for the formation $As_2\mathbf{L}_3$.[13a] Because we started from crystalline $As_2\mathbf{L}_2Cl_2$ in that case, only two equivalents of HCl were formed while making $As_2\mathbf{L}_3$, instead of the six equivalents formed when cryptand was prepared directly from $AsCl_3$ and $H_2\mathbf{L}$.

The removal of HCl by vacuum allows for cryptand formation while avoiding the use of potentially harsh and complicating bases. To test the scope of this new vacuum-enabled synthetic technique, $H_2\mathbf{8}$ was mixed with $AsCl_3$ in chloroform at 50 °C and the reaction vessel was exposed to high vacuum for a few seconds every 1.5 hours. Within a few hours ^{1}H NMR spectroscopy revealed no free $H_2\mathbf{8}$ and that $As_2\mathbf{4}_2Cl_2$ and a new highly symmetric species were both present in solution. After one more day of heating, the new high-symmetry species was the dominant product. Crystals were grown by layering this chloroform solution with hexanes and the structure revealed that the main product of the reaction was the $As_2\mathbf{8}_3$ cryptand (Figure 6a-b). Similarly, $Sb_2\mathbf{8}_3$ was prepared using vacuum-enabled synthesis (Figure 6c-f). Both $As_2\mathbf{8}_3$ and $Sb_2\mathbf{8}_3$ could not be
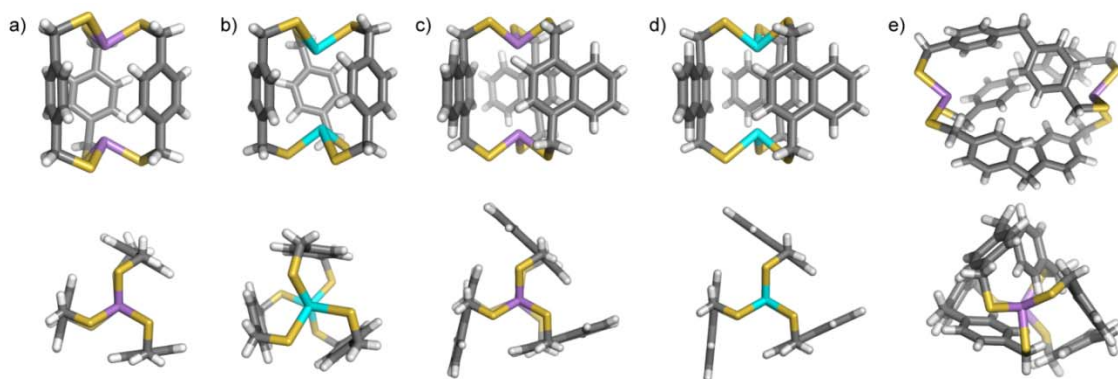
Figure 1. Stick representations of the X-ray crystal structures of previously reported E_2L_3 cryptands: (a) $As_2\mathbf{1}_3$,[9] (b) $Sb_2\mathbf{1}_3$,[12] (c) $As_2\mathbf{2}_3$,[6] (d) $Sb_2\mathbf{2}_3$,[6] and (e) $As_2\mathbf{3}_3$.[10] Arsenic is shown in purple, antimony in teal, sulfur in yellow, carbon in black and hydrogen in white.
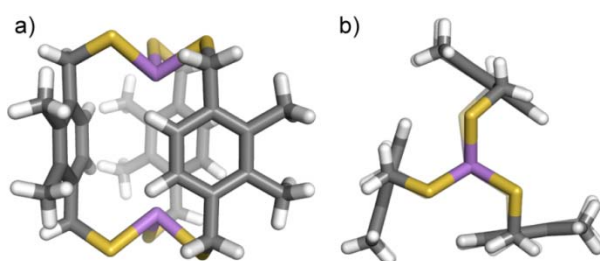
Figure 2. Stick representations of the X-ray crystal structures of the $As_2\mathbf{4}_3$ cryptand: (a) side-view showing the ligand domain and (b) top-view down the As-As axis showing one of the As(III) coordination domains.
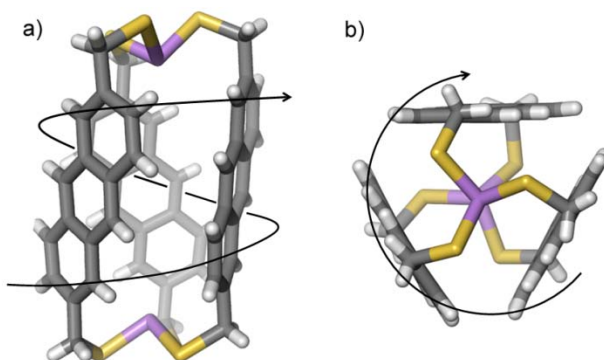
Figure 3. Stick representations of the X-ray crystal structures of $\varDelta,\varDelta,P$ isomer of the $As_2\mathbf{5}_3$ cryptand: (a) side-view showing the P configuration in the ligand domain and (b) top-view showing Δ configuration of one of the As(III) coordination domains.
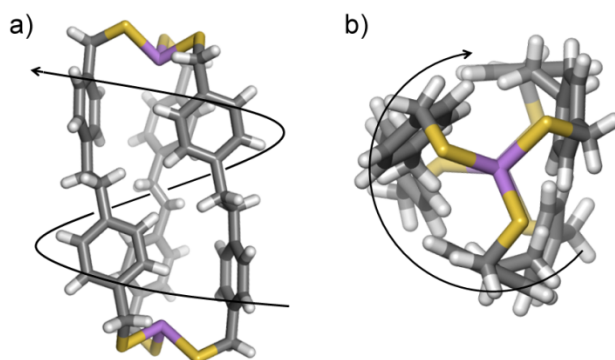
Figure 4. Stick representations of the X-ray crystal structures of the *Δ,Δ,M* isomer of the As$_2$**6**$_3$ cryptand: (a) side-view showing the *M* configuration in the ligand domain and (b) top-view showing Δ configuration of one of the As(III) coordination domains
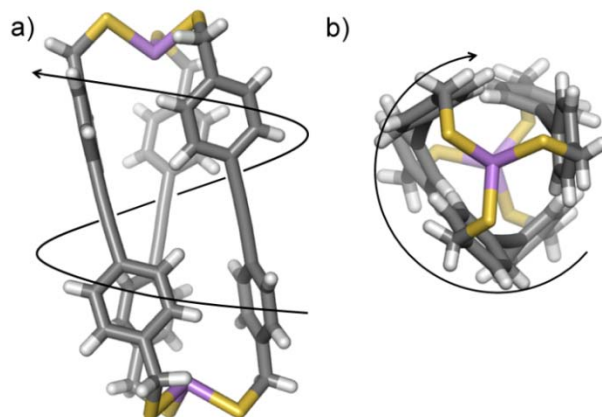
Figure 5. Stick representations of the X-ray crystal structures of the *Δ,Δ,M* isomer of the As$_2$**7**$_3$ cryptand: (a) side-view showing the *M* configuration in the ligand domain and (b) top-view showing Δ configuration of one of the As(III) coordination domains

prepared by other routes, suggesting that this relatively gentle synthetic route may allow for the preparation of new, larger-order assemblies. Additionally, this further supports that As$_2$L$_2$Cl$_2$ macrocycles are intermediates in cryptand formation.[7,8]
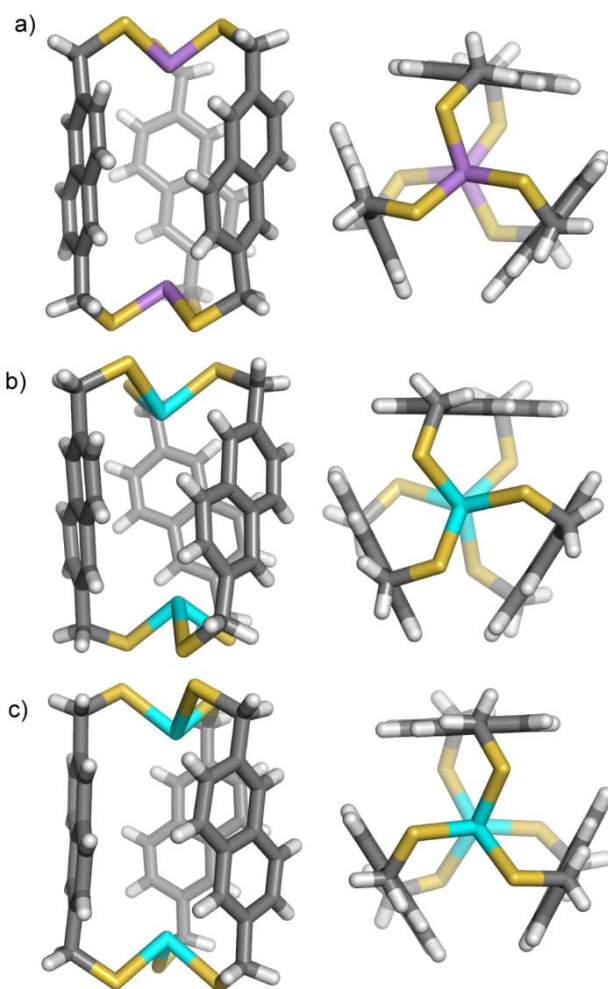
Figure 6. Stick representations of the X-ray crystal structures of the $E_2\mathbf{8}_3$ cryptands: (a) $As_2\mathbf{8}_3$, (b) $Sb_2\mathbf{8}_3(1)$, and (c) $Sb_2\mathbf{8}_3(2)$. (b) and (c) are isomeric forms of $Sb_2\mathbf{8}_3$ which cocrystallize.

4. Discussion of Cryptand Geometry

Single crystals of each cryptand were grown and the structures were obtained using X-ray diffraction (Figures 1-6). Comparison reveals several structural features that are general for this class of E_2L_3 cryptand. In each case, the $E\cdots\pi$ interaction causes the arsenic or antimony atoms to be positioned within the cryptand cavities. Consequently, their lone pairs of electrons point toward one another making the cavities uniquely Lewis basic. As expected, the distance between the pnictogen centers in each complex depends on the distance between the thiolate functionalities on the ligands (Table 2). In the arsenic structures, $As\cdots As$ distances range from 5.03 Å for $As_2\mathbf{1}_3$, the shortest cryptand, to 12.28 Å for $As_2\mathbf{7}_3$, the longest cryptand (Table 2). While this result is not surprising for the rigid cryptands, ($As_2\mathbf{1}_3$, $As_2\mathbf{2}_3$, $As_2\mathbf{4}_3$, $As_2\mathbf{5}_3$, $As_2\mathbf{7}_3$, and $As_2\mathbf{8}_3$) some flexibility is expected for $As_2\mathbf{3}_3$ and $As_2\mathbf{6}_3$. Indeed, $As_2\mathbf{3}_3$ exhibits this flexibility as the ligands are folded into

72

the cavity, destroying the C_3 symmetry of the complex and giving a shorter than expected As···As distance of 9.19 Å. All other cryptands have apparent C_3 symmetry. Despite the inherent ligand flexibility within As$_2$**6**$_3$, in the solid state the ligand is fully extended and the C_3 symmetry of the complex is maintained. This bonding arrangement allows for the expected *anti* conformation for the phenyl rings on the ethylene spacer.

Similarly, Sb···Sb distances trend with ligand length (Table 2). Compared to As···π, the relatively stronger Sb···π interaction can provide for shorter E···π contacts although this is not observed here due to the constraints imposed by the rigid ligand framework and the relatively longer Sb-S bonds.[7,14] The stronger Sb···π interaction may cause twisting of the ligands in Sb$_2$**1**$_3$ to allow for shorter contacts than would be present without twisting. Due to the naphthalene group on H$_2$**2**, twisting within E$_2$**3**$_3$ assemblies is limited sterically: while the S···S distances in H$_2$**1** and H$_2$**2** are the same, the Sb···Sb distances for Sb$_2$**1**$_3$ (4.30 Å) and Sb$_2$**2**$_3$ (4.83 Å) differ by > 0.5 Å. This is remarkable because the As···As distances in As$_2$**1**$_3$ and As$_2$**2**$_3$ vary by < 0.1 Å. This larger difference in distances within the antimony cryptands is manifested by the tight helical twist found in the Sb$_2$**1**$_3$ complex.

As expected, cavity volumes trend roughly with ligand length: the volume increases in concert with the S···S distance (Table 2). However, the ligands in As$_2$**3**$_3$ are folded into the cavity, resulting in a smaller than expected volume in the solid state (51 Å^3). The cavities in As$_2$**6**$_3$ and As$_2$**7**$_3$ are also smaller than expected, a result of the relatively narrow ligands not completely enclosing a well-defined cavity. The volumes of the corresponding As- and Sb-containing cryptands are approximately equal.

The S-E-S bond angles and E-S bond distances were measured and the averages for each complex are listed in Table 2. The E-S bond distances do not vary much from complex to complex, averaging 2.24 Å for As-S bonds and 2.44 Å for Sb-S bonds. The S-E-S angles vary slightly more. In the arsenic complexes, the individual (not average) angles range from 90.6° to 103.0° with an average of 95.4°. In the antimony complexes, these angles range only from 89.7 to 94.4° with an average angle of 92.6°. As$_2$**3**$_3$ has the most diverse set of observed angles which is not surprising given the lack of symmetry in the complex.

The degree of helicity in the cryptands was measured as the offset of the methylene carbons on each ligand. It was found to range from 6° (nearly untwisted) for As$_2$**2**$_3$ to 65° for As$_2$**7**$_3$. In general, greater E··E distances have larger degrees of helicity, but this can vary greatly depending

on ligand orientation. This is evidenced by the structures of co-crystallized $Sb_2\mathbf{8}_3(1)$ and $Sb_2\mathbf{8}_3(2)$ in which the methylene carbons are offset by pitches 39.9° and 9.1°, respectively, but only differ in Sb⋯Sb distances by 0.05 Å.

5. Discussion of Pnictogen-π Interactions

Lewis acid/base adducts formed by interactions between pnictogens and arene rings have been rigorously studied by Schmidbaur and co-workers, although only recently have they been used in a supramolecular context as a structural motif in the design of larger, higher order assemblies.[9-14, 16] Pnictogen-π interactions are defined as short contacts (less than the sum of the respective van der Waals radii) between the trivalent metalloid center and arene carbon atoms; the attractive interaction is measured between the pnictogen-center and the centroid of these close contacts. η^2-coordination is typically observed, though in some cases hapticity can be as high as η^6 when sterically demanding ring substituents center the metal over the ring.[11,17] In the crystal structure of each cryptand, short As⋯π contacts are observed (Table 2). The apparent C_3 symmetry of all of the structures except $As_2\mathbf{3}_3$ results in approximately equal E⋯π contacts between each metal center and each ligand. The cryptand with the shortest average E⋯π contacts (3.25 Å) is $As_2\mathbf{7}_3$, while $As_2\mathbf{5}_3$ had the longest average contacts (3.33 Å). This very narrow range of contact distances does not correlate to the E⋯E distance or the length of the ligand spacer. Additionally, the hapticity observed for each structure (η^2) was not affected by the length of the ligand.

6. Analysis of Chirality in E_2L_3 Cryptands

If considered a chelate, the pnictogen-π contact completes a five-membered chelate-type ring that contains arsenic or antimony, the thiolate sulfur, the methylene carbon, and the two aryl carbons (*ipso* and *ortho*) involved in the η^2-E⋯π interaction. The bidentate nature of the primary/secondary coordination spheres creates a distorted octahedral coordination environment around the pnictogen center. In the solid state, the coordination environments of all observed E_2L_3 cryptands possess a conformational chirality which can be described with established stereochemical conventions. The absolute configuration of the pnictogen coordination domain is defined by the direction of torsional twist observed along the C_3 axis. A clockwise twist is designated as Δ and a counter-clockwise twist is designated as Λ (Figures 3-5).[18,19]

As$_2$**1**$_3$, As$_2$**4**$_3$, and Sb$_2$**2**$_3$ cryptands are "mesocates" - one pnictogen center is Δ and the other is Λ and the ligand domain is not significantly twisted - there is very little, if any, degree of helicity (Figure 7).[20] On the other hand, Sb$_2$**1**$_3$, Sb$_2$**8**$_3$, As$_2$**8**$_3$ and As$_2$**5**$_3$ - As$_2$**7**$_3$ are helicates in which helicity is observed in the ligand domain and both pnictogen centers have identical stereochemistry. The ligands of As$_2$**3**$_3$ adopt an asymmetric conformation in the solid state, resulting in the crystallization of a racemic pair of helices: $\Delta,\Lambda M$-As$_2$**3**$_3$ and $\Delta,\Lambda P$-As$_2$**3**$_3$. Here, M designates a left-handed twist in the ligand domain and P designates a right-handed twist (Figures 3-5).[10] All helical structures crystallize as racemic mixtures of enantiomers (Δ,Δ and Λ,Λ). For the sake of simplicity, only Δ,Δ isomers are shown and discussed. These complexes are examples of chiral structures originating from coordination assemblies lacking chiral components.[20,21]
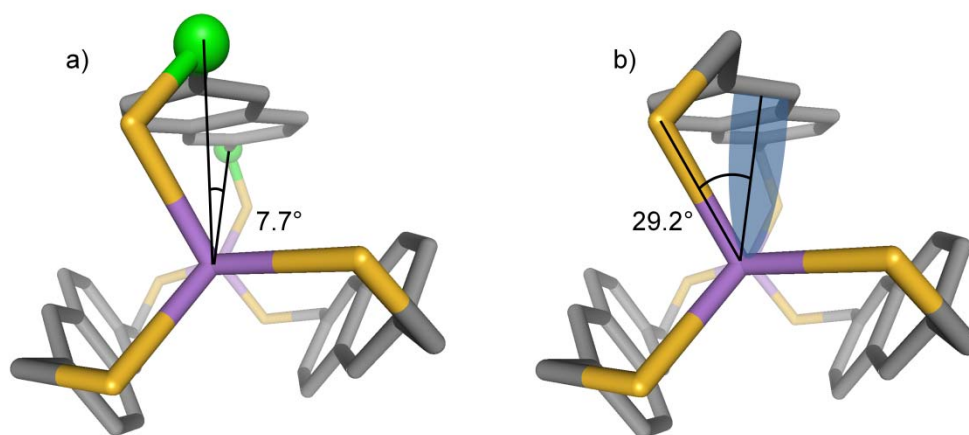
Figure 7. Illustrations of degree of helicity and twist angle of E coordination domains (a) Degree of helicity was measured as an average of the three –CH$_2$-E-E-CH$_2$- torsion angles; -CH2- carbon atoms (highlighted green). (b) Twist angle was estimated as the torsion angle between a sulfur, a centroid defined using the three sulfurs, the E center, and the closest aryl contact.

In general, there are three origins of helicity in metallosupramolecular architectures: 1) helical induction by intramolecular effects, 2) axial chirality in the ligands, and 3) helical induction by intermolecular interactions.[18,19,22] Presumably, cryptands adopt the degree of helicity necessary to reach a conformation in which interactions that promote twisting of the ligand domain are balanced with interactions that oppose twisting. Interactions that promote twisting in the ligand domain include favorable ligand-ligand interactions and E⋯π interactions. An E⋯π distance of about 3.3 Å is remarkably preserved across all observed cryptands. This is evidence that the E⋯π

interaction is significant to the conformation, and thus the stereochemistry of these cryptands. Steric interactions between individual components of an assembly could be considered interactions which would oppose helical twisting. For instance, in the smaller, non-helical cryptands such as $As_2\mathbf{1}_3$, twisting is limited by the unfavorable steric interactions which would result from short As-As distances. The bulky ligands of the non-helical $As_2\mathbf{2}_3$ and $As_2\mathbf{4}_3$ cryptands exacerbate the effects of the interactions opposing twisting due to unfavorable steric clash between neighboring ligands in the cryptand. For $As_2\mathbf{5}_3$, $As_2\mathbf{6}_3$, and $As_2\mathbf{7}_3$, these cryptands are large enough to allow twisting up to the point that steric interactions predominate.

With the exception of the highly asymmetrical $As_2\mathbf{3}_3$, the observed helical structures have E centers of identical chirality (i.e. $\varDelta,\varDelta$ or $\varLambda,\varLambda$) while the non-helical structures possess $\varDelta,\varLambda$ configurations. Since $\varDelta$ and $\varLambda$ configurations of the pnictogen coordination environments are energetically equal, it is reasonable to suspect that the helicity in the ligand domain (or lack thereof) gives rise to the relative configurations (pairing or non-pairing) of chirality of the E centers and not the other way around.

Since helicity results in the coordination environments of the E centers being offset from one another (i.e., the sulfur atoms are not eclipsed), in order for the two E centers in helical cryptands to have equivalent environments, they must have identical stereochemical configurations. We observe that a small degree of helicity may allow for $\varDelta,\varLambda$ configuration of the E coordination domains. For example, $As_2\mathbf{2}_3$ has a small (6°) degree of helicity yet maintains $\varDelta,\varLambda$ configuration. A unique coupling relationship exists between the stereochemical domains. In related dinuclear assemblies (e.g., double, triple, and quadruple-stranded metallohelicates) the helicity is coupled to the *absolute* stereochemical configuration of each metal center. For instance, in the bis-chatecolate structures studied by Raymond and co-workers, the metal coordination domains of *P*-helices all have $\varDelta,\varDelta$ configurations as a result of strong mechanically coupling between the metal centers.[22] In our structures, the *absolute* stereochemistry of the E coordination domains is *de*coupled from that of the helical domain. However, the coupling of the *relative* stereochemistry of the two E coordination domains to the ligand domain is still intact. In cryptands with significant helical twist, the E coordination domains have the same stereochemistry, while in non-helical cryptands, the E coordination domains have opposite stereochemistry (the cryptands are "meso"). The unrestricted rotation around the sulfur-methylene bonds seems to be sufficient to decouple the absolute

stereochemistry of the ligand domain from that of the As and Sb coordination domains. In related metallohelicates, the ligands are much more rigid and no similar rotation is possible.[21,22]

	As$_2$**4**$_3$	As$_2$**5**$_3$	As$_2$**6**$_3$	As$_2$**7**$_3$	As$_2$**8**$_3$	Sb$_2$**8**$_3$
Formula	C30 H36 As2 S6	C54 H42 As2 S6	C48 H48 As2 S6	C48 H36 As2 S6	C36.33 H30.33 As2 Cl S6	C37.25 H31.38 Cl3 N0.13 S6 Sb2
Formula weight	738.79	1033.08	967.06	954.97	844.59	1022.96
Temperature/K	173(2)	173(2)	173(2)	173(2)	173(2)	173(2)
Wavelength/Å	0.71073	0.71073	0.71073	0.71073	0.71073	0.71073
Crystal System	Monoclinic	Monoclinic	Monoclinic	Monoclinic	Hexagonal	Rhombohedral
Space Group	P2(1)/n	C2/c	C2/c	C2/c	R-3c	R-3
a/Å	14.4540(6)	26.660(7)	30.468(3)	31.093(2)	21.3256(7)	21.0255(7)
b/Å	12.6952(5)	10.399(3)	13.6420(12)	13.5902(10)	21.3256(7)	21.0255(7)
c/Å	17.6319(7)	20.779(6)	11.0855(10)	10.6951(8)	41.358(3)	21.0255(7)
α/°	90	90	90	90	90	69.14
β/°	90.1500(10)	125.192(7)	106.3970(10)	107.090(1)	90	69.14
γ/°	90	90	90	90	120	69.14
V/Å^3	3235.4(2)	4708(2)	4420.2(7)	4319.7(6)	16288.8(13)	7831.4(5)
Z	4	4	4	4	18	8
D_{calcd}/g cm^{-3}	1.517	1.458	1.453	1.468	1.550	1.735
μ/cm^{-1}	2.473	1.723	1.829	1.871	2.293	1.932
F(000)	1512	2112	1992	1944	7692	4038
Crystal size/mm	0.32 x 0.06 x 0.04	0.07 x 0.06 x 0.05	0.37 x 0.14 x 0.04	0.18 x 0.16 x 0.12	0.36 x 0.28 x 0.18	0.16 x 0.16 x 0.08
Index ranges	-17<=h<=17	-34<=h<=17	-38<=h<=38	-39<=h<=39	-27<=h<=27	-26<=h<=26
	-15<=k<=15	-13<=k<=11	-17<=k<=17	-17<=k<=17	-27<=k<=27	-26<=k<=26
	-20<=l<=20	-24<=l<=26	-14<=l<=14	-13<=l<=13	-52<=l<=52	-26<=l<=26
Reflections collected	30492	9193	24133	19714	58788	88616
Independent Reflections [R$_{int}$]	5689 [0.0546]	4993 [0.0856]	4837 [0.0417]	4719 [0.0416]	3969 [0.0307]	11413 [0.0556]
Data/restraints/ Parameters	5689 / 0 / 343	4993 / 0 / 280	4837 / 0 / 253	4719 / 0 / 325	3969 / 0 / 199	11413 / 0 / 577
Goodness-of-fit on F^2	1.066	1.004	1.088	1.091	1.075	1.37
R1/wR2 [I > 2σ(I)]	0.0456/0.1025	0.0756/0.1014	0.0468/0.1210	0.0418/0.0884	0.0385/0.1041	0.0633/0.1789
R1/wR2 (all data)	0.0651/0.1123	0.1626/0.1318	0.0670/0.1416	0.0616/0.1004	0.0447/0.1081	0.0810/0.1886
Largest diff. peak and hole/e Å^{-3}	0.571/-0.289	0.752/-0.453	1.064/-0.452	0.609/-0.233	1.145/-0.498	1.900/-1.630

Table 1. Crystallographic data and refinement parameters

Complex	E···π (Å)[a]	Stereochemical Configuration[b]	E···E (Å)	Twist Angle (°)[c]	Degree of Helicity[d] (°)	Interior Volume (Å³)[e]	E-S (Å)	S-E-S (°)	Reference
As₂1₃	3.30	Δ,Λ	5.03	36.6	-	38	2.25	94.6	9
As₂2₃	3.30	Δ,Λ,P	5.11	35.7	6.0	44	2.25	94.2	6
As₂3₃	3.35	Δ,Λ,M+P[f]	9.19	39.1	-	55	2.24	97.3	10
As₂4₃	3.31	Δ,Λ	5.09	34.7	-	38	2.25	94.1	-
As₂5₃	3.33	Δ,Δ,P	9.52	33.3	29.5	90	2.25	94.8	-
As₂6₃	3.30	Δ,Δ,M	11.71	27.3	54.3	67	2.24	96.1	-
As₂7₃	3.25	Δ,Δ,M	12.28	23.5	65.8	64	2.24	97.5	-
As₂8₃	3.29	Δ,Δ,P	7.55	29.2	7.7	72	2.24	94.7	-
Sb₂1₃	3.31	Δ,Δ,P	4.30	43.0	12.7	36	2.43	92.0	12
Sb₂2₃	3.34	Δ,Λ	4.83	33.7	-	46	2.42	91.5	6
Sb₂8₃ (1)[g]	3.31	Δ,Δ,M	6.44	40.0	39.9	63	2.42	91.1	-
Sb₂8₃ (2)	3.36	Δ,Δ,M	7.01	29.1	9.1	74	2.44	91.3	-

Table 2. Stereochemical outcomes and selected geometric information for E_2L_3 assemblies. (a) Measured as the average distance between E center and centroid of close contacts with neighboring arene rings. (b) See Figures 3-5 for examples of helical domain designations. To simplify discussion, for homoconfigurational cryptands only the Δ,Δ isomers are shown. (c) Twist of the octahedral coordination environment - estimated as the torsion angle between a sulfur, a centroid defined using the three sulfurs, the E center, and the closest aryl contact. (d) Reported as an average of the three –CH₂-As-As-CH₂- torsion angles. (e) Cavities were measured using solvent (0.7 Å) surfaces in WebLab ViewerPro 4.0. Cavity volumes were estimated as the difference between the volume of the E_2L_3 cryptand filled with chloride atoms and the E_2L_3 cryptand with a void cavity. (f) (Δ,Λ,M)- and (Δ,Λ,P)-As₂L²₃ form as a racemic mixture. (g) There are two different polymorphs observed in the same crystal, Sb₂8₃(1) and Sb₂8₃(2).

6. Summary

In this report, the X-ray crystal structures of six new As_2L_3 and Sb_2L_3 supramolecular cryptands were analyzed in the context of previously reported As- and Sb-cryptands. A new vacuum-enabled synthesis allowed for the formation of two of these new assemblies which could not be prepared by other routes. Comparing the stereochemistries of these cryptands, revealed that in cryptands with significant helicity the As and Sb coordination environments showed identical stereochemistry (i.e., Δ,Δ or Λ,Λ), whereas all non-helical cryptands were mesocates (Δ,Λ-configuration). The degree of helicity determines the stereochemical relationship between the As and Sb coordination environments. The pnictogen-π interaction is an anchoring point for a chelate ring and influences the degree of helicity and overall stereochemistry in observed cryptands. This reinforces the conclusion that pnictogen-π interactions are important supramolecular forces in directing the conformations of main group element-containing structures, and thus are important to the design of these complexes.

CHAPTER VI

CONCLUDING REMARKS AND FUTURE PERSPECTIVES

Since the surface of a material essentially defines the material's functionality, research into new methods for fabrication of surface architectures and surface functionalities is critical to the science of materials. This dissertation has described the surface anatomy, construction, and functionalization of mesoporous silica. The application of mesoporous silica and similar meso- and nanoscale materials as sorbents was reviewed along with relevant figures of merit for sorbent materials. Our initial investigations describe novel supramolecular functionalization motifs for modification of mesoporous silica and iron oxide nanoparticles and serve to highlight the advantages and challenges of supramolecular modification of materials. We have shown that it is possible to create a persistent surface based on an arene-arene interaction motif and have identified the contributions of each component of the material on the stability of the modified surface. We have also demonstrated a surface modification motif based on the well-known host-guest chemistry of cyclodextrin and have similarly explored the component contributions to the state of the modified material. Finally, we have obtained evidence regarding the role that the relatively un-studied supramolecular pnictogen-π interactions play in the conformations of E_2L_3 Cryptands.

Although we have successfully produced, characterized, and evaluated two novel surface interaction motifs, this work is only a hint at the possibilities of supramolecular surface modification. This dissertation has established a foundation for design and evaluation of supramolecular surface modification motifs. One of the most promising advantages of supramolecular modification, that it allows modification of surfaces with sophisticated and delicate functionalities, was not part of the scope of this work.

APPENDIX

EXPERIMENTAL DETAILS FOR CHAPTERS III, IV, AND V

1. Chapter III

Commercially available reagents were used as recieved unless otherwise noted. MCM-41 was provided by PNNL where it was prepared according to methods in reference 1.

Synthesis of Ph-SAMMS

In a typical preparation of Ph-SAMMS, MCM-41 (5.1 g) with 3.5 nm pores was stirred in dry toluene (50 mL) for 30 min. H_2O (1.2 ml) was added and this was stirred for an additional hour. Trimethoxyphenysilane (3.95 g) was added and the reaction was heated to reflux. After 1 h of reflux and again after 18 h the reflux condenser was replaced with a distillation apparatus and methanol was distilled (via azeotrope at 65 °C). The reaction was filtered hot through a fritted funnel and subsequently washed three times with methanol (200 mL). The white powdery material was dried at room temperature for 2 h and then placed under vacuum for 6 h. This method yielded a material with 1.6 phenyl rings per nm^2.

Synthesis of SH-bearing organics

2-mercaptomethylnaphthalene (BM) was prepared as follows. 2-bromomethylnaphthalene (4.26 g) and thiourea (2.2 g) were dissolved in acetone (180 mL). This solution was refluxed for two hours and the white solid thiouronium salt was filtered, washed three times with acetone (100 mL), dried under vacuum, and used without further purification. The crude thiouronium salt was dissolved in degassed 2 M aqueous NaOH (180 mL). This was heated to 90 °C and this temperature was maintained for 2 h under argon. After cooling, degassed HCl (4 M) was added slowly *via* cannula until the pH of the mixture was acidic. The thiol product was extracted into

dichloromethane, dried with Na_2SO_4, and evaporated to dryness. White, crystalline product was obtained in 91% yield.

Metal Uptake Studies

Metal uptake studies were carried out using filtered Columbia River water (pH 7.8) from Hanford, Washington, doped with 50 ppb each target metal. Prepared metal solutions (10 mL) were aliquoted into polypropylene tubes and spiked with a small volume of sorbent suspended in deionized water to obtain the liquid-to-solid ratios of 5000. Phenyl-SAMMS sorbents was preconditioned with one microliter of methanol per 2 mg sorbent to enable effective surface wetting. Contact times were 2 h with agitation at 60 Hz on an orbital shaker. After contact, the water was filtered through a 0.2 micron filter and Hg, Cd, Ag, and Pb content were analyzed using ICP-MS (Agilent 7500 ce, Agilent Technologies, CA). Ge and In were used as internal standards for metals of similar mass at 10 ppb. All samples were run in triplicate.

Synthesis of lauric acid Fe_3O_4 nanoparticles

These particles were prepared by Cynthia Warner following the method described in reference 2: $Fe(acac)_3$ (6 mmol), 1,2-hexadecanediol (30 mmol), lauric acid (18 mmol), and laurylamine (18 mmol) were dissolved in benzyl ether (80 mL) and heated to 300 °C at a rate of 4 °C min^{-1} under argon. The solution was refluxed for 30 minutes, cooled to room temperature, transferred to conical vials (50 mL), and ethanol (20 mL) was added to each vial. The tubes were centrifuged, the supernatant decanted, and the pelleted nanoparticles suspended in ethanol. This process was repeated until the obtained supernatant was clear. The black solid was suspended in hexanes and centrifuged to remove insoluble particle aggregates. The particles remaining in hexanes following centrifugation were then collected and dried under argon.

Synthesis of benzoic acid Fe_3O_4 nanoparticles by ligand exchange

Lauric Acid Fe_3O_4 NPs were suspended in toluene (2 mL) and combined with benzoic acid (15 mg/ml) dissolved in methanol (2 mL). The mixture was stirred for 18 h at room temperature. The nanoparticles were retrieved by magnetic decantation then washed several times with ethanol, acetone, and water to remove lauric acid and excess benzoic acid. The benzoic acid Fe_3O_4 NPs were dried under argon.

Application of 2-mercatomethylnaphthalene to benzoic acid Fe₃O₄ nanoparticles

Benzoic acid Fe_3O_4 nanoparticles (60 mg) were suspended in dichloromethane (10 mL) by sonication for 20 min in a scintillation vial. MN (65 mg) was dissolved in dichloromethane (5 mL) and added to the nanoparticle suspension. This mixture was incubated for 24 h with agitation at 60 Hz. The vial was then uncapped and the solvent allowed to evaporate. Nanoparticles were then suspended in methanol (5 mL) by sonication for 5 minutes. They were then retrieved by magnetic separation. This methanol wash was performed three times followed by a water wash.

Thermal gravimetric analysis

TGA was performed on a TA Instruments© Q500 using platinum pans, air as the balance gas and N_2 as the purge gas. The heating program was as follows: Ramp 5 °C/min to 110 °C, isothermal for 30 min, ramp 5 °C/min to 1000 °C, isothermal for 10 minutes, end. All TGA experiments were run in triplicate.

Ellman's Test for Thiols

Ellman's reagent, 5,5'-Dithiobis(2-nitrobenzoic Acid), was purchased from TCI America. The tests were performed an aqueous sodium phosphate (0.1 M) buffer containing EDTA (1 mM) adjusted to pH 7.8. The extinction coefficient was determined using cysteine as a thiol standard and was measured at peak absorbance near 412 nm. Before measurement all solutions were filtered through a 0.2 micron filter. The Ellman's test is time-sensitive and all measurements were performed 11-20 minutes after addition of the Ellman's reagent to the material or standard solution. For Ph-SAMMS materials, one microliter of methanol per 2 mg sorbent was added to facilitate surface wetting. All Ellman's tests were performed in triplicate. When the results for the Ellman's tests are compared to TGA measurements of the same material, the tests typically differ by 1-3% if at all. The Ellman's test yields the lower value. This is may be due to the kinetic restriction mass transport through the material during the timeline of the Ellman's experiment.

2. Chapter IV

Davisil® (160 Å) was purchased from Sigma-Aldrich and was refluxed in toluene for 18 h before analysis. Unless otherwise noted, mesoporous materials were dried in a vacuum oven for at least 24 hours before analysis.

Preparation of Amino-SAMMS

Davisil® (2 g) and water (67 mg) were added to toluene (150 mL) and stirred for 1 h. (3-Aminopropyl)triethoxysilane (267 mg, 1.21 mmol) was added and the reaction was refluxed for 18 h. After 1 h of reflux and again after 18 h the reflux condenser was replaced with a distillation apparatus and ethanol was distilled (via azeotrope). The reaction was filtered hot through a fritted funnel and subsequently washed three times with methanol (200 mL). The white powdery material was dried at room temperature for 2 h and then placed under vacuum for 6 h. This method yielded Amino-SAMMS having 1.1 amines per nm^2.

Purification of *p*-toluenesulfonyl chloride (TsCl)

TsCl (40 g, 210 mmol) was dissolved in chloroform (100 mL), stirring, at room temperature. The resulting cloudy brown solution was filtered through a medium sintered glass frit, yielding a clear brown filtrate. Petroleum ether (500 mL) was added to precipitate impurities which were removed by filtration through a medium glass frit. The solution was clarified with charcoal, separated by filtration, and evaporation to dryness which yields white, crystalline product (37 g, 92%).

Synthesis of mono-6-deoxy-6-(*p*-toluenesulfonyl)-β-cyclodextrin (β-CD-OTs)

A solution of potassium hydroxide (17.5 g) in water (700 mL) was cooled to 0 °C in an ice/brine bath, and β-CD (25 g, 22 mmol) was added and dissolved, stirring. The colorless solution was kept stirring at 0°C while *p*-toluenesulfonyl chloride was added (10 g, 52.5 mmol). After stirring the resulting cloudy white mixture at 0 °C for 2.5 hours, carefully monitoring the temperature, a second portion of *p*-toluenesulfonyl chloride (15 g, 78.5 mmol) was added. The mixture was stirred for an additional 3 hours and subsequently filtered through celite in a medium sintered glass funnel, keeping the filtrate cold. 10% aqueous hydrochloric acid (175 mL) was slowly added, still keeping filtrate cold. The filtrate turned milky white as it was acidified, indicating formation of a fine precipitate. The filtrate was refrigerated overnight, collected on a medium frit and dried *in vacuo*, yielding a white powder (12 g, 42%).

Synthesis of mono-6-deoxy-6-azido-β-cyclodextrin (β-CD-N$_3$)

β-CD-OTs (7.37 g, 5.71 mmol) was dissolved in DMF (22 mL) and heated to 60 °C, stirring, yielding a clear, colorless solution. Potassium iodide (0.474 g, 2.86 mmol) was added, turning the solution clear yellow, followed by sodium azide (3.71 g, 57.1 mmol). The resulting cloudy yellow-white mixture was stirred at 60 °C for 24 hours. The mixture was allowed to cool to room temperature, then added to an excess of acetone/water (4:1 v/v) to precipitate product and dissolve salts. The fine white precipitate was collected on a medium sintered glass frit and dried in vacuo, yielding a white powder (5.834 g, 88%).

Synthesis of β-CD-SAMMS

Amino-functionalized silica gel (1 g) was suspended in DMF (6 mL) at room temperature, stirring. CO_2 was bubbled through for 2 min. Bubbling was continued while β-CD-N$_3$ (0.37 g, 0.319 mmol) was added, then mixture was stirred for 5 min. Bubbling was continued while PPh$_3$ (.037 g, 0.141 mmol) in DMF (6 mL) was added. The mixture was stirred at room temperature for 24 hours with continuous bubbling of CO_2. The solid was collected by vacuum filtration and dried *in vacuo*.

Attachment of 1-adamantanethiol and 2-mercaptomethylnaphthalene to β-CD-SAMMS

1-adamantanethiol (4 mg, 0.0238 mmol) was dissolved in chloroform (2 mL) and β-CD silica (0.150 g, 0.0060 mmol) was added. The resulting suspension was shaken at room temperature for 2 hours. Solvent was allowed to evaporate overnight, leaving a slightly yellow powdery product.

Synthesis of Ad-SAMMS

2 g of Amino-SAMMS (0.25 amines/nm^2) were suspended in acetonitrile along with triethylamine (20 mL) and stirred under inert atmosphere for 2 h. 1-adamantanecarbonyl chloride (0.25g, 1.26 mmol) was added and the reaction was stirred for 24 h at ambient temperature under

inert atmosphere.   Ad-SAMMS was separated by vacuum filtration, washed as follows. Twice with CH_3CN (20 mL), twice with 95% ethanol (20 mL), twice with dichloromethane (20 mL), once with 100 mL DI water, twice with saturated potassium carbonate (40 mL), and once more with DI water (200 mL).

Attachment of β-cyclodextrin to Ad-SAMMS

β-cyclodextrin (24 mg) was dissolved in H_2O (10mL) by stirring for 10 minutes. Ad-SAMMS (150 mg) was added to the stirring mixture and stirred 24 h. The material was collected by vacuum filtration.

Thermal gravimetric analysis

See Section 1, this appendix

Stability tests using Ellman's Test for Thiols

See Section 1, this appendix.

3. Chapter V

^{1}H NMR spectra were measured using a Varian INOVA-300 spectrometer operating at 299.935 MHz. *J* values are given in Hz. *Warning: Arsenic and its complexes are highly toxic! Use appropriate safety precautions.*

$As_2 4_3$ cryptand

2,3-dimethyl-1,4-bis(mercaptomethyl)-benzene[3] (H_2**4**, 0.160 g, 0.807 mmol) was dissolved in $CHCl_3$ (100 mL) under N_2. 0.1 M KOH in MeOH (20 μL) was added. The reaction mixture was stirred at 55 °C and $AsCl_3$ (45.8 μL, 0.537 mmol) was added, causing precipitation of a white solid. After 2 h the suspension was cooled to room temperature and filtered through glass wool to yield a white powder. The powder was dissolved in DCM which was washed with H_2O (50 mL), brine (3× 50 mL), and concentrated under vacuum, yielding a white solid, As_2**2**$_3$.   Crystals suitable for X-ray analysis were grown by the slow diffusion of hexanes into a $CHCl_3$ solution of As_2**4**$_3$.

2,5,4′-Trimethylbenzophenone (5a)

AlCl$_3$ (100 g, 750 mmol) was added to a 1 L round bottom flask and covered with CS$_2$ (150 mL). *p*-Xylene (69 g, 650 mmol) and *p*-toluoyl chloride (100 g, 646 mmol) were dissolved in CS$_2$ (75 mL) and added slowly to the stirring suspension of AlCl$_3$ in CS$_2$. After the addition was complete and the reaction mixture reached room temperature, the suspension was stirred at reflux for 2 h. The reaction mixture was cooled in an ice bath and 200 mL of H$_2$O was added slowly while stirring. The resulting mixture was extracted with 500 mL of diethyl ether. The organic phase was washed with H$_2$O (3 × 200 mL), 10% NaOH (2 × 250 mL), and again with H$_2$O (2 × 200 mL). The organic phase was dried with sodium sulfate and concentrated under vacuum yielding a white solid. Vacuum distillation (110-120 °C, 0.05 mmHg) provided 2,5,4′-trimethylbenzophenone (**5a**) as a blue powder. (117.5 g, 81% yield). ^{1}H NMR (300 MHz; CDCl$_3$; Me$_4$Si) δ 7.70 (d, 2 H, C*H*, *J* 8.1), 7.19 (m, 5 H, C*H*), 2.423 (s, 3 H, C*H*$_3$), 2.325 (s, 3 H, C*H*$_3$), 2.248 (s, 3 H, C*H*$_3$).

Anthraquinone-2,6-dicarboxylic acid (5d)

2,5,4′-trimethylbenzophenone (**5a**, 555 g, 245 mmol) was heated at reflux (<360 °C) under air for 6 h with vigorous stirring. The reaction mixture was then cooled to room temperature to give an orange solid. The solid was triturated with ether (10 mL) and the insoluble portion was collected by vacuum filtration and washed with cold ether. The solvent from the combined filtrate and ether washings was removed under reduced pressure and triturated again as described above. After repeating this process four times, 35 g of ether-insoluble material was collected. Recrystallization from CS$_2$ gave a 3:2 mixture of 2,6-dimethyl-9(10H)-anthracenone (**5b**) and 2,6-dimethylanthracene (**5c**) as a yellow solid (15 g, 28% yield). The crude mixture was used without further purification.

CrO$_3$ (59.4 g, 594 mmol) was added to a well-stirred solution of sulfuric acid (2 mL), acetic anhydride (15 mL, 160 mmol), and acetic acid (350 mL) and cooled to 20 °C in an ice bath. Maintaining a reaction temperature below 35 °C, the mixture of **5b** and **5c** (11.6 g, ~54.0 mmol) was added in small portions and then stirred for 2 h. *Warning: This reaction is highly exothermic. Chromium trioxide is a strong oxidizing agent and chromium byproducts of this reaction are toxic. This procedure should be conducted with care, especially at this scale.* It was then heated to 120 °C for 3 h, cooled to room temperature, and poured into H$_2$O (2 L). The resultant precipitate was removed by vacuum filtration, washed with H$_2$O, and dried in a vacuum oven to afford 2,6-

anthraquinonedicarboxylic acid (**5d**) as a yellow solid (15.4 g, 96.2% yield). ^{1}H NMR (300 MHz; DMSO) δ 8.70 (s, 2 H, C*H*), δ 8.44 (d, 2 H, C*H J* 7.8), δ 8.36 (d, 2 H, C*H J* 8.1).

Dimethyl 2,6-anthracenedicarboxylate (5h)

CuSO$_4$ (0.8 g, 5 mmol), metallic Zn (94.2 g, 1.44 mol), and concentrated NH$_4$OH (715 mL) were stirred in a 2 L round bottom flask in an ice bath as 2,6-anthraquinonedicarboxylic acid (**5d**, 30.2 g, 102 mmol) was added slowly. After complete addition the reaction was heated to 100 °C and additional concentrated NH$_4$OH (715 mL) was added over 4 h. The reaction was complete when the red color dissipated and the mixture became clear (if after 4 h the reaction remained red, additional CuSO$_4$ (2.4 g, 15 mmol) was added in portions to drive the reaction to completion). Upon completion the mixture was cooled and filtered. The filtrate was acidified with 12 M HCl to give a bright yellow precipitate which was collected by vacuum filtration and dried in a vacuum oven to yield a 1:2 mixture of anthracene-2,6-dicarboxylic acid (**5e**) and 9,10-dihydroanthracene-2,6-dicarboxylic acid (**5f**) as a bright yellow solid (27.14 g, 99% yield) which was used without further purification.

A suspension of the mixture of **5e** and **5f** (27 g, ~0.10 mol), iodomethane (142 g, 1.00 mol), and lithium carbonate (74 g, 1.0 mol) in DMF (1300 mL) was stirred for 24 h and then added to 1 M HCl (5 L). The resulting yellow precipitate was collected by vacuum filtration and dried in a vacuum oven to give a 2:1 mixture of dimethyl 9,10-dihydro-2,6-anthracenedicarboxylate (**5g**) and dimethyl 2,6-anthracenedicarboxylate (**5h**) (20.9 g, 70% yield).

2,3-Dichloro-5,6-dicyano-1,4-benzoquinone (DDQ, 7.5 g, 30 mmol) was added to the mixture of **5g** and **5h** (6.8 g, 23 mmol) in benzene (278 mL) and the suspension was stirred at reflux for 1 h. After cooling to room temperature the solid was collected by vacuum filtration. The solid was washed with methanol and dried in a vacuum oven to give dimethyl 2,6-anthracenedicarboxylate (**5h**) as a bright yellow solid (6.061 g, 90% yield). ^{1}H NMR (300 MHz; CDCl$_3$; Me$_4$Si) δ 8.83 (s, 2 H, C*H*), 8.59 (s, 2 H, C*H*), 8.06 (m, 4 H, C*H*), 4.02 (s, 6 H, C*H$_3$*).

2,6-Bis(bromomethyl)anthracene (5j)

Dimethyl 2,6-anthracenedicarboxylate (**5h**, 2.13 g, 7.23 mmol) was suspended in freshly distilled THF (225 mL) and stirred in an ice bath. LiAlH$_4$ (0.415 g, 11 mmol) was added slowly to the yellow suspension and the reaction mixture was stirred for an additional 40 min on ice and then

heated to reflux for 1 h. The mixture was cooled to room temperature and EtOAc (100 mL) was added to quench any remaining LiAlH$_4$. The solvents were removed under reduced pressure to afford a pale yellow solid. 6 M HCl (400 mL) was added and the suspension was stirred briefly, filtered, washed with 6 M HCl (125 mL), and dried under vacuum to give 2,6-bis(hydroxylmethyl)anthracene (**5i**) as a pale yellow solid (1.72 g, 98.5%).

2,6-Bis(hydroxylmethyl)anthracene (**5i**, 1.0 g, 4.2 mmol) was suspended in freshly distilled DCM (160 mL) and stirred in an ice bath under N$_2$. A solution of PBr$_3$ (0.5 g, 1.8 mmol) in 17 mL DCM was slowly added to the yellow suspension. After 15 min. the reaction mixture was allowed to warm to room temperature and was stirred overnight (~17 h). The resulting green suspension was washed with 2 M NaOH (1 × 250 mL) and extracted with DCM (3 × 200 mL). The combined organics were washed with 2 M HCl (1 × 250 mL). The HCl wash was extracted with DCM (2 × 150 mL) which was added to the combined organics. The combined organics were washed with H$_2$O (1 × 250 mL), dried with brine (1 × 250 mL), Na$_2$SO$_4$, and evaporated under reduced pressure to afford 2,6-bis(bromomethyl)anthracene **(5j)** as a bright yellow solid (1.32 g, 86%). ^{1}H NMR (300 MHz; CDCl$_3$; Me$_4$Si) δ 8.37 (s, 2 H, CH), 7.98 (m, 4 H, CH), 7.51 (dd, 2 H, CH), 4.70 (s, 4 H, CH_2).

2,6-Bis(mercaptomethyl)anthracene (H$_2$5)

2,6-Bis(bromomethyl)anthracene (**5j**, 1.7 g, 467 mmol) and thiourea (1.07 g, 14 mmol) were suspended in acetone (60 mL) and stirred at reflux overnight (~15 h.). The mixture was cooled and filtered and the solid was washed with acetone to give 2,6-bis(thiouroniummethyl)anthracene bromide(**5k**) as a pale yellow solid. This salt was placed under N$_2$ and 2 M NaOH (~50 mL) was added via a pressure equalizing addition funnel. The reaction was stirred at reflux for 2 h. The pale yellow solution was cooled in an ice bath and 6 M HCl (~15 mL) was added which caused a pale yellow precipitate to form. The precipitate was collected by vacuum filtration and dried under reduced pressure overnight in a desiccator to afford 2,6-bis(mercaptomethyl)anthracene (H$_2$**5**) as a pale yellow solid (1.10 g, 88%). ^{1}H NMR (300 MHz; CDCl$_3$; Me$_4$Si) δ 8.26 (s, 2 H, CH), 7.90 (d, 4 H, CH, J 8.7), 7.39 (dd, 2 H, CH), 3.87 (d, 4 H, CH_2, J 7.5), 1.76 (t, 1 H, SH, J 7.6).

As₂5₃ cryptand

2,6-bis(mercaptomethyl)anthracene (H$_2$**5**, 0.060 g, 0.222 mmol) was placed under N$_2$ and a solution of freshly distilled THF (60 mL), MeOH (20 mL), and KOH (0.025 g, 0.444 mmol) was added *via* cannula. The reaction mixture was stirred at 55 °C and AsCl$_3$ (0.027 g, 0.148 mmol) was added, causing precipitation of a white solid. After 2 h the suspension was cooled to room temperature, filtered through glass wool, and concentrated under vacuum to afford crude As$_2$**5**$_3$ as a white powder (0.071 g, 54% yield). The powder was dissolved in benzene which was allowed to slowly evaporate, yielding X-ray quality crystals.

4,4'-bis(bromomethyl)dibenzyl (6a)

Dibenzyl (3.2 g, 17 mmol), paraformaldehyde (1.6g), and ZnBr (6g, 26 mmol) were added to 33% HBr/HOAc (30 mL) and stirred at 80 °C for 18 h. After cooling, the reaction mixture was poured into 200 mL H$_2$O and extracted with DCM. The organic extract was washed with saturated sodium bicarbonate solution and evaporated to dryness. Pure product (0.675g, 10%) was obtained by recrystallization from benzene. ^{1}H NMR (500 MHz; CDCl$_3$; Me$_4$Si) δ 7.31 (d, 4H, C*H*, *J* 8.0), 7.15 (d, 4H, C*H*, *J* 8.0), 4.49 (s, 4H, C*H$_2$*), 2.90 (s, 4H, C*H$_2$*).

4,4'-bis(mercaptomethyl)dibenzyl (H₂6)

6a (0.675 g, 1.8 mmol) and thiorea (0.334 g, 4.4 mmol) were dissolved in 15 mL ethanol and stirred at 70 °C for 16 h. After cooling, diethyl ether was added causing precipitation of a white solid. This salt was removed, washed with diethyl ether, and dried in a vacuum desiccator. The salt was dissolved in degassed 2M NaOH under N$_2$, and heated at reflux for 2 h. After cooling, degassed 4M HCl was added *via* cannula until an acidic pH was achieved, causing a white precipitate to form. This precipitate was removed by filtration, washed with acetone and H$_2$O, and dried in a vacuum desiccator (0.205g, 67%). ^{1}H NMR (300 MHz; CDCl$_3$; Me$_4$Si) δ 7.24 (d, 4 H, C*H*, *J* 8.3), 7.14 (d, 4 H, C*H*, *J* 8.1), 3.73 (d, 4H, C*H$_2$ J* 7.4), 2.88 (s, 4H, C*H$_2$*) δ 1.75 (t, 2H, S*H, J* 7.5).

As₂6₃ cryptand

H$_2$**6** (0.131 g, 0.47 mmol) was added to a flamed-dried 3-neck flask and placed under N$_2$. 0.102 M KOH in methanol (14.9 mL) was diluted with 50 mL dry THF, degassed, and added to H$_2$**7** *via* cannula. The mixture was heated to 55 °C and 30 μL AsCl$_3$ was slowly added. After

stirring at 55 °C for 2.5 h the solution was cooled, filtered through glass wool, and concentrated under vacuum. Slow evaporation yielded crystals suitable for X-ray diffraction analysis.

4,4'-dimethyltolan (7a)

A 500 ml Schlenk flask was charged with a stir bar, 4-iodotoluene (11 g, 51 mmol), $PdCl_2(PPh_3)_2$ (2.14 g, 3.05 mmol), and copper iodide (1 g, 5.2 mmol) and placed under N_2. In a separate flask DBU (41 ml, 270 mmol) was dissolved in acetonitrile (11 ml), degassed, and transferred to the reaction vessel *via* cannula. Trimethylsilylacetylene (TMSA) (3.6 ml, 25 mmol) was added via syringe. The reaction mixture was stirred at room temperature for 24 h. The solvent was evaporated to near-dryness and the remaining mixture poured into DCMwhich was washed with 1 M HCl and H_2O. The extract was dried over sodium sulfate and evaporated to dryness leaving a brown oily solid. The crude product was purified *via* a celite/silica/celite plug (10:1 hexanes:ethyl acetate) yielding a crystalline, colorless solid (60% isolated yield).   ^{1}H NMR (300 MHz; $CDCl_3$; Me_4Si) δ 7.42 (d, 4H, C*H*, *J* 8.1), 7.16 (d, 4H, C*H*, *J* 7.8), 2.37 (s, 6H, C*H*$_3$).

4,4'-bis(bromomethyl)tolan (7b)

A flame dried 3-neck 250 mL round bottom flask was equipped with a condenser and charged with a stir bar, 4,4'-dimethyltolan (0.5 g, 2.4 mmol)**, and *N*-bromosuccinimide (1.07 g, 6.06 mmol) and placed under N_2. Benzoyl peroxide (58 mg, 0.24 mmol) was dissolved in 130 ml of freshly distilled, degassed CCl_4. This benzoyl peroxide solution was transferred *via* cannula into the reaction vessel. The solution was heated to 60 °C for 23 hours. The reaction mixture was washed with 1 M HCl, 1 M NaOH, and deionized H_2O, dried over sodium sulfate and evaporated. The crude product (34% isolated yield) was washed repeatedly with diethyl ether, dried, and used without further purification. ^{1}H NMR (300 MHz; $CDCl_3$; Me_4Si) δ 7.53 (d, 4H, C*H*, *J* 8.7), 7.37 (d, 4H, C*H*, *J* 8.7), δ 4.49 (s, 4H, C*H*$_3$).

4,4'-bis(mercaptomethyl)tolan ($H_2$7)

4,4'-bis(bromomethyl)tolan (**7b**, 1.5 g, 4.1 mmol) and thiourea (1 g, 13 mmol) were dissolved in ethanol (120 mL) and 2 mL acetone was added to the mixture. The reaction was heated to reflux for 3 h. The precipitate was filtered and the white solid was rinsed with acetone and dried in a vacuum desiccator. The dried precipitate was dissolved in degassed 2 M NaOH (120

mL), placed under N_2, and stirred at reflux for 3.5 h. After cooling, 4 M HCl (degassed) was added *via* cannula until an acidic pH was achieved and the solution was extracted with DCM (3 × 100 mL) The extract was dried over sodium sulfate and evaporated to dryness, yielding a white solid (55% isolated yield). ^{1}H NMR (300 MHz; CDCl$_3$; Me$_4$Si) δ 7.48 (d, 4H, C*H*, *J* 8.1), 7.31 (d, 4H, C*H*, *J* 8.1), 3.75 (s, 4H, C*H*$_2$, *J* 7.8), 1.77 (t, 2H, S*H*, *J* 7.7).

As$_2$7$_3$ cryptand

H$_2$**7** (22 mg, 0.06 mmol) was dissolved in 8 ml of dried, degassed, DCM and AsCl$_3$ (7 µl, 0.027 mmol) was added slowly. X-ray quality crystals were obtained when pentane was slowly diffused (via vapor diffusion) into the solution.

As$_2$8$_3$ cryptand

2,6-bis(mercaptomethyl)naphthalene[4] (H$_2$**8**, 90.8 mg, 0.411 mmol) and AsCl$_3$ (23.4 µL, 0.274 mmol) were dissolved in CHCl$_3$ (125 mL) and stirred at 50 °C under N_2. The reaction vessel was exposed to high vacuum for 5-10 seconds every 0.5-1.5 hours for two working days (left under N_2 overnight). The volume of the solution was reduced to 8 mL under a stream of N_2 and layered with hexanes to give clear, colorless crystals (35.6 mg, 0.0422 mmol, 31%). ^{1}H NMR (300 MHz; CDCl$_3$; Me$_4$Si) δ 7.50 (m, 4H, C*H*), 7.13 (s, 2H, C*H*), 3.95 (AB*q*, 4*H*, CH$_2$, *J* 12.3).

Sb$_2$8$_3$ cryptand

2,6-bis(mercaptomethyl)naphthalene[4] (H$_2$**8**, 67.5 mg, 0.305 mmol) and SbCl$_3$ (49.1 mg, 0.215 mmol) were dissolved in CHCl$_3$ (125 mL) and stirred at 50 °C under N_2. The reaction vessel was exposed to high vacuum for 5-10 seconds several times a day for 10 days. The volume of the solution was reduced to 10 mL by vacuum and layered with CH$_3$CN to give < 10 mg of clear, colorless crystals.

X-ray Crystallography

Diffraction intensities were collected at 173(2) K on a Bruker Apex CCD diffractometer using MoKα radiation $\lambda = 0.71073$ Å. Absorption corrections were applied by SADABS.[9] Structures were solved by direct methods and Fourier techniques and refined on F^2 using full matrix least-squares procedures. All non-H atoms were refined with anisotropic thermal parameters. H

atoms were refined in calculated positions in a rigid group model. Solvent molecules, $CHCl_3$ in $As_2 8_3$ and CH_3CN in $Sb_2 8_3$, are disordered around -3 axis and were treated by SQUEEZE.[10] Corrections of the X-ray data by SQUEEZE (343 and 23 electron/cell, respectively for $As_2 8_3$, $Sb_2 8_3$) are close to the required values of 348 and 22 electron/cell for six and one molecules, respectively, in the full unit cells. In $As_2 6_3$ elongations of thermal ellipsoids for some carbon atoms in ligands perpendicular to C-C bonds were found. Such elongations seem to be related to a disorder for these carbon atoms. Some structural features in $Sb_2 8_3$ also indicate that the molecules in this structure are flexible or could be disordered as well. As results some of C-C bond distances in $Sb_2 8_3$, $As_2 5_3$ and $As_2 6_3$ were not able to be measured precisely. All calculations were performed by the Bruker SHELXTL (v. 6.10) package.[11]
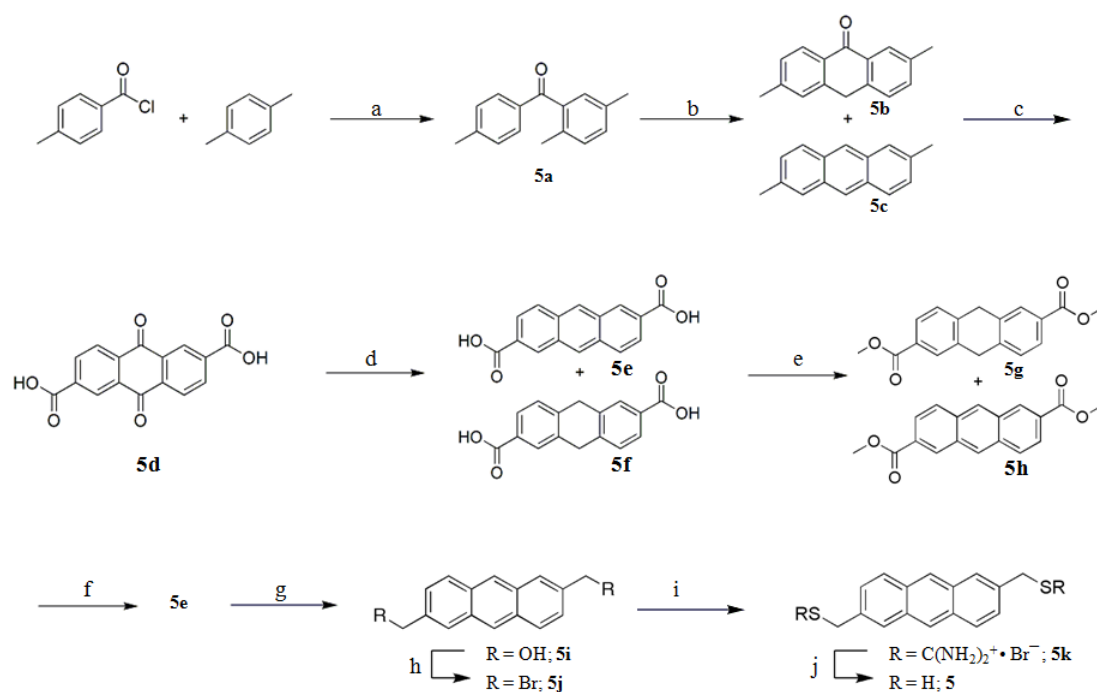
Scheme 1. Reagents and Conditions for $H_2 5$ synthesis.[5-7] (a) CS_2, $AlCl_3$, rt, 3 h, (b) 360 °C, 4 h, air, (c) CrO_3, acetic acid, 120 °C, 3 h, (d) $CuSO_4$, Zn^0, NH_4OH, 90 °C, 4 h, (e) CH_3I, Li_2CO_3, DMF, RT, 24 h, (f) DDQ, PhH, 90 °C, 1h, (g) LAH, THF, 70 °C, 1 h, (h) DCM, PBr_3, rt, N_2, 24 h, (i) NH_2CSNH_2, acetone, 70 °C, (j) NaOH, 110 °C, 2 h.
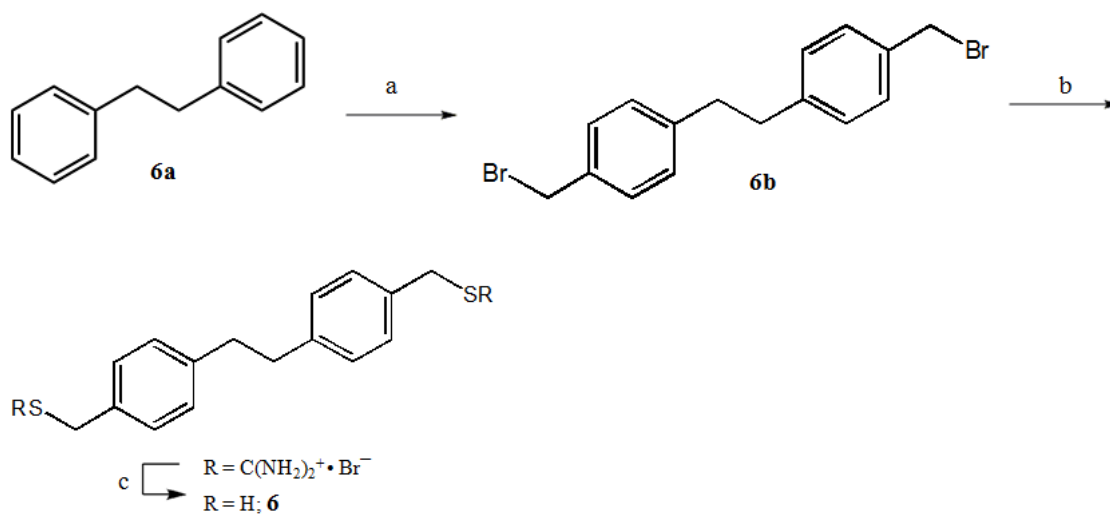
Scheme 2. Reagents and conditions for H$_2$**6** synthesis. (a) (CH$_2$O)n, ZnBr, 30% HBr/HOAc, 80 °C, 18 h, (b) NH$_2$CSNH$_2$, ethanol, 60 °C, 16 h, (c) NaOH, 100 °C, 2 h.
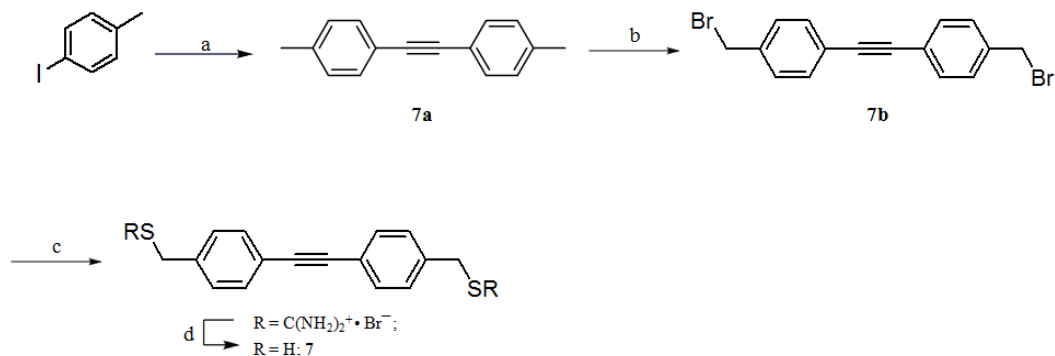
Scheme 3. Reagents and Conditions for H$_2$**7** synthesis.[8] (a) TMSA, PdCl$_2$(PPh$_3$)$_2$, CuI, DBU, CH$_3$CN, RT, 24 h, (b) NBS, benzoyl peroxide, CCl$_4$, 60 °C, 23 h, (c) NH$_2$CSNH$_2$, EtOH, 60 °C, 3 h, (d) NaOH, 110 °C, 2 h.

REFERENCES CITED

Chapter I

1.   C. T. Kresege, M. E. Lenowicz, W. J. Rot, J. C. Vartulli, J. S. Beck, *Nature*, 1992, **359**, 710.

2.   M. Grün, K. K. Unger, A. Matsumoto, and K. Tsutsumi, *Microporous Mesoporous Mater.*, 1999, **27**, 207.

3.   Y. Shi, Y. Wan, and D. Zhao, *Chem. Soc. Rev.*, 2011, **40**, 3854.

4.   P. J. Davis, C. J. Brinker, D. M. Smith, and R. A. Assink, *J. Non-Cryst. Solids*, 1992, **142**, 197.

5.   L. C. Klein, *J. Non-Cryst. Solids*, 1990, **119**, 119.

6.   G. E. Fryxell and J. Liu, in *Adsorption on Silica Surfaces*, ed. E. Paprier, Marcel Dekker, New York, 10th ed., 2000, 665.

7.   X. S. Zhao, G. Q. Lu, A. K. Whittaker, G. J. Millar, and H. Y. Zhu, *J. Phys. Chem. B.*, 1997, **101**, 6525.

8.   X. Feng, G. E. Fryxell, L. Q. Wang, A. Y. Kim, J. Liu, K. M. Kemner, *Science*, 1997, **276**, 923.

9.   S. Mann, S. L. Burkett, S. A. Davis, C. E. Fowler, N. H. Mendelson, S. D. Sims, D. Walsh, and N. T. Whilton, *Chem. Mater.*, 1997, **9**, 2300.

10.   A. Vinu, K. Z. Hossain, and K. Ariga, *J. Nanosci. Nanotechnol.*, 2005, **5**, 347.

11.   J.-M. Lehn, *Supramolecular chemistry : concepts and perspectives : a personal account built upon the George Fisher Baker lectures in chemistry at Cornell University [and] Lezioni Lincee, Accademia nazionale dei Lincei, Roma*, VCH, Weinheim; New York, 1995.

12.   J.-M. Lehn, *Science*, 1985, **227**, 849.

13.   C. Haensch, M. Chiper, C. Ulbricht, A. Winter, S. Hoeppener, and U. S. Schubert, *Langmuir*, 2008, **24**, 12981.

14. T. Yokoi, T. Tatsumi, and H. Yoshitake, *J. Colloid Interf. Sci.*, 2004, **274**, 451.

15. W. Yantasee, C. L. Warner, T. Sangvanich, R. S. Addleman, T. G. Carter, R. J. Wiacek, G. E. Fryxell, C. Timchalk, and M. G. Warner, *Environmental Science and Technology*, 2007, **41**, 5114.

16. S. V. Mattigod, K. Parker, and G. E. Fryxell, *Inorganic Chemistry Communications*, 2006, **9**, 96.

17. W. Yantasee, Y. H. Lin, T. S. Zemanian, and G. E. Fryxell, *Analyst*, 2003, **128**, 467.

18. S. A. Fontenot, T. G. Carter, D. W. Johnson, R. S. Addleman, M. G. Warner, W. Yantasee, C. L. Warner, G. E. Fryxell, and J. T. Bays, in *Trace Analysis with Nanomaterials*, eds. D. T. Pierce and J. X. Zhao, Wiley-VCH Verlag GmbH & Co. KGaA, Weinheim, 2010, 191.

19. G. L. Ellman, *Arch. Biochem. Biophys.*, 1959, **82**, 70.

20. F. Civan, *AIChE J.*, 2001, **47**, 3301.

21. H. Takahashi, B. Li, T. Sasaki, C. Miyazaki, and T. Kajino, *Chem. Mater.*, 2000, **12**, 3301.

Chapter II

1. G. E. Fryxell, J. Liu, S. V. Mattigod et al., in *Ceramics Transactions Vol. 107*, ed. G. T. Chandler, X. Feng, The American Ceramic Society, 2000, 29.

2. G. E. Fryxell, Y. Lin, H. Wu et al., in *Studies in Surface Science and Catalysis Vol. 141*, ed. A. Sayari, M. Jaroniec, Elsevier Science, 2002, 583.

3. G. E. Fryxell, R. S. Addleman, S. V. Mattigod et al., *Ency. Nanosci. Nanotech.*, Marcel-Dekker, 2004, 1135.

4. G. E. Fryxell, Y. Lin, S. Fiskum et al., *Envi. Sci. Technol.*, 2005, **39**, 1324.

5. D. P. Mellor, *Chemistry of Chelation and Chelating Agents*, Pergamon Press, New York, NY, 1979.

6. D. T. Richens, *The Chemistry of Aqua Ions*, John Wiley & Sons Ltd, West Sussex, UK, 1997.

7. R. G. Pearson, *J. Am. Chem. Soc.*, 1963, **85**, 3533.

8. R. T. Herrin, A. W. Andren, M. M. Shafer et al., *Environ. Sci. Technol.*, 2001, **35**, 1959.

9. K. J. Powell, P. L. Brown, R. H. Byrne et al., *Aus. J. Chem.*, 2004, **57**, 993.

10. R. H. Byrne, *Geochem. Trans.*, 2002, **3**, 11.

11.   W. Yantasee, B. Charnhattakorn, G. E. Fryxell et al., *Anal. Chim. Acta*, 2008, **620**, 55.

12.   W. Yantasee, C. L. Warner, T. Sangvanich et al., *Environ. Sci. Technol.*, 2007, **41**, 5114.

13.   P. J. Lloyd-Jones, J. R. Rangel-Mendez, M. Streat, *Process Saf. Environ. Prot.*, 2004, **82**, 301.

14.   T. G. Carter, W. Yantasee, T. Sangvanich et al., *Chem. Commun.*, 2008, 5583.

15.   USP United States Pharmacopeial Convention Inc., Rockville, MD, USA, 22nd Edition, 1990.

16.   L. Shargel, A. B. C. Yu, in *Encyclopedia of Pharmaceutical Technology Vol 1*, ed. J. Swarbrick, J. C. Boylan, Informa Health Care, London, UK, 2002, 164.

17.   W. Yantasee, B. Charnhattakorn, G. E. Fryxell et al., *Anal. Chim. Acta*, 2008, **620**, 55.

18.   S. A. Corr, Y. P. Rakovich, Y. K. Gun'ko, *Nanoscale Res. Lett.*, 2008, **3**, 87.

19.   I. M. Hsing, Y. Xu, W. Zhao, *Electroanalysis*, 2007, **19**, 755.

20.   D. L. Huber, *Small*, 2005, **1**, 482.

21.   E. Katz, I. Willner, *Angew. Chem. Int. Ed.*, 2004, **43**, 6042.

22.   E. Katz, I. Willner, J. Wang, *Electroanalysis*, 2004, **16**, 19.

23.   A. H. Latham, M. E. Williams, *Acc. Chem. Res.*, 2008, **41**, 411.

24.   S. Laurent, D. Forge, M. Port et al., *Chem. Rev.*, 2008, **108**, 2064.

25.   A. H. Lu, E. L. Salabas, F. Schueth, *Angew. Chem. Int. Ed.*, 2007, **46**, 1222.

26.   M. Magnani, L. Galluzzi, I. J. Bruce, *J. Nanosci. Nanotechnol.*, 2006, **6**, 2302.

27.   Q. A. Pankhurst, *BT Technol.*, *J.* 2006, **24**, 33.

28.   Q. A. Pankhurst, J. Connolly, S. K. Jones et al., *J. Phys. D Appl. Phys.*, 2003, **36**, 167.

29.   S. Rodriguez-Mozaz, M. J. L. de Alda, D. Barcelo, *Anal. Bioanal. Chem.*, 2006, **386**, 1025.

30.   V. Salgueirino-Maceira, M. A. Correa-Duarte, *Adv. Mater.*, 2007, **19**, 4131.

31.   M. Seydack, *Biosens. Bioelectron.*, 2005, **20**, 2454.

32.   P. Tartaj, M. D. Morales, S. Veintemillas-Verdaguer et al., *J. Phys. D Appl. Phys.*, 2003, **36**, 182.

33. W. Yantasee, Y. Lin, K. Hongsirikarn et al. *Environ. Health Persp.*, 2007, **115**, 1683.

34. W. Yantasee, C. L. Warner, T. Sangvanich et al., *Environ. Sci. Technol.*, 2007, **41**, 5114.

35. C. F. Poole, *Trends Anal. Chem.*, 2003, **22**, 362.

36. B. L. Cushing, V. L. Kolesnichenko, C. J. O'Connor, *Chem. Rev.*, 2004, **104**, 3893.

37. Y. Jun, J. Choi, J. Cheon, *Angew. Chem. Int. Ed.*, 2006, **45**, 3414.

38. M. A. Neouze, U. Schubert, *Monatsh. Chem.*, 2008, **139**, 183.

39. J. Park, J. Joo, S. Kwon et al., *Angew. Chem. Int. Ed.*, 2007, **46**, 4630.

40. Y. H. Deng, C. C. Wang, J. H. Hu et al., *Colloid Surface A*, 2005, **262**, 87.

41. G. Ennas, A. Musinu, G. Piccaluga et al., *Chem. Mater.*, 1998, **10**, 495.

42. C. W. Lu, Y. Hung, J. K. Hsiao et al., *Nano Lett.*, 2007, **7**, 149.

43. S. Santra, R. Tapec, N. Theodoropoulou et al., *Langmuir*, 2001, **17**, 2900.

44. W. Stober, A. Fink, E. Bohn, *J. Colloid Interf. Sci.*, 1968, **26**, 62.

45. E. E. Carpenter, *J. Magn. Magn. Mater.*, 2001, **225**, 17.

46. M. Mikhaylova, D. K. Kim, N. Bobrysheva et al., *Langmuir*, 2004, **20**, 2472.

47. C. K. Lo, D. Xiao, M. M. F. Choi, *J. Mater. Chem.*, 2007, **17**, 2418.

48. Q. H. Lu, K. L. Yao, D. Xi et al., *J. Magn. Magn. Mater.*, 2006, **301**, 44.

49. M. Mandal, S. Kundu, S. K. Ghosh et al., *J. Colloid Interf. Sci.*, 2005, **286**, 187.

50. H. Y. Park, M. J. Schadt, L. Y. Wang et al., *Langmuir*, 2007, **23**, 9050.

51. J. Lim, A. Eggeman, F. Lanni et al., *Adv. Mater.*, 2008, **20**, 1721.

52. Z. Xu, Y. Hou, S. Sun, *J. Am. Chem. Soc.*, 2007, **129**, 8698.

53. L. Wang, J. Luo, M. M. Maye et al., *J. Mater. Chem.*, 2005, **15**, 1821.

54. P. Gong, H. Li, X. He et al., *Nanotechnology*, 2007, **18**, 285604.

55. Y. Kimishima, W. Yamada, M. Uehara et al., *Mat. Sci. Eng. B*, 2007, **138**, 69.

56.   D. P. Tang, R. Yuan, Y. Q. Chai, *J. Phys. Chem. B*, 2006, **110**, 11640.

57.   C. Liu, Z. Zhou, X. Yu et al., *Inorg. Mater.*, 2008, **44**, 291.

58.   W. Yantasee, K. Hongsirikarn, C. L. Warner et al., *Analyst*, 2008, **133**, 348.

59.   S. Shin, J. Jang, *Chem. Commun.*, 2007, 4230.

60.   A. Ngomsik, A. Bee, M. Draye et al., *C. R. Chim.*, 2005, **8**, 963.

61.   C. T. Yavuz, J. T. Mayo, W. W. Yu et al., *Science*, 2006, **314**, 964.

62.   S. Yean, L. Cong, C. T. Yavuz et al., *J. Mater. Res.*, 2005, **20**, 3255.

63.   G. E. Fryxell, in *Environmental Applications of Nanomaterials*, ed. G. E. Fryxell, G. Cao, Imperial College Press, London, UK, 2007, 159.

64.   G. E. Fryxell, S. V. Mattigod, Y. Lin et al., *J. Mater. Chem.*, 2007, **17**, 2863.

65.   S. V. Mattigod, G. E. Fryxell, K. Alford et al., *Environ. Sci. Technol.*, 2005, **39**, 7306.

66.   S. V. Mattigod, G. E. Fryxell, K. E. Parker, *Inorg. Chem. Commun.*, 2007, **10**, 646.

67.   M. Santandreu, S. Sole, E. Fabregas et al., *Biosens. Bioelectron.*, 1998, **13**, 7.

68.   M. Riskin, B. Basnar, Y. Huang et al., *Adv. Mater.*, 2007, **19**, 2691.

69.   H. B. Liu, J. Guo, L. Jin et al., *J. Phys. Chem. B*, 2008, **112**, 3315.

70.   J. Cai, J. Guo, M. L. Ji et al., *Colloid Polym. Sci.*, 2007, **285**, 1607.

71.   E. Palecek, M. Fojta, *Talanta*, 2007, **74**, 276.

72.   A. de la Escosura-Muniz, A. Ambrosi, and A. Merkoci, *Trends Anal. Chem.*, 2008, **27**, 568.

73.   http://www.epa.gov/ogwdw/hfacts.html - accessed Feb. 2012.

74.   G. D. Liu, C. Timchalk, Y. H. Lin, *Electroanalysis*, 2006, **18**, 1605.

75.   G. Liu, Y. Lin, *J. Nanosci. Nanotechno.*, 2005, **5**, 1060.

76.   R. C. Bansal, M. Goyal, *Activated Carbon Adsorption*, Taylor & Francis: New York, NY, 2005.

77.   R. Pelech, E. Milchert, M. Bartkowiak, *J. Colloid Interface Sci*, ,2006, **296**, 458.

78.   Z. X. Jiang, Y. Liu, X. P. Sun et al., *Langmuir*, 2003, **19**, 731.

79. D. Satapathy, G. S. Natarajan, *Adsorption*, 2006, **12**, 147.

80. S. Babel, T. A. Kurniawan, *Chemosphere*, 2004, **54**, 951.

81. N. Kannan, G. Rengasamy, *Fresenius Environ. Bull.*, 2005, **14**, 435.

82. H. Kasaini, R. C. Everson, O. S. L. Bruinsma *Sep. Sci .Technol.*, 2005, **40**, 507.

83. M. Abdulkarim, F. Abu Al-Rub, *Adsorpt. Sci. Technol.*, 2004, **22**, 119.

84. J. R. Rangel-Mendez, M. Streat, *Water Res.*, 2002, **36**, 1244.

85. S. Biniak, M. Pakula, G. S. Szymanski et al. *Langmuir*, 1999, **15**, 6117.

86. C. Y. Yin, M. K. Aroua, W. Daud, *Colloids Surf.*, *A* 2007, **307**, 128.

87. A. M. Yusof, M. M. Rahman, A. K. H. Wood, *J. Radioanal. Nucl. Chem.*, 2004, **259**, 479.

88. A. M. Yusof, M. M. Rahman, A. K. H. Wood, *J. Radioanal. Nucl. Chem.*, 2007, **271,** 191.

89. C. Y. Yin, M. K. Aroua, W. Daud, *Sep. Purif. Technol.*, 2007, **52**, 403.

90. W. Yantasee, Y. H. Lin, K. L. Alford et al., *Sep. Sci. Technol.*, 2004, **39**, 3263.

91. W. Yantasee, Y. H. Lin, G. E. Fryxell et al., *Ind. Eng. Chem. Res.*, 2004, **43**, 2759.

92. R. B. Merrifield, *J. Am. Chem. Soc.*, 1963, **85**, 2149.

93. W. D. Samuels, N. H. LaFemina, V. Sukwarotwat, W. Yantasee, X. S. Li, and G. E. Fryxell, *Sep. Sci. Technol.*, 2010, **45**, 228.

94. M. B. Gholivand, F. Ahmadi, E. Rafiee, *Sep. Sci. Technol.*, 2007, **42**, 897.

95. R. Ryoo, S. H. Joo, S. Jun, *J. Phys. Chem.*, *B* 1999, **103**, 7743.

96. S. H. Joo, S. J. Choi, I. Oh et al., *Nature*, 2001, **412**, 169.

97. K. P. Gierszal, M. Jaroniec, *J. Am. Chem. Soc.*, 2006, **128**, 10026.

98. J. Lee, K. Sohn, T. Hyeon, *J. Am. Chem. Soc.*, 2001, **123**, 5146.

99. C. H. Kim, D. K. Lee, T. J. Pinnavaia, *Langmuir*, 2004, **20**, 5157.

100. A. H. Lu, A. Kiefer, W. Schmidt et al., *Chem. Mater.*, 2004, **16**, 100.

101. C. D. Liang, S. Dai, *J. Am. Chem. Soc.*, 2006, **128**, 5316.

102. X. Q. Wang, C. D. Liang, S. Dai, *Langmuir*, 2008, **24**, 7500.

103. Y. D. Xia, R. Mokaya, *Chem. Mater.*, 2005, **17**, 1553.

104. Y. D. Xia, Z. X. Yang, R. Mokaya, *J. Phys. Chem. B*, 2004, **108**, 19293.

105. Z. X. Yang, Y. D. Xia, X. Z. Sun et al., *J. Phys. Chem. B*, 2006, **110**, 18424.

106. P. F. Fulvio, M. Jaroniec, C. D. Liang et al., *J. Phys. Chem.*, *C* 2008, **112**, 13126.

107. F. A. Cotton, G. Wilkinson, *Advanced Inorganic Chemistry*, 4th ed., John Wiley & Sons: New York, NY, 1980.

108. Y. Shin, G. E. Fryxell, M. H. Engelhard et al., *Inorg. Chem. Commun.*, 2007, **10**, 1541.

109. O. P. Bahl, Z. Shen, J. G. Lavin et al., in *Carbon Fibers*, 3rd ed., ed. S. Rebouillat, J. B. Donnet, T. K. Wang, J. C. M. Peng, Marcel-Dekker, New York, NY, 1998, 1.

110. Y. Shin, G. E. Fryxell, C. A. Johnson et al., *Chem. Mater.*, 2008, **20**, 981.

111. Y. Shin, C. M. Wang, M. H. Engelhard et al., *Microporous Mesoporous Mater.*, 2009, **123**, 345

112. Y. S. Shin, G. Fryxell, W. Y. Um et al., *Adv. Funct. Mater.*, 2007, **17**, 2897.

113. C. Baerlocher, W. M. Meier, D. H. Olson, *Atlas of Zeolite Framework Types*, 5th ed., Elsevier, Amsterdam, 2001.

114. E. Erdem, N. Karapinar, R. Donat, *J. Colloid Interface Sci.*, 2004, **280**, 309.

115. M. Hartmann, L. Kevan, *Chem. Rev.* 1999, **99**, 635.

116. G. San Miguel, S. D. Lambert, N. J. D. Graham, *J. Chem. Technol. Biotechnol.*, 2006, **81**, 1685.

117. M. J. Zamzow, B. R. Eichbaum, K. R. Sandgren et al., *Sep. Sci. Technol.*, 1990, **25**, 1555.

118. W. Um, C. Papelis, *Environ. Sci. Technol.*, 2004, **38**, 496.

119. W. Um, C. Papelis, *Am. Mineral.*, 2003, **88**, 2028.

120. S. M. Dal Bosco, R. S. Jimenez, W. A. Carvalho, *J. Colloid Interface Sci.*, 2005, **281**, 424.

121. J. Weitkamp, *Solid State Ionics*, 2000, **131**, 175.

122. U. Wingenfelder, C. Hansen, G. Furrer et al., *Environ. Sci. Technol.*, 2005, **39**, 4606.

123. T. Shahwan, B. Zünbül, Ö. Tunusoglu et al., *J. Colloid Interface Sci.*, 2005, **286**, 471.

124. A. H. Ören, A. Kaya, *J. Hazard. Mater.*, 2006, **131**, 59.

125. N. Z. Logar, V. Kaucic, *Acta Chim. Slov.*, 2006, **53**, 117.

126. M. Vaca Mier, R. López Callejas, R. Gehr et al., *Water Res.*, 2001, **35**, 373.

127. K. B. Payne, T. M. Abdel-Fattah, *J. Environ. Sci. Health A*, 2005, **40**, 723.

128. B. Dousová, T. Grygar, A. Martaus et al., *J. Colloid Interface Sci.*, 2006, **302**, 424.

129. Y.-h. Xu, T. Nakajima, A. Ohki, *J. Hazard. Mater.*, 2002, **92**, 275.

130. Y. S. Tao, H. Kanoh, L. Abrams et al., *Chem. Rev.*, 2006, **106**, 896.

131. M. E. Davis, *Nature*, 2002, **417**, 813.

132. T. O. Drews, M. Tsapatsis, *Curr. Opin. Colloid Interface Sci.*, 2005, **10**, 233.

133. M. G. Valdés, A. I. Pérez-Cordoves, M. E. Díaz-García, *Trends Anal. Chem.*, 2006, **25**, 24.

134. T. Prasada Rao, S. Daniel, J. Mary Gladis, *Trends Anal. Chem.*, 2004, **23**, 28.

135. H. Nishide, E. Tsuchida, *Makromol. Chem.*, 1976, **177**, 2295.

136. H. Nishide, J. Deguchi, E. Tsuchida, *Chem. Lett.*, 1976, 169.

137. S. Y. Bae, G. L. Southard, G. M. Murray, *Anal. Chim. Acta*, 1999, **397**, 173.

138. S. Shirvani-Arani, S. J. Ahmadi, A. Bahrami-Samani et al., *Anal. Chim. Acta*, 2008, **623**, 82.

139. V. M. Biju, J. M. Gladis, T. P. Rao, *Anal. Chim. Acta*, 2003, **478**, 43.

140. T. Rosatzin, L. I. Andersson, W. Simon et al., *J. Chem. Soc.*, *Perkin Trans. 2*, 1991, 1261.

141. R. Garcia, C. Pinel, C. Madic et al., *Tetrahedron Lett.*, 1998, **39**, 8651.

142. T. P. Rao, R. Kala, S. Daniel, *Anal. Chim. Acta*, 2006, **578**, 105.

Chapter III

1. M.A. Shannon, et al., *Nature*, 2008, 452, 301.

2. M. Hightower and S.A. Pierce, *Nature*, 2008, 452, 285.

3. G.E. Fryxell, et al., *Envi. Sci. Technol.*, 2005, **39**, 1324.

4.   W. Yantasee, G.E. Fryxell, and Y.H. Lin, *Analyst*, 2006, **131**, 1342.

5.   W. Yantasee, et al., *Envi. Sci. Technol.*, 2007, **41**, 5114.

6.   S. Babel, and T.A. Kurniawan, J. Hazard. Mater., 2003, **97**, 219.

7.   Z.Y. Xu, Q.X. Zhang, and H.H.P. Fang, *Crit. Rev. Env. Sci. Technol.*, 2003, **33**, 363.

8.   G. San Miguel, S.D. Lambert, and N.J.D. Graham*, J. Chem. Technol. Biotechnol.*, 2006, **81**, 1685.

9.   A.R. Turker, *Clean-Soil Air Water*, 2007, **35**, 548.

10.   V.A. Lemos, et al., *Appl. Spectrosc. Rev.*, 2008, **43**, 303.

11.   W. Yantasee, et al., *ACS Appl. Mater. Interfaces*, 2010, **2**, 2749.

12.   T.P. Rao, R.S. Praveen, and S. Daniel, *Crit. Rev. Anal. Chem.*, 2004, **34**, 177.

13.   V. Pichon and F. Chapuis-Hugon, *Analytica Chimica Acta*, 2008, **622**, 48.

14.   A. Kloskowski, et al., *Crit. Rev. Anal. Chem.*, 2009, **39**, 43.

15.   M.S. Mauter, and M. Elimelech, *Envi. Sci. Technol.*, 2008. **42**, 5843.

16.   W. Yantasee, et al., *Ind. Eng. Chem. Res.*, 2004, **43**, 2759.

17.   X. Feng, et al., *Science*, 1997, **276**, 923.

18.   G.E. Fryxell et al., *J. Mater. Chem.*, 2007, **17**, 2863.

19.   F. Hoffmann, et al., *Angew. Chem. Int. Ed.*, 2006, **45**, 3216.

20.   G.E. Fryxell, *Ceramic Transactions*, 2000, **107**, 29.

21.   G. E. Fryxell, et al., in *Studies in Surface Science and Catalysis*, ed. A. Sayari, and M. Jaroniec, Elsevier Science, 2002, 583.

22.   B. Busche, et al., *Inorg. Chem. Commun.*, 2009, **12**, 312.

23.   W. Yantasee, et al., *Analyst*, 2003, **128**, 467.

24.   W. Yantasee, et al., *Analytica Chimica Acta*, 2008, **620**, 55.

25.   E. De Canck, et al., *Langmuir*, 2010, **26**, 10076.

26. W. Yantasee, et al., *Analyst*, 2003, **128**, 899.

27. Y.S., Shin, *Adv. Funct. Mater.*, 2007, **17**, 2897.

28. C.L. Warner, et al., *Chem. Sus. Chem*, 2010, **3**, 749.

29. W. Yantasee, et al., *Analyst*, 2008, **133**, 348.

31. M.G. Warner, C.L. Warner, R.S. Addleman, and W. Yantasee, in *Magnetic Nanomaterials*: NmLS-Series, vol. 4, Wiley-VCH, 2010.

32. T.G. Carter, et al., *Chem. Comm.*, 2008, **43**, 5583.

33. C.T. Kresge, et al., *Nature*, 1992, **359**, 710.

34. J.S. Beck, et al., *J. Am. Chem. Soc.*, 1992, **114**, 10834.

35. E.P. Barrett, L.G. Joyner, and P.P. Halenda, *J. Am. Chem. Soc.*, 1951, **73**, 373.

36. S. Brunauer, P.H. Emmett, and E. Teller, *J. Am. Chem. Soc.*, 1938, **60**, 309.

37. G.L. Ellman, *Arch. Biochem. Biophys.*, 1959, **82**, 70.

38. S.R. Wasserman, et al., *J. Am. Chem. Soc.*, 1989, **111**, 5852.

39. G.E. Fryxell and J. Liu, in *Adsorption on Silica Surfaces*, ed. E. Paprier, 2000, Marcel Dekker, New York, NY, 665.

40. http://water.epa.gov/drink/contaminants/index.cfm#inorganic - accessed June, 2011

41. N. Gartmann and D. Bruhwiler, *Mesoporous Materials*, 2009, **48**, 6354

42. D. T. Richens, *The Chemistry of Aqua Ions*, John Wiley & Sons, West Sussex, UK, 1997.

Chapter IV

1. D. Granadero, J. Bordello, M. J. Pérez-Alvite, M. Novo, and W. Al-Soufi, *Int. J. Mol. Sci.*, 2010, **11**, 173-188.

2. K. a. Connors, *Chem. Rev.*, 1997, **97**, 1325.

3. E. M. M. Del Valle, *Process Biochem.*, 2004, **39**, 1325.

4. J. Szejtli, *Chem. Rev.*, 1998, **98**, 1743.

5. X. Feng, G. E. Fryxell, L. Q. Wang, A. Y. Kim, J. Liu, and K. M. Kemner, *Science*, 1997, **276**, 923.

6.   N. Zhong, H.-sup Byun, and R. Bittrnan, *Tetrahedron Lett.*, 1998, **39**, 2919.

7.   Y.-F. Poon, I. W. Muderawan, and S.-C. Ng, *J. Chromatogr. A.*, 2006, **1101**, 185.

8.   N. Gartmann and D. Brühwiler, *Angew. Chem. Int. Ed.*, 2009, **48**, 6354.

9.   H. Park, B. Mayer, and P. Wolschann, *J. Phys. Chem.*, 1994, **98**, 6158.

10.   H. Jiang, H. Sun, S. Zhang, R. Hua, Y. Xu, S. Jin, H. Gong, and L. Li, *J. Inclusion Phenom. Macrocyclic Chem.*, 2006, **58**, 133.

11.   G. L. Ellman, *Arch. Biochem. Biophys.*, 1959, **82**, 70.

12.   A. Harada, R. Kobayashi, Y. Takashima, A. Hashidzume, and H. Yamaguchi, *Nature Chem.*, 2011, **3**, 3157.

13.   F. V. D. Manakker, T. Vermonden, C. F. V. Nostrum, and W. E. Hennink, *Biomacromolecules*, 2009, **10**, 3157.

Chapter V

1.   *(a)* D. L. Caulder and K. N. Raymond, *Acc. Chem. Res.*, 1999, **32**, 975; *(b)* S. Leininger, B. Olenyuk and P. J. Stang, *Chem. Rev.*, 2000, **100**, 853; *(c)* M. W. Hosseini, *Acc. Chem. Res.*, 2005, **38**, 313; *(d)* D. J. L. Tranchemontagne, Z. Ni, M. O'Keeffe and O. M. Yaghi, *Angew. Chem. Int. Ed.*, 2008, **47**, 5136; *(e)* Z. Wang and S. M. Cohen, *Angew. Chem. Int. Ed.*, 2008, **47**, 4699.

2.   M. Hutin, D. Schultz and J. R. Nitschke, *Chimia*, 2008, **62**, 198; R. J. Sarma and J. R. Nitschke, *Angew. Chem. Int. Ed.*, 2008, **47**, 377.

3.   D. Fiedler, D. H. Leung, R. G. Bergman and K. N. Raymond, *Acc. Chem. Res.*, 2005, **38**, 351.

4.   M. A. Pitt and D. W. Johnson, *Chem. Soc. Rev.*, 2007, **36**, 1441.

5.   S. R. Batten, S. M. Neville and D. R. Turner, *Coordination Polymers: Design, Analysis, and Application*; RSC Publishing, Cambridge, 2009, 7.

6.   V. M. Cangelosi, L. N. Zakharov and D. W. Johnson, *Angew. Chem. Int. Ed.*, 2010, **49**, 1248.

7.   V. M. Cangelosi, T. G. Carter, J. L. Crossland, L. N. Zakharov and D. W. Johnson, *Inorg. Chem.,* 2010, **49**, 9985.

8.   V. M. Cangelosi, T. G. Carter, L. N. Zakharov and D. W. Johnson, *Chem. Commun.* 2009, **45**, 5606.

9.   W. J. Vickaryous, R. Herges and D. W. Johnson, *Angew. Chem. Int. Ed.* 2004, **43**, 5831.

10.   M. A. Pitt, L. N. Zakharov, K. Vanka, W. Thompson, B. Laird and D. W. Johnson, *Chem. Commun.*, 2008, **44**, 3936.

11.   *(a)* H. Schmidbaur, W. Bublak, B. Huber and G. Müller, *Angew. Chem.*, 1987, **99**, 248; *(b)* H. Schmidbaur, R. Nowak, B. Huber and G. Müller, *Organometallics*, 1987, **6**, 2266. (*c*) T. Probst, O. Steigelmann, H. Riede and H. Schmidbaur, *Chem. Ber.*, 1991, **124**, 1089.

12.   W. J. Vickaryous, L. N. Zakharov and D. W. Johnson, *Main Group Chemistry*, 2006, **5**, 51.

13.   *(a)* W. J. Vickaryous, E. R. Healey, O. B. Berryman and D. W. Johnson, *Inorg. Chem.,* 2005, **44**, 9247; *(b)*V. M. Cangelosi, L. N. Zakharov, S. A. Fontenot, M. A. Pitt and D. W. Johnson, *Dalton Trans.*, 2008, 3447. (*c*) V. M. Cangelosi, A. C. Sather, L. N. Zakharov, O. B. Berryman and D. W. Johnson, *Inorg. Chem.,* 2007, **46**, 9278.

14.   *(a)* A. Schier, J. M. Wallis, G. Müller and H. Schmidbaur, *Angew. Chem. Int. Ed.*, 1986, **25**, 757; *(b)* H. Schmidbaur, R. Nowak, A. Schier, J. M. Wallis, B. Huber and G. Müller, *Chem. Ber. Recl.*, 1987, **120**, 1829; *(c)* H. Schmidbaur, J. M. Wallis, R. Nowak, B. Huber and G. Müller, *Chem. Ber. Recl.*, 1987, **120**, 1837; *(d)* H. Schmidbaur, R. Nowak, O. Steigelmann and G. Müller, *Chem. Ber.*, 1990, **123**, 1221.

15.   H. Schmidbaur and A. Schier, *Organometallics*, 2008, **27**, 2361.

16.   N. R. Lindquist, T. G. Carter, V. M. Cangelosi, L N. Zakharov and D. W. Johnson, *Chem. Commun.*, 2010, **46**, 3505.

17.   H. Schmidbaur, T. Probst, B. Huber, O. Steigelmann and G. Müller, *Organometallics*, 1989, **8**, 1567.

18.   C. Piguet, G. Bernardinelli and G. Hopfgartner, *Chem. Rev.*, 1997, **97**, 2005.

19.   G. A. Hembury, V. V. Borovkov and Y. Inoue, *Chem. Rev.*, 2008, **108**, 1.

20.   M. Albrecht, *Chem. Eur. J.*, 2000, **6**, 3485.

21.   *(a)* D. L. Caulder, R. E. Powers, T. N. Parac and K. N. Raymond, *Angew. Chem. Int. Ed.*, 1998, **37**, 1840; *(b)* R. M. Yeh, J. Xu, G. Seeber and K. N. Raymond, *Inorg. Chem.*, 2005, **44**, 6228.

22.   *(a)* M. Meyer, B. Kersting, R. E. Powers and K. N. Raymond, *Inorg. Chem.*, 1997, **36**, 5179. *(b)* R. M. Yeh, M. Ziegler, D. W. Johnson, A. J. Terpin and K. N. Raymond, *Inorg. Chem.*, 2007, **40**, 2216. *(c)* J. Xu, T. N. Parac and K. N. Raymond, *Angew. Chem.*, 1999, **38**, 2878.

Appendix

1. M. Grün, K. K. Unger, A. Matsumoto, and K. Tsutsumi, *Microporous Mesoporous Mater.*, 1999, **27**, 207.

2. W. Yantasee, C. L. Warner, T. Sangvanich et al., *Environ. Sci. Technol.*, 2007, **41**, 5114.

3. V. M. Cangelosi, L. N. Zakharov, J. L. Crossland, B. C. Franklin, D. W. Johnson, *Cryst. Growth Des.*, 2010, **10**, 1471.

4. V. M. Cangelosi, A. C. Sather, L. N. Zakharov, O. B. Berryman and D. W. Johnson, *Inorg. Chem.*, 2007, **46**, 9278.

5. R. J. Jones, L. C. Liotta, M. D. Collard, A. D. Schiraldi, *Macromolecules*, 1999, **32***, 5792.

6. R. S. Givens, M. K. Venkatramanan, J. Figard, *Tetrahedron Lett.*, 1984, **25**, 2187.

7. D. R. Broene, D. François, *Tetrahedron Lett.*, 1991, **32***, 5227.

8. M. J. Mio, L. C. Kopel, J. B. Braun, T. L. Gadzikwa, K. L. Hull, R. G. Brisbois, C. J. Markworth, and Paul A. Grieco, *Org. Lett.*, 2002, **9**, 3199.

9. G. M. Sheldrick, *Bruker/Siemens Area Detector Absorption Correction Program*, Bruker AXS, Madison, WI, 1998.

10. P. van der Sluis and A. L. Spek, *Acta Cryst., Sect. A.,* 1990, **46**, 194.

11. SHELXTL-6.10 "Program for Structure Solution, Refinement and Presentation" Bruker AXS Inc., 5465 East Cheryl Parkway, Madison, WI